

ION TRAFFIC ACROSS CELLULAR MEMBRANES

by Jill Gallaher

April, 2010

m Under the direction of Dr. Martin Bier

DEPARTMENT OF PHYSICS

The cell membrane protects the delicate internal machinery of the cell and hosts a complex transport system for ion exchange with the environment. Energy is continually expended to maintain a transmembrane electrical potential of about 80 mV.

Low extracellular potassium leads to some interesting dynamics that elucidate mechanisms for energy expenditure and survival. As the extracellular potassium concentration, $[K^+]_o$, is lowered, the transmembrane potential hyperpolarizes. But at a certain point in decreasing $[K^+]_o$, a switch to a depolarized state occurs. A switch back to the hyperpolarized state occurs when again increasing the $[K^+]_o$, but this switch occurs at a higher $[K^+]_o$ than the one at which the switch to depolarization occurred. So there is an apparent hysteresis.

In a system of ion pumps, ion channels, and ion transporters the flows of sodium, potassium, and chloride are tightly coupled. A model is set up involving the most relevant components in the ion transport. The model reproduces the observed hysteresis and can quantitatively account for the change in location and size of the hysteresis loop when an important chloride transporter is blocked or stimulated.

The switching points in the hysteresis loop occur when inward rectifying potassium channels (IRKs) close or open. Adding isoprenaline opens other potassium channels and makes the IRK contribution negligible. After also neglecting the role of chloride, the fixed potassium permeability leads to a system that can be analytically solved. Expressions are derived for the position and the size of the hysteresis loop. The expressions agree with experimental data and provide insight into the evolutionary origin of the IRKs.

The membrane's freezing temperature is just slightly below physiological temperatures. At the freezing transition the membrane exhibits increased ion permeability. The increased permeability

comes in the form of quantized bursts similar to those of ion channel currents. The currents through a pure membrane near the phase transition are measured and analyzed. Power laws are found, and the power spectral density of the current signal appears to follow a $1/f$ pattern. A theoretical basis for this behavior is formulated and a physical explanation is proposed. Biological significance is discussed.

ION TRAFFIC ACROSS CELLULAR MEMBRANES

A Dissertation

Presented To

The Faculty of the Department of Physics

East Carolina University

In Partial Fulfillment

of the Requirements for the Degree

Doctor of Philosophy in Biomedical Physics

by

Jill Gallaher

April, 2010

ION TRAFFIC ACROSS CELLULAR MEMBRANES

by

Jill Gallaher

APPROVED BY:

DIRECTOR OF DISSERTATION:

Martin Bier, Ph.D

COMMITTEE MEMBER:

Michael Dingfelder, Ph.D

COMMITTEE MEMBER:

John Kenney, Ph.D.

COMMITTEE MEMBER:

Alexander Murashov, M.D., Ph.D

COMMITTEE MEMBER:

Mark Sprague, Ph.D.

CHAIR OF THE DEPARTMENT OF PHYSICS:

John Sutherland, Ph.D.

DEAN OF THE GRADUATE SCHOOL:

Paul J. Gemperline, Ph.D.

DEDICATION

This one goes out to all my homies.

ACKNOWLEDGEMENTS

I would like to thank my advisor, Dr. Martin Bier, for sparking my interest in this subject and acknowledge the hard work and patience he put into guiding me through some new ideas, processes, and techniques. His creativity and humor have made this work exciting and enjoyable.

This research wouldn't be possible without collaboration with others. I have worked with Jan Siegenbeek van Heukelom of the University of Amsterdam for over five years now. He has given me a ton of insight into ion channel research. His group provided the experimental data presented here involving transmembrane voltage recordings of mouse muscle cells. Thomas Heimberg's membrane biophysics group of the University of Copenhagen provided the experimental data that is presented here involving black lipid membranes. Katarzka Wodzińska conducted the experiments.

I would like to thank Dr. John Kenney, Dr. Mark Sprague, Dr. Michael Dingfelder, and Dr. Alexander Murashov for serving on my committee. Special thanks are also extended to Dr. Roberta Johnke, Nick Bakken, Jen Sattler, Julie DiNitto, and Bineyam Kasshun for the discussions, debates, encouragement, advice and/or proofreading.

TABLE OF CONTENTS

LIST OF FIGURES	v
LIST OF TABLES	vi
LIST OF ABBREVIATIONS, SYMBOLS, UNITS, AND CONSTANTS	viii
0.1 Abbreviations	viii
0.2 Symbols	ix
0.3 Units	xii
0.4 Constants	xii
1 COMPLEXITIES, HYSTERESIS, AND PHASE TRANSITIONS	1
2 THE MEMBRANE AS A BARRIER AND A GATEWAY	5
2.1 A Brief History of Membrane Models	5
2.2 The Hydrophobic Effect	8
2.3 Bilayer Composition and Organization	10
2.4 Ion Traffic Through the Membrane	12
2.4.1 The Resting Potential	12
2.4.2 Electrochemical Gradients, Permeability, and Flux	13
2.4.3 Ion Channels: Passive Diffusion	15
2.4.4 Ion Pumps: Primary Active Transport	17
2.4.5 Ion Exchangers: Secondary Active Transport	18
2.5 Experimental Techniques	19
3 HYPOKALEMIC HIBERNATION	22
3.1 The Role of Chloride Transport	24
3.1.1 The Model	25
3.1.2 Methods	30
3.1.3 Results	31
3.1.4 Discussion	36
3.2 The Role of Inward Rectifying Potassium Channels	39
3.2.1 The Model	40

3.2.2	Isoprenaline Eliminates Bistability	42
3.2.3	IRKs Produce Bistability	45
3.2.4	The Dimensions of the Bistable Area	47
3.2.5	Discussion	52
4	THERMAL AND ELECTRICAL MEMBRANE DEFORMATION	55
4.1	Thermodynamics of Membranes	55
4.1.1	Lipid Rafts and the Freezing Transition	56
4.1.2	The Meyer-Overton Rule	57
4.1.3	Boundary Layer Deformation	58
4.2	Electrical Membrane Deformation	58
5	FRACTAL BEHAVIOR IN LIPID PORE KINETICS	60
5.1	Methods and Results	61
5.1.1	Building the Probability Density Histogram	63
5.1.2	Calculating the Kinetic Rate Constants	65
5.1.3	Finding the Power Spectral Density	66
5.2	Theory	67
5.3	Conclusions	72
6	EPILOGUE	75
	REFERENCES	78
	APPENDIX A: CODE FOR CHLORIDE TRANSPORT MODEL	87
	APPENDIX B: DERIVATION OF CHLORIDE PERMEABILITY AND COTRANS- PORTER FLUX	92
	APPENDIX C: CODE FOR COMPUTING PDF, TIME-DEPENDENT TRAN- SITION RATES, AND POWER SPECTRAL DENSITY	95

LIST OF FIGURES

1.1	Phase transitions in ferromagnetic materials.	3
2.1	Early membrane models and images.	7
2.2	Singer and Nicolson's fluid mosaic model of the cell membrane.	8
2.3	Self-assembly of lipids and proteins in water.	9
2.4	Cell membrane composition.	10
2.5	Lipid chemical formula.	11
2.6	Ion channel representation.	15
2.7	A representation of the Na,K-ATPase dynamics.	18
2.8	Types of ion exchangers.	19
2.9	A cell-attached patch clamp configuration.	20
2.10	A typical single channel recording from patch clamp.	21
3.1	Overview of the components of the chloride model.	27
3.2	Results of experiment and theoretical simulation.	33
3.3	Results of isoprenaline experiment and theoretical curve.	44
3.4	Comparison of experiment when IRKs are active with theoretical curve.	47
3.5	A close-up view of the same theoretical curve of Fig. 3.4 with the points of interest highlighted.	48
4.1	Phase properties of lipids at the freezing temperature.	56
5.1	Black lipid membrane experimental setup and data.	62
5.2	Effect of anesthetics on membrane permeability.	64
5.3	The probability density function and kinetic rate constants compared to the theory.	66
5.4	Power Spectral density of current signal in Fig. 5.1(b).	67
5.5	Examples of commonly encountered PDF distributions.	68
5.6	Energy landscape involving the open states of lipid pores.	69
5.7	Lipid pore configurations.	72
5.8	Energy landscape involving the open and closed states of lipid pores.	73
6.1	Overview of ion traffic and ATP production in the animal cell.	76

LIST OF TABLES

2.1 Concentrations of the most prominent permeable ions in a typical mammalian muscle
cell. 13

3.1 A list of parameter values to fit the experimental data depicted in Fig. 3.2. 34

LIST OF ABBREVIATIONS, SYMBOLS, UNITS, AND CONSTANTS

0.1 Abbreviations

ADP	adenosine diphosphate
ATP	adenosine triphosphate
Ba ²⁺	barium
BLM	black lipid membrane
Ca ²⁺	calcium
Cl ⁻	chloride
DNA	deoxyribonucleic acid
DOPC	dioleoyl phosphatidylcholine
DPPE	dipalmitoyl phosphatidylcholine
EM	electron microscopy
GABA	γ -aminobutyric acid
GABA _A R	γ -aminobutyric acid receptor A
GHK	Goldman-Hodgkin-Katz
GLUT1	glucose transporter 1
IRK	inward rectifying potassium channels
K ⁺	potassium
KCl	potassium chloride
Mg ²⁺	magnesium
MSOGH	Millhauser, Salpeter, Oswald and Goychuk and Hänggi
Na ⁺	sodium
PDF	probability density function
pH	potentiometric hydrogen ion concentration
P _i	inorganic phosphate
TRP	transient receptor potential

0.2 Symbols

Symbol	Meaning (Units)	Page
α_X	stoichiometry coefficient for pump	26
β_X	stoichiometry coefficient for cotransporter	26
γ	line tension (J/m)	72
ε	sensitivity of IRK open/closed distribution	45
λ	effective sampling rate (Hz)	71
ϕ	electrical potential (V)	14
τ	characteristic relaxation time (s)	94
B	cell volume (μm^3)	29
C	total extracellular concentration of permeable solutes (mM)	42
δC	chemical imbalance across membrane (mM)	41
C_m	specific membrane capacitance (F/cm ²)	29
C_n	n^{th} closed state	73
$[\text{Cl}^+]_{\text{i}}$	intracellular chloride concentration (mM)	24
$[\text{Cl}^+]_{\text{o}}$	extracellular chloride concentration (mM)	24
c_P	heat capacity (J/K)	58
d	diameter of cylindrical muscle cell (μm)	94
D	diffusion constant (cm ² /s)	14
E	energy (J)	58
E_{Cl}	chemical potential for chloride (mV)	13
E_{K}	chemical potential for potassium (mV)	13
E_{Na}	chemical potential for sodium (mV)	13
f	frequency (Hz)	60
$f(t)$	probability density function (s ⁻¹)	65
H	enthalpy (J)	58
$I_n(t)$	Modified Bessel function of order n	71
j	index for PDF bin number	65
J_{cot}	cotransporter flux (mol/cm ² s)	26

J_{cot}^0	activity of cotransporter (mol/cm ² s)	26
J_P	flux of Na,K-ATPase (mol/cm ² s)	26
J_P^{Max}	activity of Na,K-ATPase (mol/cm ² s)	26
J_X	channel flux of ion X (mol/cm ² s)	28
$[K^+]_i, K_i$	intracellular potassium concentration (mM)	13
$[K^+]_o, K_e$	extracellular potassium concentration (mM)	13
K_e^{avg}	center of bistable region (mM)	48
$K_e^{d \rightarrow h}$	concentration at depolarized-to-hyperpolarized switch (mM)	47
$K_e^{h \rightarrow d}$	concentration at hyperpolarized-to-depolarized switch (mM)	47
ΔK_e	width of bistable region (mM)	48
K_m^X	Michaelis-Menten constant for ion X (mM)	26
k_p	pump activity (mol/cm ² s)	41
k_i	kinetic rate constant for i^{th} PDF (Hz)	66
$k(t)$	time-dependent kinetic rate constant (Hz)	65
L	membrane thickness (nm)	14
$[Na^+]_i, N_i$	intracellular sodium concentration (mM)	13
$[Na^+]_o, N_e$	extracellular sodium concentration (mM)	13
N	total number of states	70
$N(j)$	number of counts in bin j	65
N_{total}	total number of data points in current signal	65
O_n	n^{th} open state	69
Osm	osmolarity of the medium (Osm)	34
Osm_0	Osmolarity of the medium with no cotransporter flux (Osm)	34
OsmSense	strength of cotransporter (1/cm ² s)	34
$P(t)$	probability pore stays open for time t	70
p_n	probability of occupying open state O_n	70
P_X	permeability of ion X (cm/s)	28
\bar{P}_K	permeability constant of IRKs (cm/s)	28
P_0	permeability of non-IRK potassium channels (cm/s)	28

$P_{\text{IRK}}^{\text{max}}$	maximum permeability of IRKs (cm/s)	45
q	voltage from the charge of a mole of monovalent ions (V/M)	29
r	radius of pore (nm)	72
r_0	minimum pore radius (nm)	72
S	entropy (J/K)	58
S	cell surface area (μm^2)	29
t	time (s)	29
t_i	bin width for i^{th} PDF (s)	65
T	temperature ($^{\circ}\text{C}$ or K)	13
T_m	melting temperature ($^{\circ}\text{C}$ or K)	56
U	dedimensionalized transmembrane potential	14
\tilde{U}	modifies the IRKs open/closed switch point	45
ΔU	height of bistable region	48
U_{avg}	dedimensionalized voltage at center inflection point	48
U_{dep}	dedimensionalized voltage at depolarized-to-hyperpolarized switch .	48
U_{hyp}	dedimensionalized voltage at hyperpolarized-to-depolarized switch .	48
U_{max}	hyperpolarization factor	44
V_0	voltage of impermeable intracellular ions (mV)	30
V_h	voltage where IRKs open/closed ratio is unity (mV)	28
ΔV_h	modifies the IRKs open/closed switch point (mV)	28
V_s	sensitivity of IRK open/closed distribution to voltage changes (mV)	28
V_m, V	transmembrane voltage (mV)	14
z, z_j	value of ionic charge	14

0.3 Units

μM	micromolar	10^{-6} M
μF	microfarads	10^{-6} F
Ω	ohms	
$^{\circ}\text{C}$	degrees Celcius	
cm	centimeter	10^{-2}m
dm	decimeter	10^{-1}m
Hz	hertz	
K	degrees Kelvin	
kg	kilograms	
L	liters	
mM	millimolar	10^{-3}M
mV	millivolts	10^{-3}V
mol	moles	
mol%	percentage of moles	
mOsm	milliosmoles	
nm	nanometer	10^{-9}m
Osm	osmoles	
pA	picoamps	10^{-12} A
pmol	picomoles	10^{-12} mol
pS	picosiemens	10^{-12} S
s	seconds	
V	volts	

0.4 Constants

ε_0	permittivity of free space	$8.854 \times 10^{-12} \text{ F/m}$
ε_w	relative permittivity of water	81
F	Faraday's constant	$9.6485 \times 10^4 \text{ C/mol}$
k_B	Boltzmann's constant	$1.38 \times 10^{-23} \text{ J/K}$
R	gas constant	8.31 J/K mol

CHAPTER 1: COMPLEXITIES, HYSTERESIS, AND PHASE TRANSITIONS

Over the history of life, there has been an apparent increase in the maximum level of complexity of organisms. With more complexity, the ability to distribute tasks to different subcomponents provides a selective advantage. Higher forms of life organize into tissues with specialized assignments which are then composed of different cells. On the cellular level, there is even more division of labor. Throughout this entangled biological network functions are coupled at multiple levels making the whole undeniably greater than the sum of the parts. The cell membrane is no exception. It is apparent from the multitude of specialized macromolecules that take the form of channels, signalers, receptors, filters and energy-expending transporters that life at an interface is convoluted and perplexing.

To understand underlying mechanisms of interconnected networks, one normally assumes a reductionist point of view and starts with understanding each component to determine the behavior of the system (Solé and Goodwin, 2000). What happens when we understand the basic structures and functions of the components, but these give rise to unpredicted phenomena? A complete understanding of hydrogen and oxygen does not explain the fluid dynamics of water. Yet even with chaos and unpredictability from stochastic processes, order can emerge.

Complexity tends to be present with nonlinear dynamical systems. Some systems can be modeled by continuous functions yet give rise to discontinuous solutions. With discontinuity, there exist critical points where the solutions appear or disappear. We may also find ranges in parameter space where the state of the system can be in either one of two or more possible configurations. A bistable system is one with two possible stable solutions with the same parameters. When there are two solutions, the state of the system depends on the history, so that it is not always possible to determine its state given the parameters that describe it. This phenomenon is called hysteresis, which in Greek means “deficiency” or “lagging behind”. Hysteresis can be related logically to a set-reset flip-flop circuit element. By cross-coupling two inverting elements, the state of the outputs can be changed by allowing either input to be high while the other is low. However, when both inputs are set low, the previous state will be retained. This allows the circuit to hold memory. A jump to a new state can be thought of as a first order phase transition. Within the phase transition

region there is a coexistence of several states, but beyond this region only one state exists.

The archetypal physics example that has hysteresis and bistability is the Ising model. This is a simplified description of a ferromagnetic material. A ferromagnetic material has the ability to remain magnetized even after an applied magnetic field has been removed unlike a paramagnetic material which has an induced magnetization only in the presence of an external field. In the model the atoms in the material interact by spins which can be pointed up or down. Each spin is influenced by the external magnetic field, H , and also by its nearest-neighbors. The Hamiltonian, \mathcal{H}_o , for this system is given by:

$$\mathcal{H}_o = -H \sum_i \sigma_i - \frac{J}{2} \sum_{(i,j)} \sigma_i \sigma_j \quad (1.1)$$

where the spin σ_i (or σ_j) equals +1 for “up” and -1 for “down”. J is the exchange interaction which simplifies the system by falling off rapidly as separation between spins is increased.

For ferromagnets $J > 0$, indicating that parallel alignment leads to a lower and therefore preferred energy state. At temperatures below the Curie temperature, the material will show a magnetization in one direction or another, but above this critical temperature the thermal energy overwhelms the spin interaction leading to no net magnetism (cf. Fig. 1.1(a)). The transformation to paramagnetism at the Curie point represents a second order (continuous) phase transition.

A ferromagnetic material also has the ability to maintain magnetization once the magnetic field has been removed. Once the domains of the material are oriented in one way, it takes some energy to reverse the field. This is what makes ferromagnetic materials good for magnetic memory. As the magnetic field alternates, the magnetism traces out a hysteresis loop, which shows how the history takes effect on the magnetism of the material (cf. Fig. 1.1(b)).

The area of the hysteresis loop is related to the amount of energy required to reverse the field. Different materials are used to take advantage of this particular consequence of interaction with alternating magnetic fields. To this effect, materials with wide hysteresis loops such as hard iron are used for permanent magnets and memory devices whereas materials with narrow hysteresis loops such as soft iron are used when its desirable to alternate the magnetic field with minimal energy loss as in transformers and motor cores. The discontinuous jump in the direction of the material’s magnetism represents a first order phase transition. Near the phase transition the spins rearrange

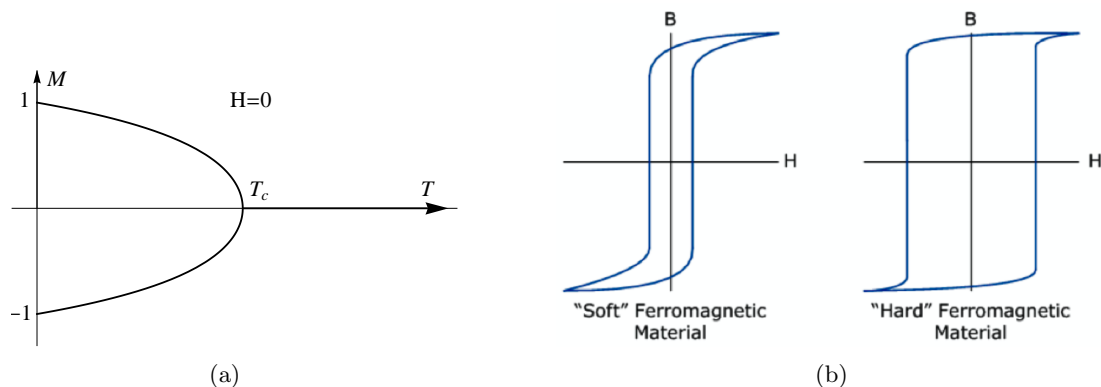


Figure 1.1: Phase transitions in ferromagnetic materials. (a) Magnetization (M) versus temperature (T) of a ferromagnetic material. At low temperatures ($T < T_c$) there are two stable states and at high temperatures ($T > T_c$), there is one stable state. Loss of magnetization occurs at the Curie temperature, T_c , and there is then a second-order phase transition. (b) Hysteresis loops for hard and soft ferromagnetic materials: The magnetization of the material (B) versus the applied magnetic field (H) is plotted. There is a range in H in which there are two stable B states. There are critical points in H , in which the B of the material will switch to another stable state. The switch in direction represents a first order phase transition. Figure from Storr (2010).

themselves in a scale-invariant manner so that the spins behave like a row of dominos where one fall brings down all the others (Gisiger, 2001).

What these examples have in common is that there are critical points in which the system essentially switches to a new state. A small change in one parameter will at some point induce a large change in another parameter. In the following discourse, these ideas will appear when dealing with ion traffic through the cell membrane. There are two related but separate problems that involve emergence of order in the far from equilibrium, self-organized structure that the cell membrane is. Chapter 2 is a brief introduction to membrane anatomy and ion transport through specialized proteins. Maintaining homeostasis inside the cell through ion transport is a complex process and new conditions for stability may be required when the cell encounters a stressful environment. Chapter 3 is a presentation of how such changes in the extracellular environment reveal a hysteresis loop when the cell makes an apparent switch to a new steady state. Models are created to account for the bistability. In Chapter 4, thermal and electrical aspects of membranes are discussed. Changes in temperatures and electric fields can affect the permeability of membranes, not through the specialized protein structures but through the bulk fluid part of the membrane. This second introduction will lead into the problem of Chapter 5. In this second problem, quantized currents are found when electrically stimulating a membrane at or near its phase transition. An

analysis of the conductance times reveals fractal behavior in the form of $1/f$ noise. A theoretical basis and a physical explanation for the noise will be proposed. Chapter 6 concludes this work with a broad overview.

CHAPTER 2:

THE MEMBRANE AS A BARRIER AND A GATEWAY

The cell membrane is the interface between a single unit of life and its environment. The cell's stability relies on a consistent cytoplasmic environment regardless of fluctuating external conditions. Essential proteins and DNA must be kept in and harmful substances like viruses and toxins must be kept out. Nutrients are taken in and waste is discarded through the membrane. It must maintain structure with the connected cytoskeleton and be able to dynamically change shape in the course of mitosis and cell fusion. Communication occurs through the membrane via chemical and electrical signaling through receptors, binding sites, endocytosis and exocytosis. The cell responds to the environment by allowing selective transmembrane movement of water and ions. Ion transport through cell membranes is involved in volume regulation, homeostasis, propagation of action potentials, and setting up concentration gradients to use as a secondary source of energy.

All living cells have a resting negative electrical potential from inside the cell to the outside of the cell. The transmembrane potential is the result of an imbalance of charged molecules that is maintained primarily by a membrane barrier which separates the cell from its environment and by the use of energy to drive pumps. Charge differences ensue despite a steady flow of ions through a complex system of channels, pumps and exchangers. This chapter will deal with membrane structure, composition, and the basic mechanisms of ionic transport.

2.1 A Brief History of Membrane Models

Before the improved resolution of the microscope in the 17th century, the fact that all life is made of cells was not established. With the higher resolving compound microscope, the thicker cell walls in plants were easily observed but the thinner cell membranes of animal cells, lacking a cell wall, could only be assumed at this time. Any advances on the structure of the membrane had to be made indirectly. Some observations would have to be made before a concise model of the membrane would be introduced.

In the mid-19th century three botanists, Karl von Nageli, Karl Cramer, and Wilhelm Pfeffer, gathered evidence to distinguish the individual cell from its surroundings in their experiments using plant tissue. They noticed the protoplast would shrink from the cellulose wall in hypertonic solutions and expand back upon dilution of the external bath. This observation led to the notion

of a semi-permeable membrane and the restoration of osmotic balance by the movement of water. At the end of the 19th century, chemical analysis had already shown that membranes were made of phospholipids and cholesterol. Ernest Overton further elucidated some aspects of membrane-solution interactions with his oil solubility studies. He needed to find substances that would be readily absorbed into plant cells to complete his research on heredity. Overton classified the permeability of hundreds of organic solutes by their distribution ratio between water and oil and found that nonpolar substances would pass more quickly through the membrane into the cell. This discovery was quite contrary to the prevalent view at the time that the membrane was impermeable to almost anything but water (DeWeer, 2000). The next big advancement in the understanding of biomembranes came from Irving Langmuir circa 1917. Langmuir created a trough which allows assembly, compression and expansion of fatty acids. He found that these molecules at an air-water interface would assemble into a monolayer and become oriented with polar groups in contact with the water and nonpolar hydrocarbon chains away from the water. This experiment established how lipids self-assembled into organized sheets with a preferred orientation. With these pieces, a membrane model was ready to be put together.

In 1925, Gorter and Grendel were able to correctly identify the basic structure of lipid bilayers. Lipids from red blood cells were extracted with acetone and other solvents and placed in a modified version of the Langmuir trough allowing surface area measurement of the monolayer. The monolayer's surface area was twice as big as the cell's surface area, leading them to the notion of a double lipid layer, or bilayer (cf. Fig. 2.1(a)) (Gorter and Grendel, 1925). Chemical analysis also showed the presence of proteins in the membrane, which led to a series of models that modified the order and structure of membrane components. The Danielli-Davson model membrane has layers of globular proteins adsorbed to the surface of the lipid bilayer (cf. Fig. 2.1(b)) which were incorporated to account for the low surface tension of the membrane (Danielli and Davson, 1935). Electron microscopy (EM) emerged in the late 1950's and continued this lipid-protein sandwich idea by the observance of dark electron dense bands on each side of the membrane (cf. Fig. 2.1(c)). A notable experimentalist, J. D. Robertson, prepared and studied electron micrographs of membranes of different cells and organelles. His "unit membrane" theory was meant to convey the universality of the bilayer structure. The same arrangement appeared from cell to cell and within as the double layer of the nuclear envelope appeared to look just like two stacked layers of the

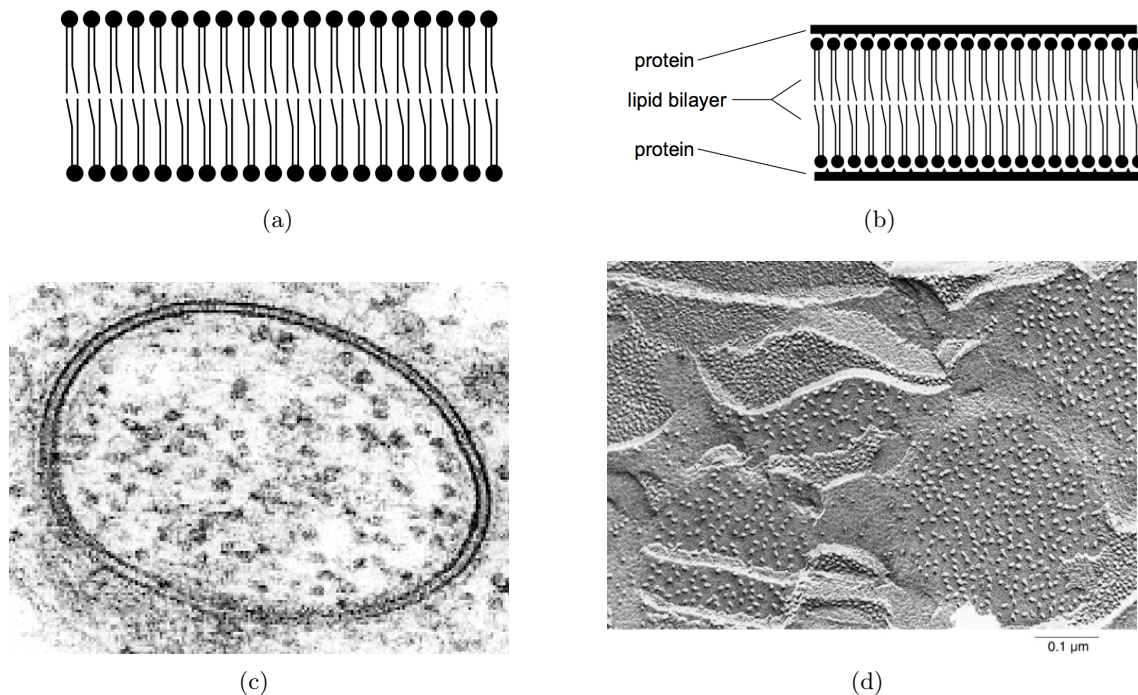


Figure 2.1: Early membrane models and images. (a) A lipid bilayer representation: lipids in water form double-layered sheets with the nonpolar lipid tails facing inward away from the water and the polar heads pointing outward. (b) The Danielli-Davson model. The lipid bilayer is sandwiched by thin layers of globular proteins. (c) Transmission electron micrograph of a lipid vesicle. The signature “train track” appearance of the membrane is visible. Figure from Wikipedia (2008). (d) Freeze-fracture electron micrograph of a cell membrane showing protrusions that became identified as membrane-spanning proteins. Figure from Staehelin (2002) with permission from author.

membrane surrounding the cell (Robertson, 1957). Robertson incorrectly identified the dark outer regions of the membrane as layers of proteins as Danielli and Davson did, but this later turned out to be the negatively charged phosphate groups of the lipid molecules. He did correctly deduce that the distribution of lipids from the inner leaflet to outer leaflet slightly differed in composition.

The freeze-fracturing EM technique of Branton in the 1960s was to first freeze and split the membrane along its two layers. After being shadowed with a heavy metal and coated with carbon, the biomaterial is chemically digested to leave a topological replica of the inner membrane surface. The EM showed the presence of raised and lowered portions lying in between the two layers (cf. Fig. 2.1(d)) indicating that some membrane components spanned the entire bilayer. Most people at the time believed that the technique was producing an artifact (Tosteson, 1989), but via X-ray crystallography, Singer and Nicholson found growing evidence of integral proteins that extended through the body of the bilayer. Hydrophobic regions in proteins in the form of α -helices were

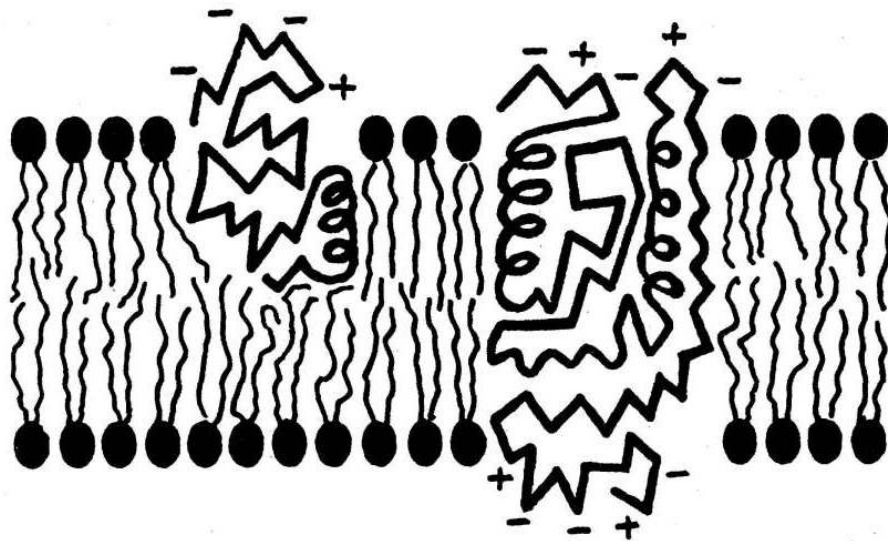


Figure 2.2: Original figure from Singer and Nicolson (1972) depicting a membrane cross section with integral proteins in the phospholipid bilayer. Ionic and polar portions of the proteins are indicated with + and - symbols. These portions contact the aqueous solutions surrounding the lipid bilayer. The membrane spanning region of the protein is nonpolar and therefore lacks charge as indicated by the absence of + and - symbols. Figure from Singer, S., and Nicolson, G. "The fluid mosaic model of the structure of cell membranes." *Science* 175: (1972) 720-731. Reprinted with permission from AAAS.

recognized which determined that integration of proteins through the membrane was both possible and probable (Singer and Nicolson, 1972). The model of Singer and Nicolson is referred to as the "fluid mosaic model" and underlies the current structural view of the membrane (cf. Fig. 2.2). Proteins that could easily be separated from the membrane because of attachment to just one leaflet of the bilayer were termed peripheral. Integral proteins, on the other hand, required more drastic measures like the use of detergents to be set free as they span the whole bilayer with hydrophilic regions on both sides and a hydrophobic region within the core. The fluid mosaic model is the basic model preferred by biologists today.

2.2 *The Hydrophobic Effect*

Water has a unique ability to be a universal solvent to many solutes. At the same time, it is apparent that some substances do not mix with water such as oils and fats. These substances are amphiphilic, meaning they contain both a polar hydrophilic ("water-loving") region and a nonpolar hydrophobic ("water-fearing") region. Rather than engage in van der Waals interactions with nonpolar or amphiphilic substances, water molecules favor maximum hydrogen bonding with each other. Membrane lipids, proteins, and sterols are all amphiphilic molecules that tend to aggregate and adjust their orientations and conformations into shapes that are more entropically

favorable. In order to minimize the surface area that water must form a shell around, lipids in water form liposomes, micelles, and bilayers (cf. Fig. 2.3(a)). Sterols are mostly nonpolar and sit inside the bilayer core but expose their hydrophilic portion to the exteriors. Proteins are composed of a long chain of amino acids which have varying degrees of polarity. They fold in a way that minimizes hydrophobic interactions with the surrounding aqueous environment (cf. Fig. 2.3(b)).

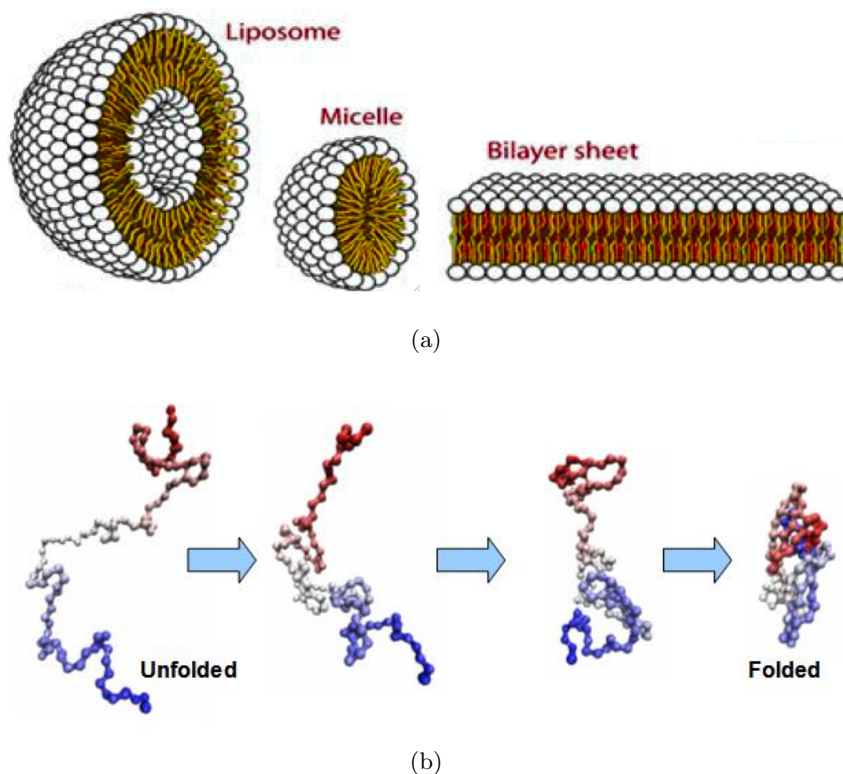


Figure 2.3: Self-assembly of lipids and proteins in water. Figure from Wikipedia (2008). (a) Lipids in water form liposomes, micelles, and bilayers to minimize interactions of hydrophobic tails with water. (b) Proteins in water or incorporated into the cellular membrane have preferred folded conformations that shield nonpolar groups from aqueous interactions. Figure from Kavraki (2007).

The bilayer, however, is not just a flat sheet of lipids with embedded proteins as the fluid mosaic model suggests. Mouritsen and Bloom in 1984 introduced the concept of hydrophobic mismatch at the boundaries between proteins and lipids which leads to small changes in membrane thickness (Mouritsen and Bloom, 1984). The hydrophobic surface of membrane proteins may be smaller or larger than the surrounding bulk lipid. Membrane elements can compensate in several ways to create a smooth interface at the boundaries of mismatched membrane elements. There is an energetic cost of changing the thickness of the lipid bilayer but this cost lessens with protein aggregation. By

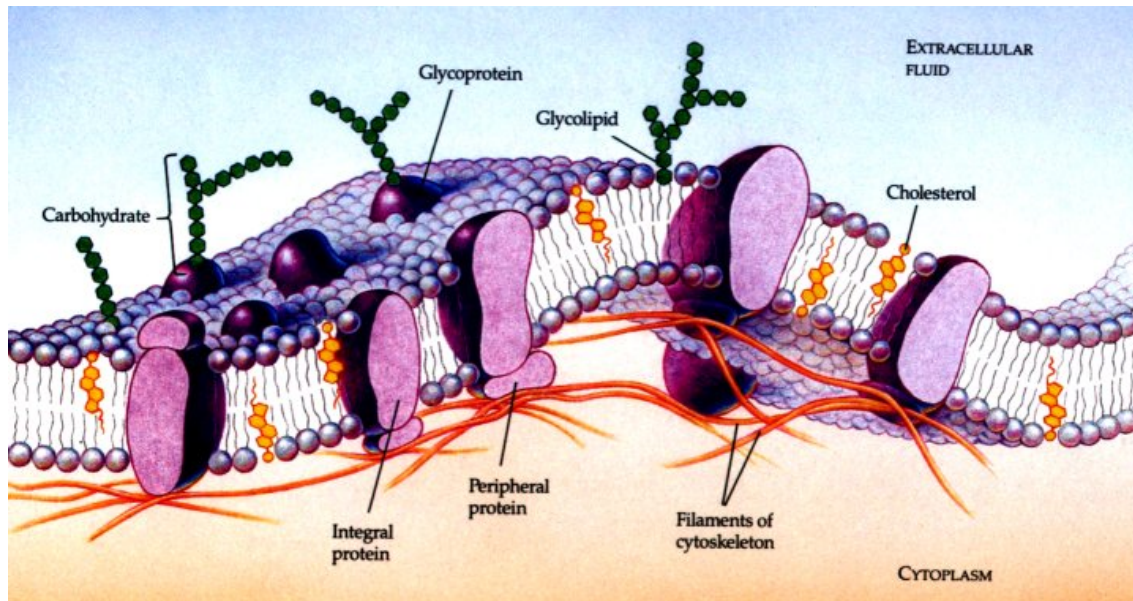


Figure 2.4: The major components of a cell membrane are depicted here. Figure from Dekker (2006).

also tilting and/or rotating lipids within the bilayer or alpha helical domains within the membrane proteins, the effective length difference at an interface may adjust to minimize any mismatch.

2.3 *Bilayer Composition and Organization*

Biomembranes are made of different compositions of hundreds of lipids and proteins along with sterols and carbohydrates. A typical representation is shown in Fig. 2.4, where the embedded proteins freely float through a fluid lipid bilayer. There is variation in the membrane components of different species, tissues, cells and membrane-enclosed organelles within the cell. There is also asymmetry from one side of the membrane to the other that presumably accounts for different environments with different functional requirements.

All of the lipids making up cell membranes are amphiphilic. There is a large variety of lipids that differ in head groups and fatty acid chain lengths. The most common lipids are phospholipids named after the phosphate group in the polar head region (cf. Fig. 2.5). The phosphate is esterified to a glycerol which is esterified to two nonpolar fatty acid chains (called the hydrophobic tails). The phosphate is bonded on the other side usually to an alcohol or sugar, and most common head groups in animals are choline and ethanolamine (Yeagle, 1987). Chains usually have from 12 to 26 carbons which may be saturated or unsaturated (Israelachvili, 1985). Saturated fatty acids are free of carbon-carbon double bonds. Unsaturated fatty acids have at least one double bond which

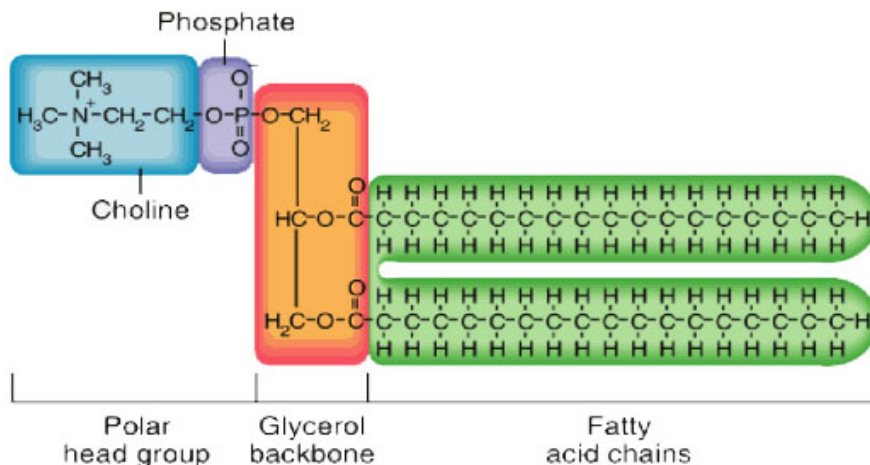


Figure 2.5: Chemical formula for a phospholipid (phosphatidylcholine). Figure from Muller (2009).

introduces a kink in the molecular structure that interferes with close packing of the membrane components.

Membrane proteins constitute about one third of all proteins encoded in the human genome and make up more than half of all current drug targets (Bordag and Keller, 2010). These membrane bound proteins function as ion channels, transporters, signal receptors and anchors to the intracellular cytoskeleton or the extracellular matrix. Proteins may be integral, spanning the entire length of the membrane, or peripheral, located on one side of the bilayer. Integral membrane proteins form mainly alpha-helix bundles but also beta-barrels within the hydrophobic core of the membrane. Peripheral proteins are temporarily attached by a combination of hydrophobic and electrostatic interactions. Hundreds of membrane protein structures have been determined from crystallization followed by X-ray diffraction, though they are notoriously difficult to isolate and purify compared to water-soluble proteins.

Sterols are molecules with four fused carbon rings, a polar hydroxyl group and a hydrocarbon tail. Cholesterols are common in mammalian plasma membranes and are situated with the hydroxyl group near the polar heads and the bulky hydrophobic portion extending within the membrane. This arrangement prevents close packing of the fatty acid tails, helps regulate membrane fluidity, provides mechanical strength, and controls the membrane's phase behavior (Róg et al., 2009).

Lipids and proteins that have carbohydrate extensions are termed glycolipids and glycoproteins. Glycosylation generally occurs on the extracellular side creating long, branching outward extensions.

This “sugar coat”, or glycocalyx is important in cell recognition processes.

2.4 Ion Traffic Through the Membrane

“A room without a door is but a tomb”

Kung, Saimi, and Martinac (1990)

The permeability of a molecule through the lipid bilayer increases with its hydrophobicity. The cell membrane will easily let gases, nonpolar molecules, and small polar molecules through, yet is essentially impermeable to large polar molecules and charged species of any size. The solubility of ions across the membrane is so small that it’s practically immeasurable because so much energy is needed to transfer an ion from water, with a dielectric constant around 80, to lipid, with a dielectric constant from 2 to 5 (Ferreira and Marshall, 1985). In effect, a good barrier is provided but in order to communicate with its environment, the cell needs to allow transport as well. Because ions do not readily move through the lipid bilayer, they require specific structures for transport. The group of transporting structures that has been identified in the membranes of cells is varied. Ions can cross the membrane through proteins in the form of channels, pumps, and exchangers. The action may be passive electrochemical diffusion through a water-filled pore or may require energy for translocation against the electrochemical gradient.

2.4.1 The Resting Potential

Because of its relatively high dielectric constant, water easily weakens ionic bonds. A salt dissolves or a neutral molecule dissociates and ions are formed. Atoms, like sodium and chlorine, become charged by the loss or gain of electrons whereas neutral molecules become charged usually through the loss or gain of hydrogen ions. The ionic composition of both the intracellular and extracellular aqueous environments has a significant impact on the cell’s resting state. Differing concentrations of ions from one side of an electrically resistive membrane to the other set up a separation of charge which induces an electric field across the membrane on the order of millivolts (mV). This transmembrane potential is necessary for survival (Nichols et al., 1992).

By convention a membrane potential is given with respect to an outside potential conveniently set to ground (0 mV). The potential varies according to the type of cell. For instance, human skeletal muscle cells have potential differences of around -75 mV, i.e. the inside has a more negative voltage than the outside. Smooth muscle potentials are more likely to be around -50 mV. Bacteria

		X				
		Na ⁺	K ⁺	Cl ⁻	Mg ²⁺	Ca ²⁺
Concentration	[X] _i (mM)	12	150	7	1.0	0.0001
	[X] _o (mM)	145	4	123	0.5	1.5

Table 2.1: Intracellular ([X]_i) and extracellular ([X]_o) concentrations of the most prominent permeable ions (X) in a typical mammalian muscle cell given in millimolar (mM). Values are adapted from Hille (1992) and Melkikh and Sutormina (2008) at a -75 mV resting potential.

tend to keep a more negative transmembrane potential like -150 mV, but the fungus *Neurospora crassa* maintains a transmembrane voltage in excess of -300 mV (Läuger, 1991).

All cells in our body live in a seawater-like environment. The extracellular bath has high sodium and chloride concentrations and low potassium concentrations. Inside the cell, the concentrations of sodium and chloride are low but the concentration of potassium is very high. The high concentration of negatively charged substances that remain in the interior of the cell like DNA, proteins, and sugars also contribute to the resting potential. Table 2.1 summarizes concentrations of some ions observed inside and outside of a typical skeletal muscle cell. The most permeable ions through the cell membrane during resting conditions are sodium, potassium and chloride.

Unlike resting potentials, excitable cells in muscles and nerves must also allow action potentials. The action potential is basically a traveling rise and subsequent return to normal of the membrane potential. This change in potential is a consequence of brief changes in permeability to certain ions and is necessary for every move and thought we make. This study, however, focuses on the resting potential of cells and how it influences proper maintenance of homeostasis and resting metabolism.

2.4.2 *Electrochemical Gradients, Permeability, and Flux*

Charge imbalance creates a chemical potential that can be related to an electrical potential difference across the membrane. The chemical potential for a particular ion can be determined by the Nernst potential equation (Ferreira and Marshall, 1985; Keener and Sneyd, 1998):

$$E_X = \frac{RT}{zF} \ln \frac{[X]_o}{[X]_i} . \quad (2.1)$$

where R is the gas constant, T is the temperature, F is Faraday's constant, z is the net charge of the ion X, of which $[X]_o$ and $[X]_i$ are the outside and inside concentrations, respectively. When the Nernst potential (Eq. (2.1)) equals the electric potential across the membrane there will be no

net current. Upon crossing this equilibrium potential when increasing or decreasing the membrane potential, the current of that ion reverses direction. For this reason, the Nerst potential is also called the reversal potential.

What is important in determining the net driving force of each ion is the difference between the chemical and electrical forces. Most ions are not at their equilibrium potential in living cells, not just because there are multiple ions involved with different magnitudes of permeability, but because living cells use energy-driven pumps that oppose the drive towards equilibrium. Therefore some ions have a constant diffusive flux across the membrane. The Nernst-Planck electrodiffusion equation defines the net flux per unit area, J , of each ion by combining both electrical and chemical gradients:

$$J = -D \left(\frac{d[X]}{dx} + \frac{zF}{RT} [X] \frac{d\phi}{dx} \right). \quad (2.2)$$

Here D is the diffusion constant, $[X]$ is the ionic concentration at position x across the membrane, and ϕ is the electric potential. The constant $\frac{zF}{RT}$ was defined following Eq. (2.1) and is frequently encountered to dedimensionalize the membrane potential (it has units of V^{-1}). A useful result of this equation can be found when one assumes that the electric field within the membrane is constant (called the constant field approximation). Boundary conditions may be applied for the internal and external concentrations ($[X]_i$ and $[X]_o$, respectively) and the flux at steady state (constant J) is found. The result is the Goldman-Hodgkin-Katz (GHK) current equation (Ferreira and Marshall, 1985):

$$J = -\frac{D}{L} \frac{zFV_m}{RT} \frac{[X]_o - [X]_i \exp(\frac{zFV_m}{RT})}{1 - \exp(\frac{zFV_m}{RT})}, \quad (2.3)$$

where L is the length across the membrane and V_m is the transmembrane voltage. In determining the net flux the permeability is accounted for by the factor D/L , which has the same units as velocity. The permeability through the cell membrane can be related to the number and/or size of open pores.

Low intracellular sodium (Na^+) concentrations and high intracellular potassium (K^+) concentrations assure that the cell can perform some necessary functions such as excitability, secondary active transport and volume regulation (Arispe et al., 1998). Both the chemical and electrical

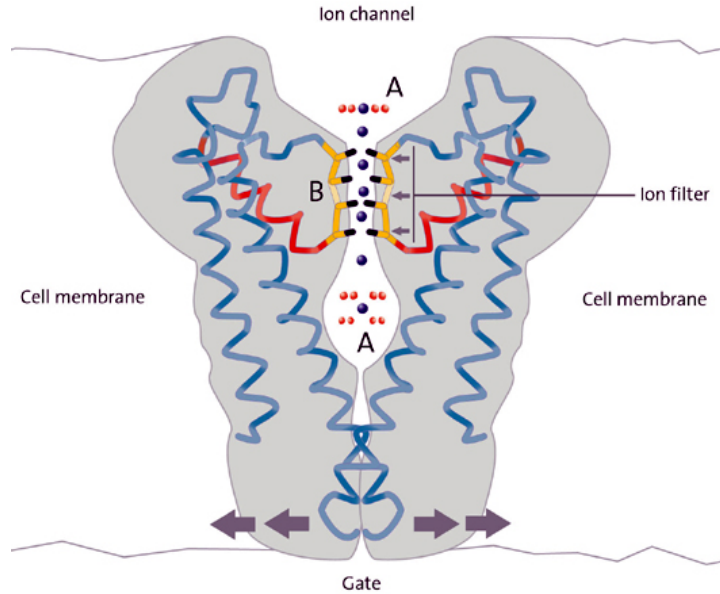


Figure 2.6: The selectivity filter portion of an ion channel may be extremely narrow so that a hydrated ion must even shed its waters to pass through. The ion can then be rehydrated on the other side. The charged residues within the filter and the size provide means for exclusion of other ions from traversing. The gate of the ion channel moves from a closed conformation to an open one when being exposed to a certain stimulus. Figure from Mallery (2007)

gradients drive Na^+ to the inside of the cell. However, Na^+ channels in the membrane are mostly closed (i.e. D/L is small). Conversely, for K^+ the electrical and the chemical forces have opposite directions and almost balance each other out. But under normal conditions a significant fraction of the K^+ channels is open and the ensuing potassium permeability is high (i.e. D/L is large). This sets up a force towards a steady state in which the transmembrane electric potential, V_m , is largely dominated by and remains near the K^+ chemical transmembrane potential.

2.4.3 Ion Channels: Passive Diffusion

Ion channels form highly conducting, hydrophilic pathways for the free diffusion of ions down electrochemical gradients. The proteins that form these channels open and close in response to normal thermal fluctuations and other various triggers. When open, ion channels allow extremely efficient ion transfer rates of around $10^6 - 10^8$ ions/s (Hille, 1992). Most ion channels are at least partially selective to one ion due to surface charge on the pore lining, pore size, and/or orientation of residues within the pore (cf. Fig. 2.6).

Ion channels are essential for many functions including neuronal signaling, muscle contraction, cell volume regulation, and cardiac pacemaking. There are several types of ion channels that vary

in form and function and over 350 genes have been identified to code for channel proteins. Because ion channels are so essential to life, channelopathies are common and widespread (around 40 known hereditary channelopathies). Channelopathies are diseases or disorders that affect the function of ion channels or the molecules that regulate them. Some channelopathies include cystic fibrosis, long QT syndrome and periodic paralysis disorders. Disfunctional ion channels are also related to seizures and epilepsy.

Voltage-gated channels open and close in response to a change in the transmembrane potential. These channels are critical in nerve and muscle cells for establishing voltage thresholds during an action potential but are common in many cell types. The electrical coupling may be due to a structural rearrangement of the whole protein or the movement of a voltage-sensing charged side group, which results in either blocking or opening the channel. Inward and outward rectifiers are voltage gated channels that selectively pass more current in one direction like a diode. If the electrochemical gradient drives the current too far in the opposite direction, the channels close.

Some channels open or close in response to the binding of a small signaling molecule called a ligand. The γ -aminobutyric acid receptor (GABA_AR) becomes activated upon binding γ -aminobutyric acid (GABA), the major inhibitory neurotransmitter in the central nervous system. Upon activation, the channel changes conformation and allows selective conduction of Cl^- through its pore. Ligand-gated channels are also important in the olfactory system, the visual system, pacemaker cells, and absorption in the kidney.

Other kinds of gating include mechanosensitive gating, light-activated gating, and temperature-controlled gating. Mechanosensitive channels respond to mechanical stimuli by opening or closing when encountering a pressure wave or a change in membrane tension. They are thought to be responsible for a variety of special functions including touch sensors in the skin, sound sensors in the inner ear and stretch sensors in the bladder. Channelrhodopsins are an example of light-activated ion channels that open and close in response to photonic stimulation. These particular channels are found in green algae and control phototaxis, which is light activated movement. Thermo-TRP (transient receptor potential) ion channels respond to distinct thermal thresholds. It has been reported that even just *the sensation* of hot or cold from capsaicin (the active ingredient in chili peppers) and mint-derived menthol give thermosensitive responses that can be traced to these channels (Dhaka et al., 2006).

2.4.4 *Ion Pumps: Primary Active Transport*

When the transfer of ions “uphill” against the electrochemical gradient is coupled to an energy source, the carrier is referred to as a pump and the process is called primary active transport. Most ion pumps are electrogenic, that is, the ion translocation involves a net electric charge. Pumps are important in volume regulation, homeostasis and maintaining concentration differences for secondary active transport (Läuger, 1991). Pumps are never open to both sides of the membrane at once but rather cycle through different conformations to allow exchange at each interface.

Energy sources for ion pumps include ATP hydrolysis, redox reactions, and light. The light driven pump, bacteriorhodopsin, is one of the most simple of known ion pumps (Läuger, 1991). Upon excitation with light, the protein undergoes a series of conformational changes and protonation/deprotonation steps that eventually result in proton transfer to the outside of the cell. Thus, a proton gradient is set up that can be used to synthesize ATP (adenosine triphosphate), the universal energy currency for all living things. Similar proteins are found in the visual pigments of retinal photoreceptors (Osorio and Nilsson, 2004; Hayashi et al., 2009).

The most prevalent pump in animal cells, the sodium-potassium pump (or Na/K-ATPase), is the main contributor to the maintenance of the transmembrane potential against the constant diffusive leak of ions through channels (Läuger, 1991). At each cycle, the pump hydrolyzes ATP into the products ADP (adenosine diphosphate) and inorganic phosphate (P_i) and uses the released energy to move three sodium ions out of the cell and two potassium ions into the cell. The detailed mechanism is outlined in Fig. 2.7. This active transport consumes 20-80% of the cell’s ATP production depending on the extent of its electrical activity (Boutilier, 2001). When ATP concentrations are low, the pump can even run backwards to generate ATP from ADP and P_i using ionic concentration gradients (Läuger, 1991).

The earliest function of ion pumps in the evolution of life may have been osmoregulation (Läuger, 1991). Cells of plants, bacteria, fungi and algae are armed with a rigid cell wall that prevents swelling and lysis caused by the influx of ions and water. Ion pumps in animal and protazoan cells, which lack a cell wall, help maintain volume by using energy to compensate for any leak that compromises the internal and external osmotic balance. Proton pumps are prevalent in primitive cells indicating that another function for pumps is for pH regulation. In excitable cells, the maintenance

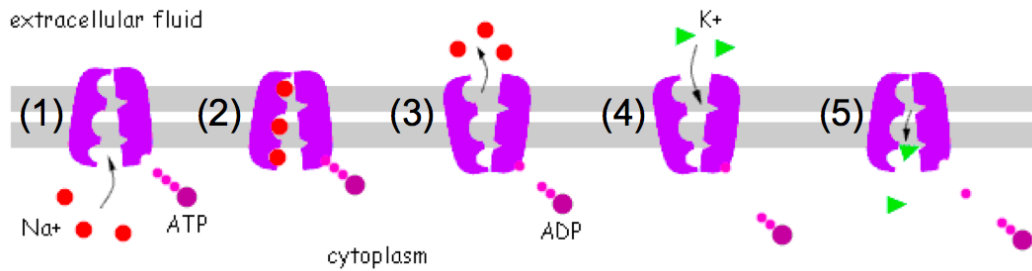


Figure 2.7: A representation of Na,K-ATPase dynamics. When open to the cytoplasmic side of the membrane (1), the molecule has selective binding for sodium ions (2). Upon hydrolysis of ATP into ADP and P_i (3), a conformation change takes place which opens the protein to the extracellular side. In this new conformational state, sodium is released and there is now a greater affinity to bind potassium ions (4). With phosphate release, the protein makes another conformational change to the previous state, which has a low affinity for potassium (5) and a high affinity for sodium and ATP binding (1). With each cycle, the Na,K-pump imports two potassium ions and exports three sodium ions. Figure modified from Adams (2007).

of a transmembrane potential by ion pumps may function to keep a large enough capacitance across the cell membrane for rapid discharge during excitation.

2.4.5 Ion Exchangers: Secondary Active Transport

Ion exchangers are driven by concentration gradients. This type of transport is termed secondary active transport because the energy stored in a concentration gradient is primarily created by an ion pump. By coupling the ion transport to an energetically downhill movement as in a concentration gradient, an exchanger can move other ions against electrochemical gradients. Many exchangers are driven by the large sodium gradient which is constantly maintained by Na,K-ATPase. An illustration of the various types of ion exchangers is shown in Fig. 2.8.

Uniporters allow facilitated diffusion of a molecule down its concentration gradient. Facilitated diffusion means that an already thermodynamically favored diffusion reaction will be accelerated. The glucose transporter GLUT1 is a uniporter that catalyzes the movement of glucose from the normally high external concentration to the low internal concentration where it eventually will be broken down to synthesize ATP.

Antiporters involve two or more substances moving in opposite directions like the sodium-calcium exchanger (Na^+/Ca^{2+} exchanger). The Na^+/Ca^{2+} exchanger uses the energetically downhill import of three sodium ions to drive the export of one calcium ion (Ca^{2+}) against both the chemical and electrical forces that drive it inward. This appears to be essential for getting rid of large amounts of internal Ca^{2+} in a short time, as is the case following an action potential.

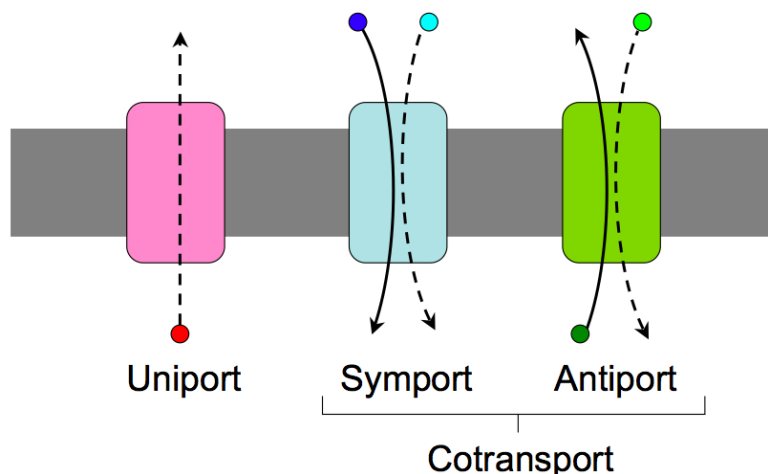


Figure 2.8: Ion exchangers use concentration gradients as the energy source to move ions and include uniporters, symporters and antiporters. Transport of an ion down its electrochemical gradient is represented with a dashed arrow and transport against the electrochemical gradient is represented with a solid arrow. Uniporters involve the facilitated diffusion of one ion across the membrane down its electrochemical gradient. Cotransporters involve the transport of at least one ion down its electrochemical gradient to facilitate the transport of at least one ion against the electrochemical gradient. Cotransport may be either in the same direction (symport) or in opposite directions (antiport).

Symporters involve two or more substances moving in the same direction such as the Na,K,2Cl-cotransporter. This cotransporter uses the inward passage of one Na^+ down its electrochemical gradient to drive one K^+ and two Cl^- 's to the interior of the cell. This transport gives a zero net charge translocation and only imports ions into the cell which acts to increase its osmotic value. Two varieties of the Na,K,2Cl-cotransporter exist: one is found strictly in the kidney, which extracts these electrolytes from the blood for reabsorption, and the other one is widely distributed in many cells and is involved in volume regulation and secretion processes.

2.5 *Experimental Techniques*

What we have learned of ion transport mechanisms came mainly from techniques that began to develop in the 1940's and 1950's which use glass microelectrodes, voltage and current clamp setups, and radioisotopes. Glass electrodes can be stretched into a fine ($\sim 1 \mu\text{m}$) tip that easily penetrates a single cell. When the microelectrode is filled with an appropriate ionic solution and connected to an amplifier, the potential difference across the membrane can be measured. With the voltage clamp the microelectrodes are connected to a negative feedback control that keeps the voltage constant. The resulting current is then measured. This is a good technique to quantify the voltage dependence of many ion transporters. A current clamp, on the other hand, measures the

resulting voltage when a constant current is maintained across a membrane. Radioactive tracer ions can be used to determine flow rates. Such substitution like K^+ with radioactive Rb^+ , which has similar properties and size, can be used to study potassium channels.

The patch clamp was developed in the late 1970's, for which the technique later earned Erwin Neher and Bert Sakmann a Nobel Prize. Patch clamp isolates a patch of membrane containing one or a few channels (cf. Fig. 2.9) by suctioning a micropipette to the cellular surface which forms a high resistance seal in excess of a gigaohm. A silver chloride wire couples the solution in the pipette to the amplifier and can be configured in either a voltage or current clamp setup. The patch clamp made it possible to isolate currents from single channels. Many kinetic schemes for ion channels rely on current recordings from patch clamp (cf. Fig. 2.10) to determine the sequence and duration of the closed and open channel states (Liebovitch and Tóth, 1991; Goychuk and Hänggi, 2002).

There are also a number of blockers and stimulators that have been identified to change the permeability of certain ions through the cell membrane. Selective blocking of channels, pumps or exchangers has the benefit of isolating certain ion fluxes.

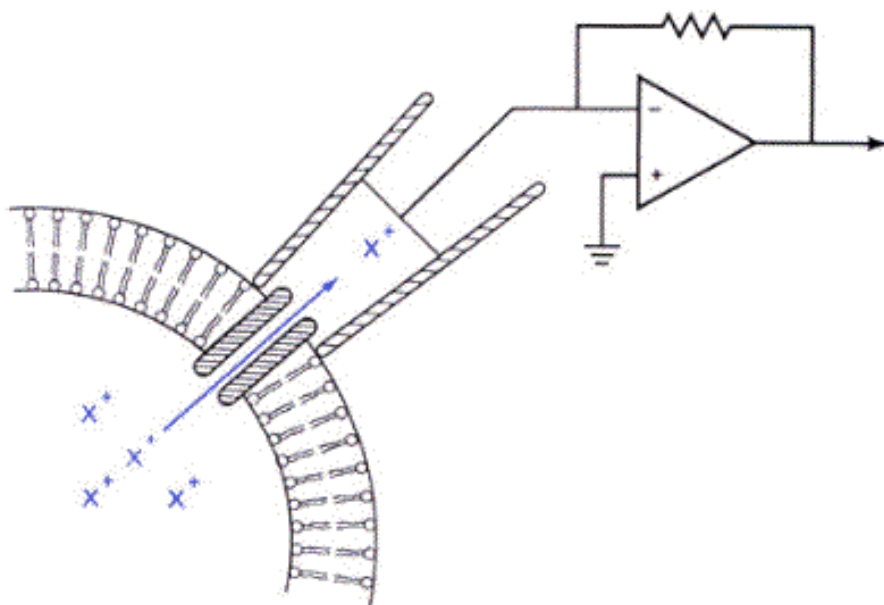


Figure 2.9: A cell-attached patch clamp configuration. The tip of the micropipette is about 1 micrometer in diameter and usually has one or a few ion channels within the patch of membrane. The micropipette makes a high resistance seal with the cellular membrane and an electrode is coupled to the ionic solution within the pipette. The electrode is then connected to an operational amplifier for negative feedback control. This is different than the microelectrode used for intracellular recordings that impales the cell rather than making a seal with the surface of the membrane. Figure from Myers (2008).



Figure 2.10: A typical single channel recording from patch clamp. The quantized currents occur due to two basic ion channel configurations: open and closed. Figure from Wikimedia Commons (2006).

Other experimental methods involve determining function through structure. X-ray crystallography has become invaluable in elucidating structural characteristics of membrane proteins. As X-ray crystallography has characterized hundreds of structures, there is a growing amount of research that uses this information to conduct molecular and stochastic dynamics simulations (Corry et al., 2000; Chung and Kuyucak, 2002). By also characterizing the genetic sequences and tertiary conformations of membrane proteins, one can speculate on the functional mechanics of an ion transporter such as gating and selectivity. Gene sequence analysis helps resolve membrane protein configurations by determining how the protein folds and combines with the bilayer through hydrophobic and hydrophilic interactions of amino acids. Identification of genetically mutant membrane proteins also provides information on specific sequences that are necessary for proper function (Bichet et al., 2004). Likewise, recognizing genetic variations in the proteins of individuals with certain ion transport disorders helps elucidate how the small variations in the gene sequence and protein structure can manifest physiologically (Bubien et al., 1990).

CHAPTER 3:

HYPOKALEMIC HIBERNATION

Environmental stress can be the cause for many cells and organisms to retreat from activity into a sort of “hibernation state” until conditions are more energetically favorable for proliferation (Wharton, 2002). Such “switching off” of activity triggered by an adverse environment can be noticed in the dormancy of persister cells (Lewis, 2007) or sporulation of yeast (Sonenshein, 2000). Biological switches are both common and diverse. Quantitative accounts of such switches in terms of basic physics and chemistry are often reminiscent of the way traditional physics has dealt with phase transitions (Plischke and Bergersen, 1994; Reichl, 1980). Getting a discrete switch in a system with underlying continuous dynamics involves bifurcations, i.e., solutions that emerge and disappear as a parameter is changed. Such bifurcations have been identified in population dynamics and in signaling pathways that involve DNA and/or proteins (Edelstein-Keshet, 1988; Murray, 1993; Ferrell and Machleder, 1998; Qian and Reluga, 2005).

Cells are sensitive to external potassium concentration changes. For potassium the transmembrane electric potential (V_m) and the transmembrane chemical potential (E_K) almost balance each other out. Under physiological conditions a large fraction of the potassium channels is open which helps stabilize the electric potential. Too much potassium (hyperkalemia) in the medium can cause depolarization of the transmembrane potential. With too little potassium in the medium (hypokalemia) a more complicated situation arises. As the concentration of extracellular potassium lowers, the membrane becomes hyperpolarized. Beyond a certain threshold, a switch to a depolarized state is observed to occur in a variety of cell types (Gadsby and Cranefield, 1977; McCullough et al., 1990; Siegenbeek van Heukelom, 1991; Brismar and Collins, 1993; Jiang et al., 2001). This transition appears reversible as potassium is added again to the extracellular medium. However, the switch back to a hyperpolarized state occurs at a higher potassium concentration than the one for which the depolarization occurred. There is an apparent hysteresis. Previous works have shown that these switches do not go via the genome (van Mil et al., 2003; Geukes Foppen and Siegenbeek van Heukelom, 2003; Gallaher et al., 2009).

The study of the control of the transmembrane potential at low extracellular potassium concentrations bears significance for the understanding of hypokalemia. This is a disorder in which the K^+

concentration in the blood becomes low (< 3.5 mM). The ailment often arises acutely in connection with diuretic therapy or renal malfunction (Landau, 2006; Alfonzo et al., 2006). Hypokalemia can also occur as a periodically returning symptom in certain inherited disorders (Jurkat-Rott and Lehmann-Horn, 2006; Struyk and Cannon, 2008). Clinical manifestations of hypokalemia can consist of decreased muscle function and even paralysis. Electrophysiological experiments and models show that, at a sufficiently low extracellular potassium concentration, a second steady state emerges (Siegenbeek van Heukelom, 1994; van Mil et al., 2003). The membrane potential in this steady state is about -60 mV. It has been suggested that the observed paralysis comes about as a result of cells switching to this depolarized state (Geukes Foppen and Siegenbeek van Heukelom, 2003).

In mammalian muscle cells a large part of the potassium permeability is due to the so-called inwardly rectifying potassium channels (IRK). These channels protect the high intracellular potassium concentration through a rectification property: they are mostly open when $V_m \lesssim E_K$ (i.e. when the net force drives K^+ into the cell) and mostly closed when $V_m \gtrsim E_K$ (i.e. when the net force drives K^+ out of the cell). In normal physiological steady state conditions $V_m - E_K$ is slightly above zero. This leads to a steady leak of potassium ions out of the cell.

Intuitively it can be understood that at a hypophysiological $[K^+]_o$, a hyperpolarization is necessary for the transmembrane chemical force on K^+ and the transmembrane electrical force on K^+ to keep canceling each other out. The driving force for potassium ions increases as the hyperpolarization of E_K is larger than the hyperpolarization of V_m . A hyperpolarized V_m also leads to an increased leak of Na^+ and thus requires more “pump work” on the part of the Na,K-ATPase. However, there is a critical point in the dynamics. The pump has a saturation level and there is a critical value of $[K^+]_o$ below which the increased leak of Na^+ into the cell at the more negative membrane potential can no longer be compensated for by pumping activity. A hyperpolarized steady state is then no longer tenable. The increased Na,K-pump activity has also increased the intracellular potassium concentration and thereby $(V_m - E_K)$. When $(V_m - E_K)$ crosses a threshold, the IRKs close and a “switch” to the depolarized state takes place. In the depolarized state V_m is about 60% of what it was in the hyperpolarized steady state. The about tenfold reduction in potassium permeability accounts for a steady state in which the high intracellular potassium concentration is “protected” even though there is a large outward directed driving force, $(V_m - E_K)$, for potassium ions.

In the reference by van Mil et al. (2003) a simpler model was presented that involved only sodium and potassium. That model employed a Michaelis-Menten description for the behavior of the Na,K-ATPase and used simple conductance characteristics for Na^+ -channels and for K^+ -channels (including the IRKs). The eventual dynamical system indeed exhibited a switch from a hyperpolarized state to a depolarized state at low $[\text{K}^+]_o$. The analysis of the model, furthermore, revealed a parameter range where both the hyperpolarized state and the depolarized state constitute stable solutions. Such bistability is also experimentally observed with murine skeletal muscle cells (Siegenbeek van Heukelom, 1991, 1994; Siegenbeek van Heukelom et al., 1996; Geukes Foppen et al., 2002; Geukes Foppen, 2004). A more complete electrochemical model is presented here by also bringing chloride into the picture.

3.1 The Role of Chloride Transport

There is growing research interest in the different channels, transporters and pumps that are involved in chloride transport. However, chloride channel function is currently a subject of a lot of speculation. These channels seem to play a part in regulation of pH, volume homeostasis, transepithelial transport and electrical excitability (Jentsch et al., 2002). Mutations in chloride channels gives rise to thick mucus and excessively salty sweat in individuals with cystic fibrosis. Normally membrane chloride permeability is relatively high and its equilibrium voltage stays near the membrane voltage.

The membrane's permeability for chloride has been reported to be up to about an order of magnitude higher than the permeability for potassium (Bretag, 1987). So, just like for K^+ , for Cl^- the electric potential and the chemical potential almost balance each other out. What keeps the intracellular chloride concentration ($[\text{Cl}^-]_i$) slightly above equilibrium with respect to the extracellular chloride concentration ($[\text{Cl}^-]_o$) is the activity of the Na,K,2Cl-cotransporter. The Na,K,2Cl-cotransporter imports one Na^+ ion, one K^+ ion, and 2 Cl^- ions at each cycle. The electrochemical gradient for Na^+ provides the energy to import the other three ions. The Na,K,2Cl-cotransporter thus couples the transmembrane electrochemical potential of Cl^- to the transmembrane electrochemical potentials of Na^+ and K^+ .

The Na,K,2Cl-cotransporter only imports ions into the cell and because of this it plays a central role in a cell's osmotic regulation and volume homeostasis (Haas and Forbush, 2000; Russell, 2000; Strange, 2004). As such, the cotransporter is also important in the function of the kidney. The

drug bumetanide blocks the Na,K,2Cl-cotransporter very effectively (it is known as a “high ceiling loop diuretic”) and it is frequently administered to patients with excessive accumulation of body fluids, hypertension, and congestive heart failure (Ellison, 2001).

A hyperosmotic media is known to stimulate the Na,K,2Cl-cotransporter (Haas and Forbush, 2000; Russell, 2000; Strange, 2004). Hyperosmolarity occurs when the environment has a higher concentration of solutes on the outside than on the inside of the cell and occurs in dehydration. The highly concentrated solution surrounding the cell has the ability to shrink the cell by losing water to the outside for osmotic balance. The Na,K,2Cl-cotransporter reduces water loss and subsequent volume contraction by moving ions inward to compensate.

A mathematical model for the steady state electrochemical balance of a cell will be presented. The model is tested against electrophysiological measurements on muscle cells. In both the model and in the experiment it will be shown how the electric transmembrane potential at steady state changes as the extracellular potassium concentration, $[K^+]_o$, is decreased to values that are significantly below the physiological level and next increased again back to the physiological level. The pumping of chloride is blocked through the application of bumetanide. After such application the chloride distribution will simply follow the electric potential, i.e. $E_{Cl} = V_m$, and chloride concentrations will no longer affect the steady state membrane potential. The low $[K^+]_o$ regime will be examined with and without bumetanide on the same cell and model predictions are compared with the actual experiment. Next, the medium is made hyperosmotic by the addition of molecules that cannot permeate the cell membrane. The low $[K^+]_o$ regime is examined for one and the same cell with and without such medium hyperosmolarity. Subsequently, model predictions are again compared with experimental outcomes. The model settings are adjusted to fit the experiments and this allows important parameters of pumps and channels to be estimated. The role of Cl^- in the maintenance of the membrane potential is quantitatively and qualitatively assessed.

3.1.1 The Model

Figure 3.1 specifies the components that go into the model which includes the Na,K-ATPase, the Na,K,2Cl-cotransporter and Na^+ , K^+ , and Cl^- channels. Below it will be spelled out how the flow through each of these components depends on concentrations, on the membrane potential and on other constant parameters.

In this model the source of the transmembrane potential is the Na,K-ATPase. This pump moves

2 K^+ ions and 3 Na^+ ions at every cycle (Lauger, 1991). Using second and third order Michaelis-Menten kinetics assumes the reaction rate is limited by the probability of each binding step. The transmembrane flux is represented by:

$$J_P([Na^+]_i) = \alpha_X J_P^{Max} \left(1 + \frac{K_m^K}{[K^+]_o}\right)^{-2} \left(1 + \frac{K_m^{Na}}{[Na^+]_i}\right)^{-3}. \quad (3.1)$$

Here J_P^{Max} is the rate at which the pump cycles when $[Na^+]_i$ and $[K^+]_o$ are at saturating levels. K_m^{Na} and K_m^K are the pump's affinities for Na^+ and K^+ , respectively. The parameter α_X is a stoichiometry factor that has to be entered when expressing actual ion flows. Inward cation flow, by convention, carries a + sign and as such, $\alpha_{Na} = -3$ and $\alpha_K = 2$. The activity of the pump also depends on V_m , but for this range of V_m its variations are small. So to keep the model simple and to limit the number of adjustable parameters this dependence is neglected. Throughout the experiments the $[ATP]/([ADP][P])$ ratio is buffered at a saturating level and it therefore does not figure in Eq. (3.1).

Parameters of the Na,K,2Cl-cotransporter that are useful for the model have not been determined in the literature. As the cycle of the Na,K,2Cl-cotransporter does not involve net transport of charge, a simple assumption is made that the cycling frequency of the Na,K,2Cl-cotransporter is proportional to the sum of the transmembrane chemical driving forces of the involved ions:

$$J_{cot}([Na^+]_i, [K^+]_i, [Cl^-]_i) = \beta_X J_{cot}^0 \left[\ln \left(\frac{[Na^+]_o}{[Na^+]_i} \right) + \ln \left(\frac{[K^+]_o}{[K^+]_i} \right) + 2 \ln \left(\frac{[Cl^-]_o}{[Cl^-]_i} \right) \right]. \quad (3.2)$$

There is a factor 2 for Cl^- because two chloride ions are imported during a cycle. β_X is again a stoichiometry factor for which $\beta_{Na} = 1$, $\beta_K = 1$, and $\beta_{Cl} = -2$. J_{cot}^0 is the activity of the cotransporter and is proportional to the measured increase in external osmolarity that occurs upon blocking. It is because of a lack of information on the Na,K,2Cl-cotransporter and to keep the model as simple as possible that this linear, one-parameter dependence on osmolarity is used (van Mil et al., 1997).

The passive ion fluxes of Na^+ , K^+ and, Cl^- through membrane channels depend on electro-

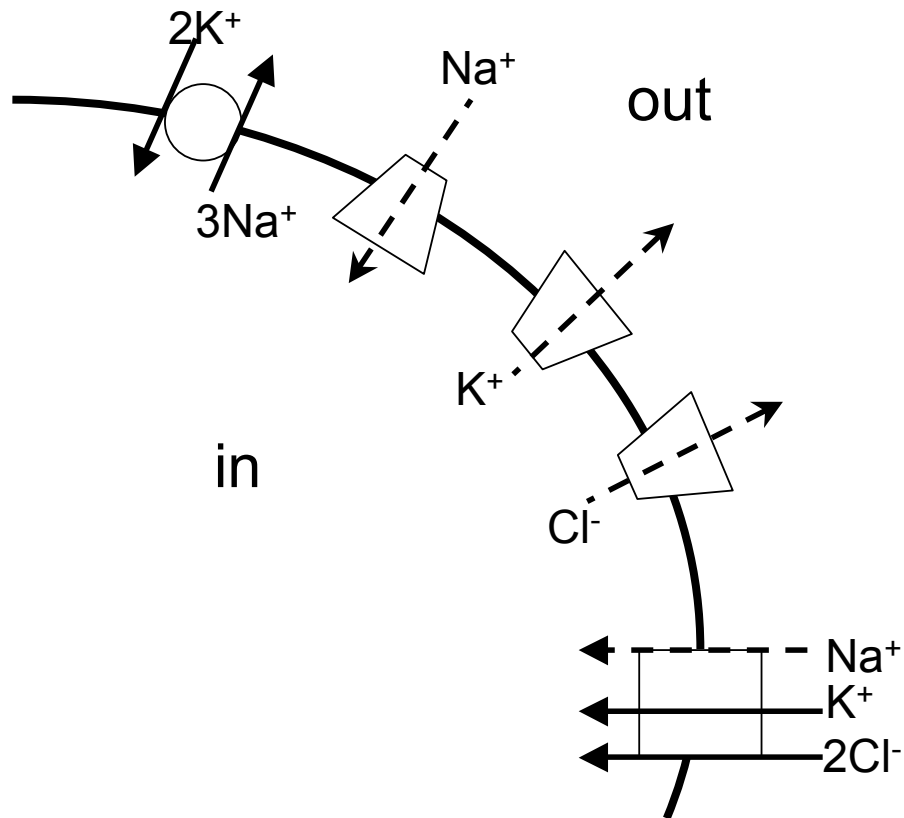


Figure 3.1: Overview of the components that make up the model. Solid arrows indicate transport against the electrochemical potential. Dashed arrows indicate transport that follows the electrochemical potential. On the top left is the Na,K-ATPase. This pump utilizes the free energy released by the hydrolysis of one ATP to import three sodium ions and export two potassium ions. The trapezoids denote ion channels that allow for passive ion flux. The arrows indicate the direction of such flux under physiological, steady state conditions. The rectangle at the right bottom represents the Na,K,2Cl-cotransporter. In the course of its cycle this symporter allows one sodium ion to move down the electrochemical gradient. A potassium ion and two chloride ions are carried along against their electrochemical gradients. Figure from Gallaher et al. (2009).

chemical gradients and permeabilities. The flux through the channels is given by the GHK current equation (cf. Eq. (2.3)):

$$J_X(U) = -P_X \frac{U ([X]_o - [X]_i e^U)}{1 - e^U} . \quad (3.3)$$

The notation for $[X]_i$ and $[X]_o$ as the concentrations of ion X inside and outside the cell, respectively, remains the same as in Eq. (2.3), where X stands for Na^+ , K^+ or Cl^- . The more convenient notation with the dedimensionalized electric transmembrane potential, U , is used here. Once again, $U = z_j F V_m / RT$, where V_m is the electric transmembrane potential and z_j is the charge value of the ion (+1 for Na^+ and K^+ , and -1 for Cl^-). At 35°C the factor F/RT is 38 V^{-1} . P_X stands for the permeability of the membrane to an ion X. J_X gives the resulting particle flow from the outside to the inside of the cell. There is no accounting for the characteristics of the short-timescale kinetics (i.e. time delayed activation and inactivation of P_{Na} and P_{K}), only steady states.

P_{Na} and P_{Cl} are assumed constant in the model, but P_{K} carries a dependence on V_m and $[\text{K}^+]_o$ because of the presence of IRKs. The following, empirically based, description will be used (Hagiwara and Takahashi, 1974; Standen and Stanfield, 1978; Siegenbeek van Heukelom, 1994; van Mil et al., 2003):

$$P_K(V_m, [\text{K}^+]_i, [\text{K}^+]_o) = P_0 + \frac{\bar{P}_K}{\sqrt{[\text{K}^+]_o}} \left(1 + \exp \left[\frac{V_m - V_h}{V_s} \right] \right)^{-1} . \quad (3.4)$$

P_0 is a constant that represents the permeability due to K^+ channels other than IRKs. The IRK channels are voltage gated and the term in parentheses establishes a Boltzmann distribution for the open/closed partition. V_s expresses how sensitive the open/closed distribution is to changes in V_m . V_h is the voltage at which the open/closed distribution is fifty-fifty (Hille, 1992). V_h appears to be close to E_K , the chemical potential of potassium (Standen and Stanfield, 1978). Thus $V_h = E_K + \Delta V_h$, where ΔV_h creates a small range in which the IRK is open even though $V_m > E_K$. As was mentioned before, upon decreasing $[\text{K}^+]_o$, the switch from the hyperpolarized to the depolarized state occurs when $(V_m - E_K)$ becomes too large. A larger ΔV_h will allow hyperpolarization to remain at lower values of $[\text{K}^+]_o$. From experiment it is apparent that the IRK channels can “sense” the electric membrane potential as well as the intracellular and extracellular

potassium concentrations. Equation (3.4) describes this sensing. The underlying mechanisms for the sensing are the focus of much research activity (Spassova and Lu, 1998; Guo and Lu, 2003; Lu, 2004; Yan et al., 2005).

For all of the involved ions the change per unit of time of the intracellular concentration, i.e. $d[X]_i/dt$, can be expressed as the sum of all the fluxes involving that ion multiplied by surface-to-volume ratio of the cell:

$$\frac{d[X]_i}{dt} = \frac{S}{B} (J_X + J_P + J_{cot}). \quad (3.5)$$

Here B represents cell volume and S represents cell surface area. The experiments involve long cylindrical muscle cells with a radius of about $20 \mu\text{m}$. This leads to $B/S = 10 \mu\text{m}$. This ratio is assumed to remain constant throughout the experiment since volume changes were not observed. Volume constancy implies that also osmolarity is invariable (i.e. $([\text{Na}^+]_i + [\text{K}^+]_i + [\text{Cl}^-]_i)$ remains constant) because an osmotic change would lead to the net movement of water and a concurrent volume change. In the reference by Fraser and Huang (2004) similar methods are used, but these authors allow for a variation of the B/S -ratio.

Going from particle fluxes to electrical currents requires charge consideration. A positive current occurs when a cation moves from the outside to the inside. So the change in the transmembrane potential due to the fluxes $d[X]_i/dt$ is:

$$\frac{dV_m}{dt} = \frac{F}{C_m} \frac{B}{S} \left(\frac{d[\text{Na}^+]_i}{dt} + \frac{d[\text{K}^+]_i}{dt} - \frac{d[\text{Cl}^-]_i}{dt} \right). \quad (3.6)$$

F is again Faraday's constant and C_m is the specific membrane capacitance where $C_m = 8.0 \times 10^{-6} \text{ F/cm}^2$. It is because of convolutions of the membrane and the presence of the T-tubular system in muscle cells that the value of the specific membrane capacitance is about 8 times larger than that of an ordinary lipid bilayer (Siegenbeek van Heukelom, 1994). Since the specific membrane capacitance does not vary much between cells, $q = FB/C_mS$ is assumed invariant. The constant q then effectively only depends on cell geometry. In the computations $q = 12183 \text{ V/M}$ (volts/molar concentration). Essentially, q is a conversion factor that gives the transmembrane voltage that results from the charge of a mole of monovalent ions in the cell. Equation (3.6) can be integrated with respect to time to express V_m in terms of $[\text{Na}^+]_i$, $[\text{K}^+]_i$, and $[\text{Cl}^-]_i$:

$$V_m = q ([Na^+]_i + [K^+]_i - [Cl^-]_i) + V_0 . \quad (3.7)$$

V_0 enters the equation as an integration constant. Physically, V_0 represents the contribution to the transmembrane potential of ions other than Na^+ , K^+ , and Cl^- . These include ions like Ca^{2+} , Mg^{2+} , and larger organic molecules (ATP, ADP, proteins, sugars, DNA, etc.), which are mostly negatively charged.

Steady state means that the time derivatives in Eq. (3.6) are zero. The resulting algebraic system connects the transmembrane electric potential to ion concentrations and membrane permeabilities. The expression for the potassium permeability (Eq. (3.4)) constitutes a serious analytical complication because P_K and V_m depend on each other. It can thus be understood that for the same $[K^+]_o$, a low- P_K depolarized state can coexist with a high- P_K hyperpolarized state (van Mil et al., 2003).

3.1.2 Methods

The experiments were performed on superficial cells of the lumbrical muscle of the mouse *in vitro*. Cells were impaled with fine tipped glass microelectrodes (filled with 3.0 M KCl and tip resistance $> 20 \text{ M}\Omega$) and remained in the cell for the entire duration of the experiment (Siegenbeek van Heukelom, 1991; van Mil et al., 1997, 2003; Geukes Foppen, 2004). First the cell was brought to a steady state with the physiological value $[K^+]_o = 5.7 \text{ mM}$ and then V_m was measured. The estimate for $[K^+]_o$ may be considered high, but that does not change the eventual results. Even the more recent lower estimates are well outside of the range where the bistability is found.

The ion concentrations in the extracellular medium were fully controllable. $[K^+]_o$ was decreased in small steps, and after each step, sufficient time was allowed for the measured V_m 's to reach a new steady state (van Mil et al., 1997). $[K^+]_o$ was decreased down to 0.76 mM followed by a stepwise increase back to 5.7 mM. The changes of $[K^+]_o$ were too slow to induce an action potential (which may drive a cell to another steady state). Generally, relaxation to a new steady state value of V_m after changing $[K^+]_o$ was a matter of minutes. When it was obvious that a switch to the other branch of solutions was occurring, the wait time was about a half an hour. More details on the materials and methods are presented in the references by Siegenbeek van Heukelom (1991), van Mil et al. (1997, 2003), Geukes Foppen et al. (2002), and Geukes Foppen (2004).

Next the same loop was performed on the same cell in an altered medium. One medium was altered with the addition of 75 μM bumetanide. The other medium was made hyperosmotic through the addition of the membrane impermeable polyethylene glycol 300. Running the two loops, the control loop and the subsequent loop with the altered medium, takes about four hours. Deterioration of the cell in such a period of time occurs, but is generally small. Each of the two kinds of two-loop experiments was done three times.

For the model calculations the following approach was taken. With the measured value of V_m and the extracellular concentrations at the beginning of each experiment, Eq. (3.5) can be used to obtain the intracellular concentrations by setting $d[\text{Na}^+]_i/dt = 0$, $d[\text{K}^+]_i/dt = 0$, and $d[\text{Cl}^-]_i/dt = 0$. Substituting the obtained values $[\text{Na}^+]_i$, $[\text{K}^+]_i$, and $[\text{Cl}^-]_i$ into Eq. (3.7) then leads to the value for V_0 . For a given cell, the value for V_0 so calculated at the physiological starting point was kept constant throughout the calculations. Independent estimates for the values of many of the involved parameters (J_P^{Max} , P_{Na} , K_m^K , K_m^{Na} , etc.) can be found in the literature and will be compared to the model results in the Discussion section.

To check the model against the experiments, the value $[\text{K}^+]_o$ is decreased from the aforementioned 5.7 mM and new values for $[\text{Na}^+]_i$, $[\text{K}^+]_i$, and $[\text{Cl}^-]_i$ are obtained when a steady state (i.e. $d[X_i]/dt = 0$ in Eq. (3.5)) emerges. Equation (3.7) then determines V_m . A simple Newton scheme often appeared to not converge to a steady state. It turns out that the ultimate V_m is orders of magnitude smaller than $q[\text{Na}^+]_i$, $q[\text{K}^+]_i$, $q[\text{Cl}^-]_i$, and V_0 themselves. $[\text{Na}^+]_i$, $[\text{K}^+]_i$, and $[\text{Cl}^-]_i$ are all of more than mM magnitude, but the ultimate V_m is brought about by a μM imbalance between positive and negative ions. This leads to complications in the computation of the steady state. Using *Mathematica*® (Wolfram Research, Inc., 2008) it was actually easier to simulate Eq. (3.5) as a system of differential equations. It could then be seen how $[\text{Na}^+]_i$, $[\text{K}^+]_i$, and $[\text{Cl}^-]_i$ converge in real time to new stable steady state values after every change of $[\text{K}^+]_o$ to simulate the real time relaxation observed in the experiments. The code for the simulation is provided in Appendix A.

3.1.3 Results

Experimental outcomes were found to be similar and Fig. 3.2 shows representative results. The triangles in the figure show the measured V_m 's as $[\text{K}^+]_o$ was decreased, and at some critical value of $[\text{K}^+]_o$, the cell switched to the depolarized state. On the way back to 5.7 mM, the steady state transmembrane potential is indicated with circles. In the course of increasing $[\text{K}^+]_o$ the

switch to the hyperpolarized state occurs at a significantly higher value for $[K^+]_o$ than the value at which, previously, the switch to the depolarized state occurred. The figures thus reveal an obvious hysteresis loop and a distinct region of bistability. For the control loop the bistable region was found to be between 1.57 mM (± 0.09 mM, $n=13$) and 2.77 mM (± 0.12 mM, $n=13$). For the loops with bumetanide in the medium the bistable region was found to be between 1.25 mM (± 0.16 mM, $n=3$) and 2.36 mM (± 0.16 mM, $n=3$). For the loops with a hyperosmotic medium the bistable region was found to be between 2.33 mM (± 0.31 mM, $n=2$) and 3.14 mM (± 0.29 mM, $n=2$). The bumetanide and hyperosmotic results can also be expressed as percentages of the control to exclude the variation between cells. With bumetanide the switches are at potassium concentrations that are $67 \pm 4\%$ and $83 \pm 8\%$ for the switch to the depolarized branch and the switch to the hyperpolarized branch, respectively. In the hyperosmotic situation these values are $181 \pm 9\%$ and $136 \pm 6\%$. Some of the results of these experiments are also found in the reference by Geukes Foppen et al. (2002).

The curves in Fig. 3.2 show the results of the model simulation. The parameters that produce the fits are compiled in Table 3.1. As was mentioned before, estimates for many of the relevant parameter values can be taken from the literature. A number of input parameters was specified before the calculations started. After determining V_0 , it was checked whether the concentrations $[Na^+]_i$, $[K^+]_i$, and $[Cl^-]_i$ were in the expected range (cf. Table 3.1). It was also necessary to check that the osmotic content ($[Na^+]_i + [K^+]_i + [Cl^-]_i$) was in an acceptable range and these values are also listed in Table 3.1. Volume changes were never observed in the course of the experiment. It seems reasonable then, that a cell can respond adequately to a hyperosmotic environment by increasing its own osmotic value.

In fitting the model curves to the experimental data, a few aspects become obvious and are worth pointing out. On the depolarized branch, when the IRK channels are closed, it is the ratio P_{Na}/P_0 that largely determines V_m . The value \bar{P}_K (cf. Eq. (3.4)) establishes the level of hyperpolarization when the IRKs are open. The two most important values for the variation of the bistable region are the parameters ΔV_h and V_s that underly the opening and closing of the IRK channels (cf. Eq. (3.4)). The sensitivity constant V_s is seen to determine the horizontal width of the bistable region in the V_m vs. $[K^+]_o$ graph. The parameter ΔV_h , which describes the deviation of V_h from E_K , is what determines where along the $[K^+]_o$ -axis the bistable region is centered.

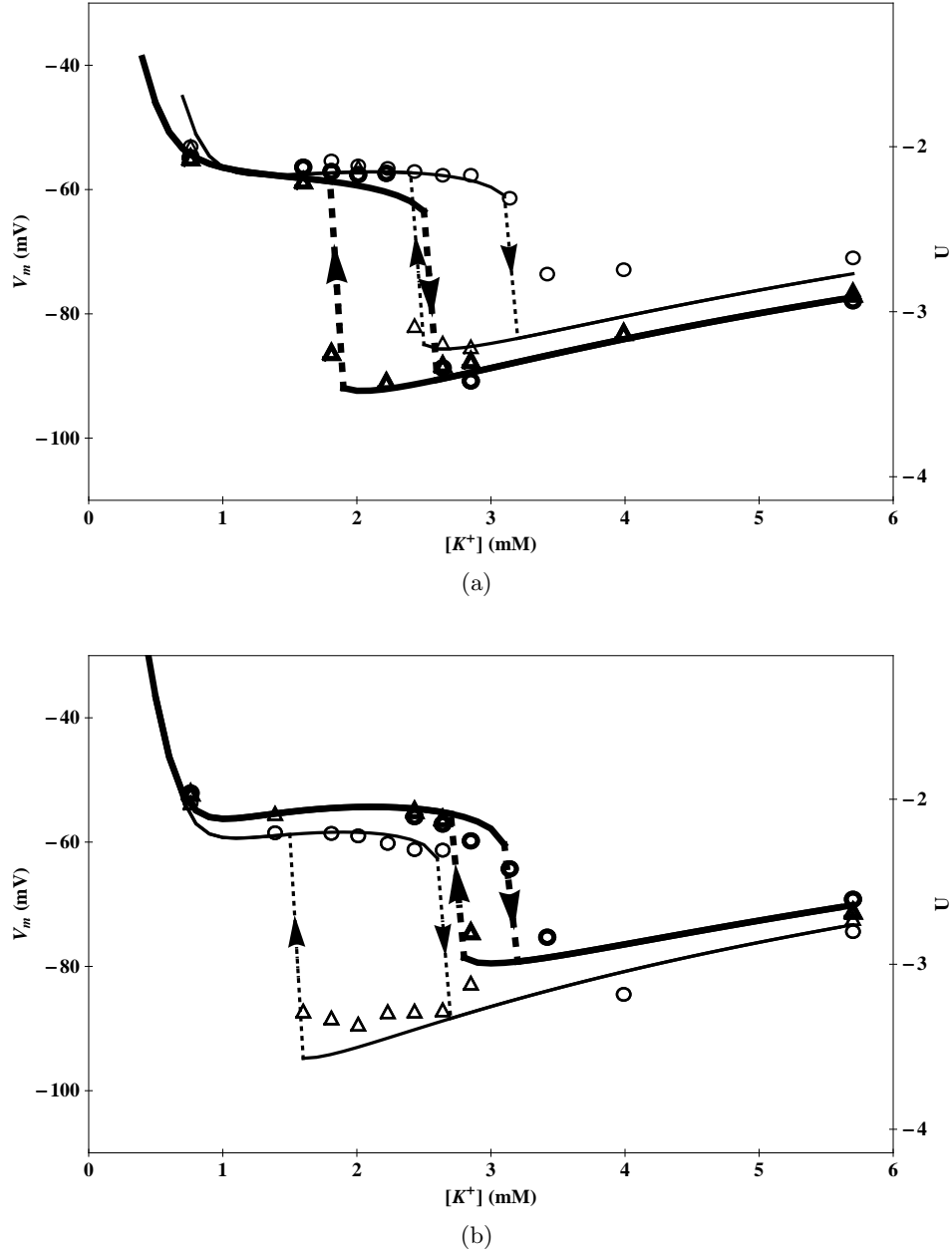


Figure 3.2: Comparison of experimental and theoretical data. Triangles indicate the transmembrane voltage as $[K^+]_o$ is decreased from 5.7 mM to 0.76 mM. Circles give the transmembrane voltage as $[K^+]_o$ is increased again. Experimental data also appeared in the reference by Geukes Foppen et al. (2002). The parameter values of these fits are given in Table 3.1. The curves indicate model fits. Figure from Gallaher et al. (2009). (a) Recorded hysteresis loops of one and the same cell with 75 μ M bumetanide (thick symbols and curves) and without bumetanide (thin symbols and curves) in the medium. Bumetanide removes Cl^- as an influence on the membrane potential and is here observed to shift the bistable region to lower values of $[K^+]_o$. (b) Recorded hysteresis loops of one and the same cell in a normal (289 mOsm/kg) medium (thin symbols and curves) and in a hyperosmotic (344 mOsm/kg) medium (thick symbols and curves). Hyperosmolarity increases the turnover rate of the Na,K,2Cl-cotransporter and thus drives the chloride electrochemical potential further away from zero. The figure shows how the augmented chloride contribution to the membrane potential drives the bistability to higher values of $[K^+]_o$.

	Parameter	Bumetanide		Hyperosmotic		Dimensions	Condition
		Control	Altered	Control	Altered		
Input Parameters	P_{Cl}	1.90E-05	1.90E-05	1.90E-05	1.90E-05	cm/s	Derived in Appendix A
	P_0	6.06E-07	6.06E-07	6.08E-07	6.08E-07	cm/s	Adjusted to obtain the correct ratio P_{Cl}/P_K
	P_{Na}/P_0	0.08	0.154	0.075	0.08	-	Adjusted to fit depolarized V_m at low $[K^+]_o$
	\bar{P}_K/P_0	0.65	0.55	0.45	0.7	-	Adjusted with P_0 to fit hyperpolarized V_m
	V_m	-73.55	-77.35	-73.30	-70.15	mV	Taken as the average of the measured values
	V_s	8.9	7.5	8.0	10.5	mV	Determines the range of the hysteresis loop
	ΔV_h	11.8	19.3	18.8	10.7	mV	Determines switch-off in the depolarizing curve
	J_P^{Max}	5.50E-11	4.50E-11	5.50E-11	3.80E-11	mole/cm ² s	Determines the strength of the pump
	K_m^K	1.30	0.50	1.20	0.82	mM	Affects low $[K^+]_o$ behavior
	K_m^{Na}	7.00	7.00	6.00	6.00	mM	Partially determines $[Na^+]_i$
	Osm	0.296	0.296	0.296	0.344	Osm	Measured osmolality of external medium
	Osm ₀	0.268	0.268	0.268	0.268	Osm	Measured osmolality when flux of cotransporter is nil
	OsmSense	2.40E-09	0.00E+00	2.40E-09	1.40E-09	1/cm ² s	Determines the strength of the cotransporter
	J_{cot}^0	6.72E-11	0.00E+00	6.72E-11	1.06E-10	mole/cm ² s	Activity of the cotransporter: (Osm-Osm ₀)*OsmSense
	V_0	-1718.54	-1871.33	-1664.85	-1699.58	V	Integration constant for V_m
Output Parameters	P_{Cl}/P_K	5.66	4.53	5.82	6.29	-	Should be in the range 3 to 10
	P_K/P_{Na}	69.20	44.91	71.54	62.13	-	Should be in the range 50 to 100
	$[Na^+]_i$	12.68	17.04	10.11	14.94	mM	In control $[Na^+]_i$ should be approximately 14 mM
	$[K^+]_i$	136.84	143.61	135.08	134.26	mM	In control $[K^+]_i$ should be approximately 140 mM
	$[Cl^-]_i$	8.47	7.06	8.54	9.71	mM	In control $[Cl^-]_i$ should be approximately 8 mM
	$[Cl^-]_i, Eq$	8.15	7.06	8.22	9.26	mM	Equilibrium $[Cl^-]_i$ at V_m
	$[Cl^-]_i - [Cl^-]_{i, Eq}$	0.32	0.00	0.32	0.45	mM	Compares well with experimental values
	$[Na^+]_i + [K^+]_i + [Cl^-]_i$	158.0	167.7	153.7	158.9	mM	Total osmolality of permeable ions inside the cell
	J_{cot}/β_X	-8.99E-12	0.00E+00	-8.79E-12	-1.21E-11	mole/cm ² s	Gives an estimate to the rate of the cotransporter
	J_P/α_X	-9.75E-12	-1.35E-11	-9.28E-12	-1.05E-11	mole/cm ² s	Gives an estimate to the rate of the pump

Table 3.1: A list of parameter values to fit the experimental data depicted in Fig. 3.2. Input parameters were measured in experiment or taken from the literature. Output parameters were obtained by matching the model with experimental outcomes as shown in Fig. 3.2. The given values are for $[K^+]_o = 5.7$ mM. How P_{Cl} is initially estimated is shown in Appendix B. The curves in Fig. 3.2 can be shifted by changing permeability ratios and other parameters. P_0 was adjusted to get a P_{Cl}/P_K in between 3 and 10 (Bretag, 1987). On the depolarized branch, when IRKs are closed, P_{Na}/P_0 determines V_m and was appropriately set. \bar{P}_K/P_0 was likewise set in agreement with the hyperpolarized V_m . The value for \bar{P}_K leads to $\bar{P}_K/(P_0\sqrt{[K^+]_o}) \approx 10$ at physiological conditions. V_m is the average of before and after the entire experiment of Fig. 3.2. The parameter J_{cot}^0 is found to depend on the osmolality (“Osm”) of the medium. Following the reference by van Mil et al. (1997), a linear dependence $J_{cot}^0 = \text{OsmSense}(\text{Osm} - \text{Osm}_0)$ is assumed, where “OsmSense” fixes the sensitivity of J_{cot}^0 to osmolality and “Osm₀” is the osmolality at which the cotransporter comes to a standstill. The obtained values for the intracellular concentrations are very reasonable. Table modified from Gallaher et al. (2009).

It is the Na^+ potential that drives the Na,K,2Cl-cotransporter. So, ultimately, the cotransporter's energy supply derives from the ATP driven Na,K-pump. The cotransporter's Cl^- -transport against the net electrochemical Cl^- -potential, therefore, indirectly presents another load on the Na,K-pump. It can then be understood that, with more chloride transport, the system will make an earlier switch to the depolarized branch when $[\text{K}^+]_o$ is decreased. Thus the switch occurs at higher $[\text{K}^+]_o$ when the cotransporter is stimulated with a hyperosmotic medium. The presence of bumetanide, on the other hand, eliminates chloride traffic and should push the bistable region to smaller values of $[\text{K}^+]_o$. Experiments affirm these expectations and the model gives a good accounting (cf. Fig.'s 3.2(a) and 3.2(b)).

The GHK voltage equation is commonly used in electrophysiology and a discussion of this equation is included in many authoritative textbooks (Hille, 1992; Läuger, 1991; Keener and Sneyd, 1998). This equation expresses the membrane potential in terms of membrane permeabilities and ion concentrations.

$$V_m = \frac{RT}{F} \ln \left[\frac{P_K[\text{K}^+]_o + P_{\text{Na}}[\text{Na}^+]_o + P_{\text{Cl}}[\text{Cl}^-]_i}{P_K[\text{K}^+]_i + P_{\text{Na}}[\text{Na}^+]_i + P_{\text{Cl}}[\text{Cl}^-]_o} \right]. \quad (3.8)$$

This equation relies on the assumption that the net flow of charge through the channels is zero, however, that assumption does not apply in this model. The Na,K-ATPase is electrogenic, i.e., it generates a net electric current. The cotransporter is electroneutral, so in this model the net flow through the channels should carry a current equal and opposite to the Na,K-ATPase current. There is no “quick fix” of the GHK equation to take care of this effect (Fraser and Huang, 2004). Nevertheless, the GHK equation can ultimately be utilized to obtain an order of magnitude estimate to compare to the model results.

In Fig. 3.2(a) a further hyperpolarization of about 3 mV is observed on the hyperpolarized branch with the addition of bumetanide to the medium. Addition of bumetanide makes the condition that $E_{\text{Cl}} = V_m$ and chloride does not contribute to the setting of membrane potential. The GHK equation becomes:

$$V_m = \frac{RT}{F} \ln \left[\frac{P_K[\text{K}^+]_o + P_{\text{Na}}[\text{Na}^+]_o}{P_K[\text{K}^+]_i + P_{\text{Na}}[\text{Na}^+]_i} \right]. \quad (3.9)$$

At the close-to-physiological starting point, i.e. $[\text{K}^+]_o = 5.7$ mM, $[\text{Na}^+]_o = 148$ mM, and

$[\text{Cl}^-]_o = 130 \text{ mM}$, the measured V_m 's before and after the addition of bumetanide were -73 mV and -76 mV , respectively. Taking $[\text{K}^+]_i = 132 \text{ mM}$, $[\text{Na}^+]_i = 10 \text{ mM}$ in Eq. 3.9 leads to an estimate of $P_K/P_{\text{Na}} = 87$. Using this ratio in Eq. 3.8 and the lower bound of $P_{\text{Cl}} = 3P_K$ (Bretag, 1987; Aickin et al., 1989; Aickin, 1990) it is found with these equations that $[\text{Cl}^-]_i$ exceeds $[\text{Cl}^-]_{i,\text{Eq}}$ (which is to be calculated from $V_m = (RT/F) \ln \left([\text{Cl}^-]_{i,\text{Eq}} / [\text{Cl}^-]_o \right)$ at $V_m = -73 \text{ mV}$) by about 0.30 mM . This upper bound estimate, however, assumes that $[\text{Na}^+]_i$ and $[\text{K}^+]_i$ do not change upon the addition of bumetanide and it is bound to be inaccurate. It is inaccurate because the Na,K-ATPase and the Na,K,2Cl-cotransporter couple the flows of the involved ions. This model does take into account changes in $[\text{Na}^+]_i$ and $[\text{K}^+]_i$ after the addition of bumetanide and leads to an estimate of 0.32 mM for the accumulation of chloride above the equilibrium concentration. For the hyperosmotic medium the GHK equations, (3.8) and (3.9), lead to $([\text{Cl}^-]_i - [\text{Cl}^-]_{i,\text{Eq}}) = 1.6 \text{ mM}$, whereas this model predicts 0.45 mM .

3.1.4 Discussion

As was mentioned before, the Na,K,2Cl-cotransporter accumulates chloride in the cell to slightly above the concentration that would occur if the intracellular and extracellular chloride were at electrochemical equilibrium. It is obvious that there is a connection between this accumulation and the quantities J_{cot} for the cotransporter driven inflow and P_{Cl} for the chloride permeability of the membrane. A larger P_{Cl} leads to "easier" outflow and, thereby, to a smaller necessary accumulation to compensate for the inflow. Estimates of the involved quantities and parameters have varied. Direct measurement in mammalian skeletal muscle of the chloride accumulation with chloride sensitive electrodes led to $1.4 (\pm 1.2) \text{ mM}$ (Aickin et al., 1989). With similar methods, others have found values at the low end of this order of magnitude estimate (Donaldson and Leader, 1984; McCaig and Leader, 1984). It is apparent that the chloride accumulation above the electrochemical equilibrium concentration is too small to be meaningfully established with chloride sensitive electrodes. To obtain that accumulation two measured quantities that are almost equal have to be subtracted and the resulting difference comes with a relative error that is much larger than the relative error of the original measured quantities.

The method used to arrive at estimates for J_{cot} and J_{Cl} is described in Appendix B. Barium (Ba^{2+}) blocks the IRKs and upon its application the membrane potential relaxes to a new steady state. In the reference by Geukes Foppen (2004) such relaxation was employed to come to an

estimate of J_{cot} . This relaxation, which takes about one to four minutes, was recorded with and without bumetanide in the medium and fitted with a single exponential. J_{cot} was thus found to be $13.4 \times 10^{-12} \text{ mol cm}^{-2} \text{ s}^{-1}$ which is in the range of the values found here. However, the starting point for the J_{cot} -estimate of the reference by Geukes Foppen (2004) was the aforementioned approximate 1.4 mM chloride accumulation measured by Aickin et al. (1989). The reference by Geukes Foppen (2004), furthermore, used the formula $V_m = (RT/F) \ln ([\text{Cl}^-]_i / [\text{Cl}^-]_o)$ to relate a change in transmembrane voltage after the addition of bumetanide to a change in $[\text{Cl}^-]_i$. Such a correspondence between cotransporter-caused chloride accumulation and membrane potential can, at best, be very approximate, as the Na,K,2Cl-cotransporter also moves sodium and potassium across the membrane. Moreover, the intracellular concentrations of the three involved ions are all coupled to each other and to the membrane potential. The full effect of the addition of bumetanide can only be assessed through a numerical simulation in which these couplings are incorporated.

There was no systematic general and exhaustive search over the entire parameter space to find what values lead to the best fit. There are too many parameters for such an approach to lead to a unique result. Moreover, such an approach would not be sensible as the model is approximate to begin with. Initial conditions were imposed that were close to existing estimates and those values were kept within an acceptable range as the curves were fit. The goal was to merely reproduce the experimental phenomena (the bistability foremost) in a simulation with known facts, estimates, and relationships.

The Na,K-ATPase has been well researched and the parameter values reported in Table 3.1 are in the established range. K_m^K and K_m^{Na} are used as described in Eq. (3.1). Customarily, the K_m^X is defined as the concentration at which the pump operates at half the speed of what it would be at saturating $[X]$. Because of the powers -2 and -3 in the description of the Na,K-ATPase (cf. Eq. (3.1)), there will be 1/8 of the saturated turnover at $[\text{Na}^+]_i = K_m^{\text{Na}}$ and 1/4 of the saturated turnover at $[\text{K}^+]_o = K_m^K$. The authoritative textbook by Läuger (Läuger, 1991) gives $K_m^{\text{Na}} = 0.6 \text{ mM}$ and $K_m^K = 0.2 \text{ mM}$ for the values at which the pump operates at the half maximal rate. However, estimates for these parameters have varied widely. More recently Sejersted and Sjøgaard (2000) reports $K_m^K = 0.8 - 1.5 \text{ mM}$ and $K_m^{\text{Na}} \sim 15 \text{ mM}$. These numbers appear closer to the estimates found here.

J_P^{Max} is not just a molecular property. J_P^{Max} is also proportional to the number of pumps per

unit area on the cell membrane. J_P^{Max} can thus vary widely from cell to cell. Sejersted (1988) lists the estimated maximal transmembrane flux of sodium ions for three different mammalian muscle cells. These estimates vary from 25 to 83 pmol s⁻¹cm⁻². The associated J_P^{Max} is found after dividing these numbers by three. The numbers in Table 3.1 appear about an order of magnitude higher than these estimates. Likewise, P_{Na} depends linearly on the permeability of a channel as well as on the number of channels per unit area of cell membrane. The values in Table 3.1 appear close to the $P_{Na} = 5.37 (\pm 0.30) \times 10^{-8}$ cm s⁻¹ that is reported in the reference by Costa et al. (1989) for *Xenopus laevis* oocytes.

The change of the width and location of the bistable region in Fig.'s 3.2(a) and 3.2(b) is accounted for primarily with changes in the IRK parameters V_s and ΔV_h . The parameter V_s quantifies the sensitivity of the IRK's open-closed ratio to the membrane potential. Over the course of more than three decades the inward rectification has been fitted many times to a Boltzmann distribution. Estimates for V_s have consistently fallen in the range between 7 mV and 15 mV (Wessel et al., 1999). It may seem odd for V_s and ΔV_h to depend on ion concentrations as opposed to parameters of the internal structure of the IRK channel. However, it has been reported that other ions (like Mg²⁺) are involved in the closing of the IRKs and that concentration levels of intracellular polyamines can modulate properties of the IRK channel (Lu, 2004; Yan and Ishihara, 2005). It is possible that Mg²⁺ and polyamine concentrations are behind the variation in V_s and ΔV_h that is seen in Table 3.1. The variation of V_s is within the aforementioned 7 to 15 mV range. No estimates for ΔV_h were found in the literature.

It has been suggested that chloride permeability can increase with osmotic stress (Yamamoto et al., 2004). But this model assumes P_{Cl} is constant and P_K is adjusted such that the ratio P_{Cl}/P_K is between 3 and 10 (Bretag, 1987). The potassium permeability is about seventy times as large as the sodium permeability. It can be inferred from the values of \bar{P}_K and P_0 that the IRKs account for about 85% of the potassium permeability at physiological conditions.

Near physiological conditions it is the small P_{Na} that determines V_m . The membrane potential, after all, has to be brought to a level that is sufficiently negative to get the passive inward flow that steady state requires. P_K and P_{Cl} are very high and, at any electric membrane potential, E_K and E_{Cl} will be close to V_m . The cotransporter flow is driven by the sodium electrochemical potential and, for its effect on the membrane potential, the cotransporter acts as an addition to the sodium

permeability. So, blocking the cotransporter works out electrochemically like decreasing the P_{Na} . Such blocking therefore leads to a hyperpolarization. Stimulation of the Na,K,2Cl-cotransporter with hyperosmolarity leads, in turn, to a small depolarization.

Table 3.1 shows how the cotransporter actually cycles about as much as the Na,K-ATPase. From the numbers in the table it can be inferred that the inward sodium flow through the cotransporter amounts to roughly 30% of the magnitude of the outward sodium flow through the Na,K-ATPase. For potassium, cotransporter flow is about 50% of the flow through the Na,K-ATPase. At steady state it thus appears to not be legitimate to treat cotransporter activity as a mere perturbation on the dynamics of a system with only Na,K-ATPase and channels for sodium and potassium. The Na,K,2Cl-cotransporter is a carrier. As such, it ought to exhibit Michaelis-Menten type saturation with increasing concentrations of the carried ions. Lack of available data on the cotransporter led to the simple one-parameter description of the cotransporter's turnover rate. Neglecting the saturation may be particularly inappropriate in the hyperosmotic situation (Geukes Foppen et al., 2002). A more accurate model can be constructed as more data on the cotransporter will become available.

3.2 The Role of Inward-rectifying Potassium Channels

Inward rectifying potassium channels (IRKs) appear to be essential for the bistable behavior found in the previous section. When the electrochemical potential for potassium is such that too much potassium is driven outward, the IRKs close. This characteristic results in a kind of “protection” of the high intracellular potassium concentration and this is often thought to be the reason that IRK properties first evolved about 2.4 billion years ago (Hille, 1992). The dynamics of the systems of pumps and channels is such that the closing of a small fraction of IRK channels leads to the closing of more IRK channels (Goodman and Art, 1996; Lu, 2004). Because of this positive feedback mechanism there are no continuous transitions between the hyperpolarized and the depolarized state. Instead it is found, theoretically and experimentally, that there is a genuine non-equilibrium first order phase transition (Moore, 1972). It is furthermore found that, in a certain value range of the extracellular potassium concentration, both the hyperpolarized state and the depolarized state are stable and hysteretic behavior occurs (Jackson, 1989).

The hypophysiological concentration of extracellular potassium leads to a larger outbound force on intracellular potassium. A hyperpolarization can compensate for this increased chemical force.

However, such hyperpolarization implies a larger leak of sodium ions and a concurrent increased demand on the Na,K-ATPase pumps. At some point, the hyperpolarization may simply become too metabolically costly to maintain. In the depolarized state the potassium channels are largely closed and the sodium leak is decreased. By blocking ion flow and ceasing the metabolic efforts that maintaining such flow requires, the cell effectively isolates itself from the adverse environment and “goes into hibernation.” Upon again increasing the extracellular potassium concentration a switch back to the hyperpolarized state is observed. However, as was seen in the previous section, that switch back to the hyperpolarized branch occurs at a extracellular potassium concentration that is about half a millimolar higher than the concentration at which the switch to the depolarized branch occurs. So, only when the environment is well within the “healthy” domain again does the cell “wake up” again. It is likely that the bistability evolved as a functional response to environmental adversity.

Below the results of experiments will be presented in which the potassium permeability, P_K , of the cell membrane is increased dramatically. This is accomplished by adding isoprenaline to the medium. The dependence on concentration and electric potential of the IRKs open-closed behavior will be overwhelmed and become negligible in this case. With this fixed, constant and high P_K the phase transition and the bistability no longer occur. It is furthermore found that for the case of high constant P_K an analytic solution can be found for the steady state equations for the sodium and potassium flow. Theory and experiment appear in very good agreement. The isoprenaline case is also compared with the control in which the P_K is dominated by IRKs.

The only way to handle the system of equations encountered in the previous section with so many free parameters is through numerical methods. In that model, it was observed that chloride transport can affect the transmembrane potential. Despite this change, the basic hysteresis structure at low extracellular potassium conditions was preserved. To get a better grip on this system, the equations will be reduced analytically and chloride will be excluded.

3.2.1 The Model

Some of the symbols of the model from the previous section will be recycled here and some will change to keep the equations succinct. The model set up here uses the notation of Keener and Sneyd (Keener and Sneyd, 1998). The prominent ions, sodium and potassium, are pumped against the electrochemical potential by the ATP driven Na,K-ATPase in order to maintain a high

potassium concentration and a low sodium concentration inside the cell. At steady state there is, for each ion, an equal and opposite passive flow through ion channels. To model the flux of ions across the cell membrane, the following steady state equations are used:

$$P_{\text{Na}} U \frac{N_i - N_e e^{-U}}{1 - e^{-U}} = -3k_p \mu(K_e; K_m^K) \mu(N_i; K_m^N) \quad (3.10)$$

$$P_K U \frac{K_i - K_e e^{-U}}{1 - e^{-U}} = 2k_p \mu(K_e; K_m^K) \mu(N_i; K_m^N) . \quad (3.11)$$

For both sodium (Eq. (3.10)) and potassium (Eq. (3.11)) these equations describe how the leak (on the left hand sides) must equal the active transport (on the right hand sides). The sodium and potassium membrane permeabilities, P_{Na} and P_K are multiplied with the electrochemical potentials for the respective ions to obtain the leak rate, which is identical to Eq. (3.3). N_i and K_i represent the intracellular sodium and potassium concentrations. N_e and K_e represent the extracellular concentrations of sodium and potassium. The leak described on the left hand side of (3.10) and (3.11) is compensated for by the activity of the Na,K-ATPase, the sodium-potassium pump. For every cycle the Na,K-ATPase brings three sodium ions from the inside to the outside and two potassium ions from the outside to the inside. In Eq. (3.1) the powers 2 and 3 come about when it is assumed that each ion binds with the same probability. The pump activity is now described with *rate-limiting* Michaelis-Menten kinetics that comes about with the assumption that the last ion to bind limits the whole reaction rate. Here k_p is the maximal turnover rate for the pump and $\mu(x; K_m^x) = x/(K_m^x + x)$. The textbook by Lauger gives $K_m^K = 0.2$ mM and $K_m^N = 0.6$ mM (Lauger, 1991). The 0.2 mM represents the extracellular potassium concentration that, with saturating intracellular sodium concentration, leads to a half-maximal turnover rate for the pump. Likewise, 0.6 mM represents the intracellular sodium concentration that, with a saturating extracellular potassium concentration, leads to a half-maximal turnover rate for the pump.

As mentioned previously, the potential difference U comes about as a consequence of submicromolar differences in concentration between cations and anions. In this model sodium and potassium are the only permeable ions. The concentrations of sodium and potassium are all millimolar or higher. Therefore an electroneutrality condition is imposed: $N_i - N_e = -(K_i - K_e) = \delta C$, where the variable δC denotes the chemical imbalance between the cell and the medium in which it is

immersed. The electroneutrality condition also imposes an osmotic balance:

$$N_i + K_i = N_e + K_e = C \quad (3.12)$$

requiring that the total concentration, C , of permeable solutes is equal in the extracellular and the intracellular solution.

Now there are three equations (Eqs. 3.10-3.12) with three unknowns (N_i , K_i , and U). By separating out the quotients on the left hand side and adding up Eqs. (3.10) and (3.11) a single expression for U is found in which the exponentials have canceled:

$$U = - \left(\frac{3k_p}{N_e + K_e} \right) \left(\frac{P_K - \frac{2}{3}P_{Na}}{P_K P_{Na}} \right) \left(\frac{K_e}{K_m^K + K_e} \right) \left(\frac{N_i}{K_m^N + N_i} \right). \quad (3.13)$$

This may look straightforward until the nature of P_K is considered. For the IRK channels, P_K depends on the electrochemical potential of potassium, i.e., on K_e , K_i , and U (cf. Eq. (3.4)). To better understand the system it will be explored both theoretically and experimentally what happens when P_K is constant and much larger than P_{Na} . This can be accomplished by adding isoprenaline to the medium.

3.2.2 Isoprenaline Eliminates Bistability

Isoprenaline is a slowly hydrolyzable beta adrenergic agonist. Pharmacologically it has been utilized to increase the heart rate and relax the airways to increase air flow. Isoprenaline closes IRKs (Geukes Foppen et al., 2002), but the characteristic of isoprenaline that is important in this situation is the ability to open Ca^{2+} -gated potassium channels (Kume et al., 1989). The number of such channels in the muscle cells used in the experiment is very large (Sejersted and Sjøgaard, 2000; Kristensen et al., 2006). The permeability associated with the Ca^{2+} -gated potassium channels far overwhelms the permeability due to IRKs. Such opening results in a P_K that is large and independent of K_e , K_i , and U .

In the experiments the transmembrane potential of superficial cells of the lumbrical muscle of the mouse were measured *in vitro* according to the same guidelines that were outlined previously (cf. section 3.1.2). Ion concentrations in the extracellular medium were controlled and the temperature was maintained at 35°C. The external medium was kept constant, i.e. $N_e + K_e = C$. After performing the loop with the control medium, 1 μ M isoprenaline was added to the medium of the

same cell. The same loop was then performed on the cell with the altered medium. Figures 3.3 and 3.4 show results with and without isoprenaline added to the external bath, respectively. The closed circles in Fig.'s 3.3 and 3.4 show the measured U 's of the cells as K_e was decreased in small steps. The open circles represent the voltages U as K_e is increased again.

Adding isoprenaline to the external solution results in a situation with $P_{\text{Na}} \ll P_{\text{K}}$ by between one and two orders of magnitude. Using this and the $N_e + K_e = C$ condition, Eq. (3.13) becomes:

$$U = -\frac{3k_p}{P_{\text{Na}}C} \left(\frac{K_e}{K_m^K + K_e} \right) \left(\frac{N_i}{K_m^N + N_i} \right). \quad (3.14)$$

The right hand sides of Eqs. (3.10) and (3.11) are of the same order of magnitude, but on the respective left hand sides P_{K} is about two orders of magnitude larger than P_{Na} . It is for this reason that the electrochemical potential for sodium (with $N_i - N_e \exp[-U]$ in the numerator) is two orders of magnitude larger than the one for potassium (with $K_i - K_e \exp[-U]$ in the numerator). Taking $K_i = K_e \exp[-U]$, gives $N_i = C - K_e \exp[-U]$ via the osmotic balance condition. Substituting this in (3.14) and after some algebraic rearrangement it is found that

$$U = -\frac{3k_p}{P_{\text{Na}}C} \left(\frac{K_e}{K_m^K + K_e} \right) \left(1 + \frac{K_m^N}{C - K_e e^{-U}} \right)^{-1}. \quad (3.15)$$

This is a relation between K_e , U , and a number of constant parameters. With a further approximation it is possible to obtain an explicit and simple expression for U as a function of K_e . In the regime where K_e is larger than about 2 mM, $K_e/(K_m^K + K_e)$ is taken to be one. This gives the relation

$$U = U_{\text{max}} \left(1 + \frac{K_m^N}{C - K_e e^{-U}} \right)^{-1}, \quad (3.16)$$

where $U_{\text{max}} = -3k_p/(P_{\text{Na}}C)$. Solving for K_e gives

$$K_e = e^U \left(C + K_m^N \frac{U}{U - U_{\text{max}}} \right). \quad (3.17)$$

C is larger than K_m^N by a factor of about 250. So $U = \ln[K_e/C]$ is a good approximation until U comes very close to U_{max} .

In a U vs. K_e graph U decreases (following $U = \ln[K_e/C]$) as K_e decreases. But as K_e

approaches 2 mM and U approaches U_{max} , a horizontal asymptote at $U = U_{max}$ is approached from above. Thus when K_e gets very low this approximation will not hold. However, at low K_e the sodium flux increases and therefore so does N_i . Going back to Eq. (3.14) and taking N_i much greater than K_m^N means that the last term goes to unity. These two approximations together give a concise expression for $U(K_e)$:

$$U(K_e) = \begin{cases} \ln\left(\frac{K_e}{C}\right) \frac{K_e}{K_m^K + K_e}, & \text{if } K_e > K_e^* \\ U_{max} \frac{K_e}{K_m^K + K_e}, & \text{if } K_e < K_e^* . \end{cases} \quad (3.18)$$

The condition $U_{max} = \ln[K_e^*/C]$ is utilized in order to connect the two parts of this curve at $K_e = K_e^*$. Figure 3.3 shows the data points deriving from the experiment together with a fit obtained with $K_m^K = 0.2$ mM and $K_e^* = 2$ mM. The latter value leads to $U_{max} = -4.3$, which, in terms of volts, corresponds to -110 mV. In the experiments $N_e + K_e = C$ was kept at 150 mM and this value was used in Eq. (3.18) to obtain the fit.

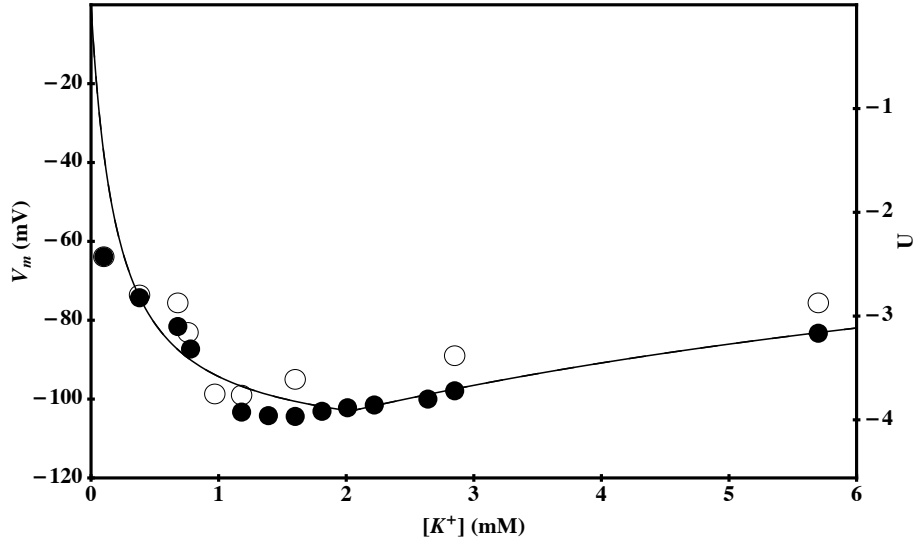


Figure 3.3: Results of isoprenaline experiment and theoretical curve. The dots represent experimental data taken at $N_e + K_e = 0.15$ M with 1 μ M isoprenaline in the medium. The filled dots represent the voltage after relaxation as K_e is decreased in a stepwise fashion. The open circles represent the voltages as K_e is increased again. The theoretical curve is according to Eq. (3.18) with $K_m^K = 0.2$ mM, $3k_p/P_{Na} = 0.65$ M. Figure from Gallaher et al. (Preprint A).

When $U_{max} = -4.3$ is related back to the expression $U_{max} = -3k_p/(P_{Na}C)$ with the value of 150 mM for C an estimate of $3k_p/P_{Na} = 0.65$ M is obtained. This is in good agreement with some

independent estimates of k_p and P_{Na} . The reference by Sejersted (1988) gives an estimate of 50 pmol $\text{s}^{-1}\text{cm}^{-2}$ for the steady-state, transmembrane flux of sodium ions of a muscle cell in physiological conditions. This value is used for $3k_p$. Molar (M) is mole per liter, i.e. mole per cubic decimeter. For consistency, decimeter (dm) will be used as the unit of distance. This gives $3k_p = 5 \times 10^{-9}$ mole $\text{s}^{-1}\text{dm}^{-2}$. The reference by Costa et al. (1989) reports $P_{\text{Na}} = 5.4 \times 10^{-9}$ dm/s for *Xenopus laevis* oocytes. Combination of the data of Sejersted and Costa et al. gives 0.9 M for $3k_p/P_{\text{Na}}$. This is reasonably close to the estimate obtained earlier of 0.65 M. Figure 3.3, moreover, shows a very good agreement between Eq. (3.18) and the experimentally recorded membrane potentials.

3.2.3 IRKs Produce Bistability

The IRK channel has an open probability that depends on the transmembrane potential as well as on intracellular and extracellular potassium concentrations (Hagiwara and Takahashi, 1974; Siegenbeek van Heukelom, 1994; Lu, 2004). The dependence appears to be well approximated by just the net electrochemical potential of potassium, i.e. $U - \ln(K_e/K_i)$ (Lu, 2004). It was, furthermore, observed already decades ago by Katz that current through the IRK decreased when K_e was decreased (Katz, 1949). It is not difficult to understand how the membrane potential can affect the open probability. A membrane potential of about 100 mV leads to a huge electric field inside the membrane (which is only about 5 nm thick). As that field changes, charged groups in or near the lining of the channel can reposition and thus modulate a channel's conductivity. How actual ion concentrations can affect a channel's conductivity is still a subject of active research (Guo and Lu, 2003; Yan et al., 2005). The potassium permeability is approximated with a slightly modified version of the previously encountered Eq. (3.4):

$$P_K = P_0 + P_{\text{IRK}}^{\text{max}} \left\{ 1 + \exp \left[\frac{1}{\varepsilon} \left(U - \ln \left(\frac{K_e}{K_i} \right) - \tilde{U} \right) \right] \right\}^{-1}. \quad (3.19)$$

P_0 , as before, represents the part of the potassium permeability that does not involve the IRKs and now $P_{\text{IRK}}^{\text{max}}$ is the maximum permeability of IRKs only. The factor $K_e^{-1/2}$ from Eq. (3.4) for the IRKs has been eliminated and does not appear to be essential. The inverse of the term in curly brackets is a Boltzmann distribution for the open fraction of the IRKs. The fraction of channels that is open depends on the net electrochemical potential of potassium ($U - \ln(K_e/K_i)$) and the parameters \tilde{U} and ε , which correspond to dedimensionalized forms of ΔV_h and V_s from Eq. (3.4),

respectively. For $U - \ln(K_e/K_i) = \tilde{U}$ the open-closed distribution is fifty-fifty. The small positive value of \tilde{U} guarantees that the IRKs are mostly open when the net electrochemical potential of potassium is about zero.

The P_K vs. U curve has a sigmoidal shape. For $U - \ln(K_e/K_i) \ll \tilde{U}$, the asymptotic value is $P_K = P_0 + P_{\text{IRK}}^{\text{max}}$ and the potential is hyperpolarized. For $U - \ln(K_e/K_i) \gg \tilde{U}$, the asymptotic value is $P_K = P_0$ and the potential is depolarized. The parameter ε gives the sensitivity of the open-closed distribution to the modified electrochemical potential $U - \ln(K_e/K_i) - \tilde{U}$. A small value of ε leads to a steep and sharp transition between the hyperpolarized and depolarized limits.

The region of interest is where K_e is taken to below the physiological value of about 5.7 mM. With isoprenaline in the external medium it was found that for $K_e > K_e^*$ the potential follows $U \approx \ln(K_e/C)$. That approximation corresponds to the branch described on the first line of Eq. (3.18) where $P_K \gg P_{\text{Na}}$. It is obvious from Eq. (3.18) that when crossing over into the regime where $K_e < K_e^*$, the transmembrane electric potential for potassium and the chemical potential for potassium are no longer balancing each other out and $U(K_e) > \ln(K_e/C)$. A situation with most of the IRKs being open can then no longer be maintained. With P_0 for P_K , we have a P_K that is of the same order of magnitude as P_{Na} . In that case Eq. (3.14) is no longer a valid approximation so Eq. (3.13) is reintroduced. With P_0 and P_{Na} of the same order of magnitude, the factor $(P_K - \frac{2}{3}P_{\text{Na}})$ will significantly differ from P_K . However, with a small K_e , the approximation $N_i \gg K_m^N$ can again be made. These conditions lead to a new expression for small K_e that incorporates the bistability. All in all, this gives for the two branches:

$$U(K_e) = \begin{cases} \ln\left(\frac{K_e}{C}\right) \frac{K_e}{K_m^K + K_e}, & \text{if } K_e > K_e^* \\ U_{\text{max}} \left(1 - \frac{2}{3} \frac{P_{\text{Na}}}{P_K}\right) \frac{K_e}{K_m^K + K_e}, & \text{if } K_e < K_e^* \end{cases} \quad (3.20)$$

In order to connect the two parts of the curve it is assumed that the bistable region is within the low K_e regime so that $\ln(K_e^*/C) = U_{\text{max}}(1 - \frac{2}{3} \frac{P_{\text{Na}}}{P_0 + P_{\text{IRK}}^{\text{max}}})$. The K_e^* is higher in the control (Eq. (3.20)) than in the isoprenaline case (Eq. (3.18)) because the term $(1 - \frac{2}{3} \frac{P_{\text{Na}}}{P_0 + P_{\text{IRK}}^{\text{max}}})$ drops slightly below unity. Figure 3.4 shows the results of experiments together with curves derived from the modeling.

With the IRKs, the closing of a small fraction of channels can lead to a snowball effect that

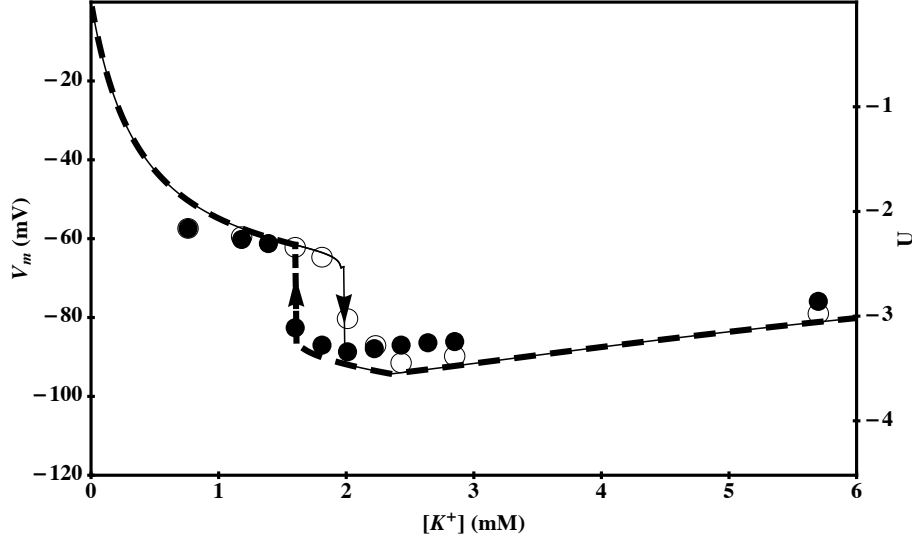


Figure 3.4: Comparison of experiment when IRKs are active with theoretical curve. The dots represent experimental data for the control situation taken at $N_e + K_e = 0.15$ M. The filled dots represent the voltage after relaxation as K_e is decreased in a stepwise fashion. The open circles represent the voltages as K_e is increased again. The theoretical curve is found by solving for U by Eq. (3.20) numerically stepwise using a Newton scheme at each K_e . It is thick and dashed for decreasing K_e and thin and continuous for increasing K_e . The parameters used were $P_{Na} = 5.4 \times 10^{-9}$ dm/s, $P_0 = 1.1 \times 10^{-8}$ dm/s, $P_{IRK}^{max} = 9.6 \times 10^{-8}$ dm/s, $\tilde{U} = 1.3$, $\varepsilon = 0.12$, $K_m^K = 0.40$ mM, and $U_{max} = -4.3$. Figure from Gallaher et al. (Preprint A).

does not occur with the constant P_K of the isoprenaline case. The increase in U that follows the closing of a small fraction of IRKs leads to an increase of the term in curly brackets in Eq. (3.19). This implies a decrease of P_K . The smaller P_K , in turn, will drive the membrane potential U further away from $\ln(K_e/K_i)$ and closer to $\ln(N_e/N_i)$, i.e., U will increase faster, leading to a further decrease in P_K , etc. The “snowball” will stop when all IRKs are closed, $P_K = P_0$, and the depolarized branch is reached. The extracellular potassium concentration at which the switch is made from the hyperpolarized branch to the depolarized branch is symbolized by $K_e = K_e^{h \rightarrow d}$.

A similar snowball effect takes place from the depolarized branch to the hyperpolarized branch as K_e is again increased (cf. Fig. 3.4). Opening of a small fraction of IRKs can lead to hyperpolarization, i.e. U goes down. But a U that is further decreasing into the negative regime will increase P_K (cf. Eq. (3.19)). In this case the “snowball” will stop once all IRKs are open and $P_K = P_0 + P_{IRK}^{max}$. This switch occurs at $K_e = K_e^{d \rightarrow h}$.

3.2.4 The Dimensions of the Bistable Area

This analysis begins by focusing in on the bistable area (cf. Fig. 3.5) and applying a very rough approximation. The approximation is based on the following *Ansatz*. Going from the hyperpolarized

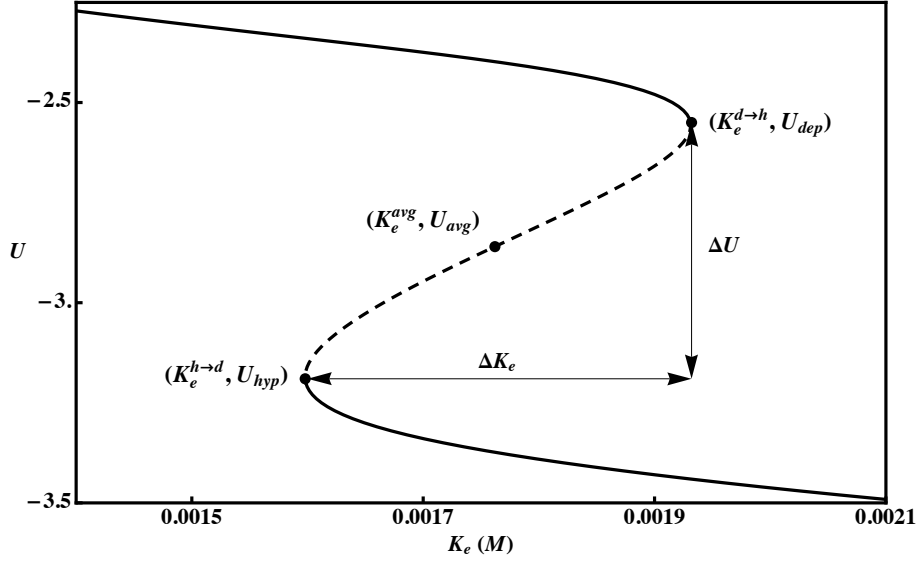


Figure 3.5: A close-up view of the same theoretical curve of Fig. 3.4 with the points of interest highlighted. Just the second part of Eq. (3.20), where the bistability is present, is shown here. The stable solutions are represented with a solid line and the unstable region is represented with a dashed line. The points of switching, the center inflection point, and the height and width are all labeled with the notation that is found in the text. Figure from Gallaher et al. (Preprint A).

branch to the depolarized branch, the aforementioned snowballing to the depolarized branch will occur after about *half* of the IRKs have closed. Likewise, the snowball effect leading to the massive opening in the depolarized-to-hyperpolarized transition will start after about *half* of the channels have already opened. It is possible to use a fraction different from 1/2. It is also possible to use different fractions for the two transitions. However, with a factor of 1/2 there is a plausible symmetry between the two transitions. The fraction of 1/2 means that the argument of the exponent in Eq. (3.19) equals zero. The *Ansatz* thus leads to:

$$U_{hyp} - \ln\left(\frac{K_e^{h \rightarrow d}}{K_i}\right) - \tilde{U} \approx U_{dep} - \ln\left(\frac{K_e^{d \rightarrow h}}{K_i}\right) - \tilde{U} \approx 0. \quad (3.21)$$

From Eq. (3.21) it is observed that the bistable area can be shifted to lower K_e -ranges by increasing \tilde{U} , which was found to be 1.3 or about 30 mV. Mathematically with Eq. (3.21) it is also possible to compensate for an increased \tilde{U} by increasing U_{hyp} and U_{dep} . However, the value of U_{hyp} is tied to U_{max} and it is largely fixed by the mechanisms that resulted in Eqs. (3.18) and (3.20). In numerical simulations of the system it is indeed observed that changing \tilde{U} leads to a horizontal shift of the bistable area (Siegenbeek van Heukelom, 1994; van Mil et al., 2003; Gallaher et al., 2009). Equation

3.21 can be used to derive the relationship between U_{hyp} , U_{dep} , K_e^{avg} , and ΔK_e .

The intracellular potassium concentration K_i is supposed not to change too much as the switch occurs. After all, the entire point of the bistability appears to be the protection of the high K_i . From Eq. (3.21) the following formula is obtained for the magnitude of the switch:

$$\Delta U = U_{dep} - U_{hyp} \approx \ln \left(\frac{K_e^{d \rightarrow h}}{K_e^{h \rightarrow d}} \right). \quad (3.22)$$

Taking advantage of the apparent symmetry (cf. Fig. 3.5) it is assumed that the switch points are equidistant from a central point (i.e. $K_e^{avg} = K_e^{d \rightarrow h} - \Delta K_e/2 = K_e^{h \rightarrow d} + \Delta K_e/2$). With a small ΔK_e using the fact that $\ln(1+\delta) \approx \delta$ for δ close to zero is reasonable. A linear relationship between the magnitude of the height (ΔU), the width ($\Delta K_e = K_e^{d \rightarrow h} - K_e^{h \rightarrow d}$), and the center (K_e^{avg}) of the bistable area is then found:

$$\Delta U \approx \left(\frac{\Delta K_e}{K_e^{avg}} \right). \quad (3.23)$$

Figure 3.5 reveals that $K_e^{h \rightarrow d} \approx 1.60$ mM and $K_e^{d \rightarrow h} \approx 1.95$ mM. These values in Eq. (3.22) predict $\Delta U \approx 0.20$. From Fig. 3.5 the two branches appear to be separated by $\Delta U = 0.65$ or about 17 mV. The *Ansatz* apparently leads to an estimation of the right order of magnitude. However, refinement is possible.

The term $\left\{ 1 + \exp \left[\left(U - \ln(K_e/K_i) - \tilde{U} \right) / \varepsilon \right] \right\}^{-1}$ in the expression for the P_K describes a sigmoid that, as $(U - \ln(K_e/K_i))$ increases, goes from an asymptotic value of 1 to an asymptotic value of 0. The transition from 1 to 0 is steeper if the value for ε is smaller. In the $\varepsilon \rightarrow 0$ limit, it no longer matters whether the critical fraction at which the “snowballing” starts is 1/2 or any other number between 0 and 1. In case of $\varepsilon \rightarrow 0$, different fractions can also be used for the two transitions without affecting the result. This is because with $\varepsilon \rightarrow 0$ the transition from 0 to 1 is effectively vertical. The experimental data in Fig. (3.4) were best fit with $\varepsilon = 0.12$. Around that value for ε the width of the bistable area can be made to vary by varying ε . This means that in this regime with $\varepsilon = 0.12$, the $\varepsilon \rightarrow 0$ limit does not yet apply and the fractions may vary from 1/2.

Equations can be obtained for the turning points because the tangent line to the theoretical curve in Fig. 3.5 becomes vertical when the switching occurs. Using the second part of Eq. (3.20) with $\partial U / \partial K_e \rightarrow \infty$ leads to two equations, one for U_{dep} and one for U_{hyp} :

$$U_{dep} - \tilde{U} - \ln\left(\frac{K_e}{K_i}\right) = \varepsilon \ln\left(\frac{P_0 + P_{\text{IRK}}^{\text{max}}}{P_0}\right) + \varepsilon \operatorname{arccosh}(-G(K_e)) \quad (3.24)$$

$$U_{hyp} - \tilde{U} - \ln\left(\frac{K_e}{K_i}\right) = \varepsilon \ln\left(\frac{P_0 + P_{\text{IRK}}^{\text{max}}}{P_0}\right) - \varepsilon \operatorname{arccosh}(-G(K_e)) , \quad (3.25)$$

where

$$G(K_e) = 1 + \frac{U_{\text{max}} P_{\text{Na}} P_{\text{IRK}}^{\text{max}}}{3\varepsilon P_0 (P_0 + P_{\text{IRK}}^{\text{max}})} \frac{K_e}{K_e + K_m^K} . \quad (3.26)$$

The symmetry is easy to see along the U -axis as the term $\varepsilon \operatorname{arccosh}(-G(K_e))$ on the right hand sides of Eqs. (3.24) and (3.25) shifts the potential up or down from a central point $\varepsilon \ln\left(\frac{P_0 + P_{\text{IRK}}^{\text{max}}}{P_0}\right)$ by nearly equal amounts (K_e 's are slightly different). In fact, getting rid of the last term on the right hand sides of these equations gives an equation for the center inflection point (cf. Fig. 3.5), which can also be found by using the second part of Eq. (3.20) with $\partial^2 U / \partial K_e^2 = 0$.

For Eq. (3.25), the two terms on the right hand side are nearly equal and opposite. They almost cancel each other out so the estimation in Eq. (3.21) for the hyperpolarized branch remains accurate:

$$U_{hyp} \approx \tilde{U} + \ln\left(\frac{K_e^{h \rightarrow d}}{K_i}\right) . \quad (3.27)$$

This implies that the snowballing from the hyperpolarized branch to the depolarized branch *will* occur after about half of the IRKs have closed. For the depolarized branch (Eq. (3.24)) the hyperbolic arccosine term presents another dependence on K_e so an approximation will ease the analysis.

$$\begin{aligned} \varepsilon \operatorname{arccosh}(-G) &= \varepsilon \ln(-G + \sqrt{G^2 - 1}) \\ &= \varepsilon \ln(-G - G\sqrt{1 - 1/G^2}) \\ &\approx \varepsilon \ln(-2G) \end{aligned} \quad (3.28)$$

The last step in Eq. (3.28) is acceptable because $G(K_e^{d \rightarrow h}) \approx -3.5$, so $1 \gg 1/G^2$. Furthermore, at $K_e^{d \rightarrow h}$ the potassium concentration is high enough to make the Michaelis-Menten term in Eq. (3.26)

practically unity. With this approximation an expression for the depolarized potential is found:

$$U_{dep} = \tilde{U} + \ln \left(\frac{K_e^{d \rightarrow h}}{K_i} \right) + \varepsilon \ln \left(\frac{P_0 + P_{\text{IRK}}^{max}}{P_0} \right) + \varepsilon \ln \left(-2 - \frac{2U_{max}P_{\text{Na}}P_{\text{IRK}}^{max}}{3\varepsilon P_0(P_0 + P_{\text{IRK}}^{max})} \right) . \quad (3.29)$$

Because of the extra terms here, the critical fraction of IRKs that need to open in order to switch back to the hyperpolarized branch is not $1/2$. The extra terms will make the argument of the exponent in Eq. (3.19) larger than zero, which makes the permeability very small. It follows that the depolarized-to-hyperpolarized transition will happen after only *very few* of the channels have opened. Now taking the difference in the depolarized and hyperpolarized potentials with some rearrangement gives the height of the bistable region:

$$\Delta U \approx \ln \left(\frac{K_e^{d \rightarrow h}}{K_e^{h \rightarrow d}} \right) + \varepsilon \ln \left(-2 \frac{P_{\text{IRK}}^{max}}{P_0} \left(1 + \frac{P_{\text{Na}}U_{max}}{3\varepsilon P_0} \right) \right) . \quad (3.30)$$

Using the parameters from Fig. 3.5 with $K_e^{h \rightarrow d} = 1.60$ mM and $K_e^{d \rightarrow h} = 1.95$ mM now gives $\Delta U = 0.73$. This is more than triple the rough estimate of $\Delta U = 0.20$ obtained before and is closer to the $\Delta U = 0.65$ that is obtained from the fit. Following the approximation that led to Eq. (3.23) and after some rearrangement the equation becomes:

$$\Delta U \approx \left(\frac{\Delta K_e}{K_e^{avg}} \right) + \varepsilon \ln \left(2 \frac{P_{\text{IRK}}^{max}}{P_0} \left(\frac{k_p}{\varepsilon P_0 C} - 1 \right) \right) . \quad (3.31)$$

It should be immediately obvious with Eq. (3.31) that with the aforementioned *Ansatz* of $\varepsilon \rightarrow 0$, the steepness of the transition increases and the approximation of Eq. (3.23) returns. Equation (3.31) shows how the parameters affect the geometry of the bistable area, but does not tell the full story. As the parameters ε , k_p , C , P_{IRK}^{max} and P_0 are changed, the height and the position of the bistable area are also affected through the dependence of K_e^{avg} on ε , k_p , C , P_{IRK}^{max} and P_0 . The validity of Eq. (3.31) as an approximation can be tested by numerically checking (against Eq. (3.20))

in conjunction with Eq. (3.19)) the geometry of the region. Upon plotting solutions it is indeed seen that a smaller k_p leads to a shift in the bistable area to larger values of K_e^{avg} . This makes sense, as with less pumping capability, the cell will have to switch sooner to a depolarized state (the switch occurs when active transport can't handle the extra sodium leak that hyperpolarization involves). A shift in the opposite direction (towards smaller K_e^{avg}) occurs when decreasing the osmolarity, C . Because $C = K_e + N_e \approx N_e$, decreasing C effectively decreases N_e . A smaller N_e reduces the passive sodium inflow (cf. Eq. (3.10)) and therefore presents less pressure on the pump. Increasing P_0 has the same effect as adding some isoprenaline to the system. P_0 accounts for the permeability of all K^+ channels other than the IRKs, so increasing this value is analogous to opening more K^+ channels that, unlike the IRKs, remain open at low K_e values. Increasing P_0 has the effect of decreasing the height and width of the bistable region. It can be seen in Eq. (3.31) that with a sufficiently large P_0 , a sufficiently large C or a sufficiently small k_p the logarithm will eventually give an imaginary number. The expression is then meaningless, ΔU is effectively undefined, and there is no longer any hysteresis. All in all, Eq. (3.31) describes how for finite parameter values a bifurcation occurs; a bistable region appears or disappears.

3.2.5 Discussion

The maintenance of the ionic balance of a living cell was analyzed at low extracellular potassium concentrations. This simple model involves only sodium and potassium. Active transport in the model against the electrochemical potential is carried out solely by the Na,K-ATPase. Passive transport takes place through sodium and potassium channels. It was shown that hysteretic behavior of the membrane potential emerges when the potassium permeability is not fixed and constant, but made to depend on the electrochemical potential of potassium (cf. Eq. (3.19)). The experiments with muscle cells are in good agreement with the results of the analysis of the model. Figure 3.3 depicts the theory and experiment for the case of a large constant potassium permeability. Figure 3.4 shows how a potassium permeability that is dominated by the IRKs (which have an open probability that depends on the electrochemical potential of potassium) leads to a bistable area. For this case, experiment and theory show first order phase transitions and hysteresis. Approximations that are inferred from the model can quantitatively account for how the dimensions and the location of the bistable area depend on the different parameters of the model.

Though the experiments were performed on muscle cells, this phenomenon is seen in other

types of cells (Gadsby and Cranefield, 1977; McCullough et al., 1990; Siegenbeek van Heukelom, 1991; Brismar and Collins, 1993; Jiang et al., 2001). This analysis may shed light on the broader issue of the role of IRKs in the potassium permeability of all cells. In the last chapter of the well-known textbook by Hille (1992) the evolution of ion channels is reconstructed. Extrapolating three billion years into Earth’s past is speculative. However, it is in the context of early evolution that an explanation of the bistability should be sought. On the basis of sequence homologies Hille estimates that IRKs first emerged more than 2.4 billion years ago. Hille suggests that there was a transitional period occurring 2-3 billion years ago during which many traits evolved to give way for the eukaryotic cell to develop. IRKs may be considered evolutionarily ancient and are found in both eukaryotes and prokaryotes (Miller, 2000; Durrell and Guy, 2001).

The selective advantage of the switching mechanism examined here is that it enables the cell to shut down in conditions of environmental stress. In the depolarized state the cell is insulating itself from the environment. With ion channels mostly closed and a very small electric transmembrane potential ion leak will be minimal. Consequently, the Na,K-ATPase pumps need not operate at a high turnover rate and ATP consumption will thus be very low. The sharp decrease of the transmembrane electric potential U that is seen in Fig. 3.3 could already qualify as a kind of switch. However, a switch without a bistable region carries the disadvantage that a cell can repeatedly “go to sleep” and “wake up” if the extracellular potassium concentration were to fluctuate in the $K_e < K_e^*$ region. No such metabolic confusion occurs if there is a sufficiently wide bistable region. A hyperpolarized to depolarized transition takes place when $K_e < K_e^{h \rightarrow d}$. The cell will remain in its state of hibernation also when K_e will subsequently fluctuate around $K_e^{h \rightarrow d}$. Only when K_e is large enough that the cell will not be metabolically compromised does the cell “wake up.” In the same respect, fluctuations of K_e around $K_e^{d \rightarrow h}$ will not lead to a switch once the cell is “awake”. The first order phase transitions and the bistable region provide the cell with a very robust safeguard against environmental challenge.

The role of chloride was not considered in this model. Because the permeability for Cl^- can be up to an order of magnitude higher than the permeability of K^+ , its contribution is not negligible (Bretag, 1987). Like for K^+ , for Cl^- the electric and chemical potentials nearly balance at physiological conditions. The Na,K,2Cl-cotransporter is driven by inward Na^+ flow and therefore leads to a greater sodium leak and a slight accumulation of intracellular Cl^- above the equilibrium

value. Changing the flux of Cl^- by stimulating or blocking the Na,K,2Cl-cotransporter preserves the hysteresis, but has effects on K_e^{avg} , ΔK_e , and/or ΔU (Gallagher et al., 2009). Coupling Na^+ and K^+ transport to Cl^- transport adds a complication to the system but appears to not change the basic dynamics. The effect of the chloride traffic on Eq. (3.31) may be as simple as adding another load on the pump and thereby decreasing the ratio k_p/C . However, the introduction of more adjustable parameters leads to larger equations and immunization of the theory against experimental falsification. By neglecting chloride, the accuracy of parameter estimates is sacrificed for the sake of simplicity and conciseness.

The transmembrane potential is dependent on the permeability of potassium which is, in turn, dependent on the extracellular concentration of potassium and the transmembrane potential itself. This nonlinearity may result in either a hyperpolarization or a depolarization of the transmembrane potential at low K_e . For normal function, the extracellular concentration of potassium must lie within a certain range, but low potassium conditions do occur and are not far from physiological conditions. The most common treatment for hypokalemia is through potassium supplementation, though this often is overshoot leaving one with hyperkalemia. Getting a good grip on the location and dimensions of the hysteretic region should be helpful in both understanding and treating this condition.

CHAPTER 4:

THERMAL AND ELECTRICAL MEMBRANE DEFORMATION

At normal physiological conditions, the probability of an ion crossing the lipid barrier is small. This is the reason that the passage of ions across the membrane is assumed to be through specialized pore-forming proteins. However, changes in the temperature and the imposing electric field can have an effect on the permeability of the membrane. At the phase transition, it is more likely that pores will be formed in the lipid matrix. The freezing point of the bulk lipids is not far from realistic cellular situations so must be considered. It has already been discussed how an electric field can influence a channel protein. But electric fields can also affect the lipid portion of the membrane. In this chapter, both thermal and electrical aspects of membrane pore formation will be discussed.

4.1 Thermodynamics of Membranes

At physiological temperatures the fluid membrane structure is constantly fluctuating. As early as 1970, Frye and Edidin had already confirmed free diffusion of membrane-bound proteins tagged with fluorescent markers as two cells were made to fuse (Frye and Edidin, 1970). This 2-D surface fluidity gives rise to a lateral diffusion constant on the order of $\mu\text{m}^2/\text{s}$ (Sankaran et al., 2009). Transverse diffusion, or flip-flopping, occurs when a lipid moves from one leaflet of the bilayer to the other. But traversing the bilayer is quite rare for a lipid because the energy required for this is much larger than that provided by the typical thermal fluctuations that have a magnitude of $k_B T$, where k_B is the Boltzmann constant and T is the temperature.

Throughout the extremely heterogeneous mixture that the cell membrane is, local rigidities are found that reduce the rate of surface diffusion in the membrane. The saturated or mono-unsaturated lipids are more inflexible, packed together, and less motile than the poly-unsaturated varieties. Lipids with a higher degree of unsaturation in their tails diffuse more freely and are more spatially extended. Lipids are also closely packed at an interface of a transmembrane protein. The protein surface within the membrane is highly distorted so that lipids tend to fit snugly into small cavities which reduces their mobility (Lee, 2003). Aggregated protein structures (O’Leary, 1987) and connections at the intracellular surface, such as anchor points of the cytoskeleton, also contribute to local membrane tension.

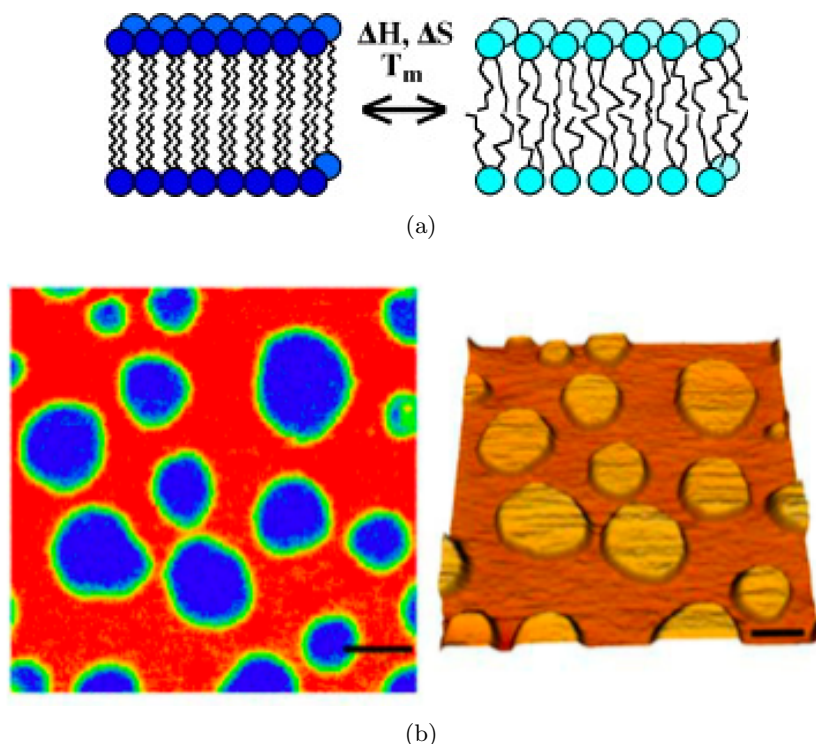


Figure 4.1: Phase properties of lipids at the freezing temperature. (a) At the freezing temperature (T_m), the lipids may exhibit properties of a gel (left) or a liquid (right) state. The change of phase is concurrent with changes in enthalpy (ΔH) and entropy (ΔS). Figure from Heimburg (2010). (b) Fluorescence image (left) and AFM topographical data (right) acquired on the same spot of a membrane at room temperature by Chiantia et al. (2006). The gel domains aggregate and form raised “rafts”. Scale bar = 2 μm . Modified from Biophysical Journal, 90, Salvatore Chiantia, Nicoletta Kahya, Jonas Ries, and Petra Schwille, Effects of Ceramide on Liquid-Ordered Domains Investigated by Simultaneous AFM and FCS, 4500-4508, Copyright 2006, with permission from Elsevier.

4.1.1 Lipid Rafts and the Freezing Transition

Membranes display peaks in heat capacity near physiological temperatures. These peaks indicate phase transitions. At higher than physiological temperatures protein unfolding contributes to these spikes in heat capacity and at just slightly lower than physiological temperatures the lipid freezing transition is found (Heimburg, 2007). At the freezing temperature, the membrane has both gel and liquid phases similar to ice floating in water at zero degrees Celcius. The drawing in Fig. 4.1(a) shows a visualization of the phase transition and the solid and liquid lipid structures. Lipids in the gel state tend to aggregate, forming rigid crystalline domains commonly referred to as “lipid rafts”. Figure 4.1(b) shows an atomic force micrograph of lipid rafts in a liposome membrane. Lengthscales of these isolated domains can range from the nanoscale to the microscale (Jacobson, 2007).

Lipid rafts form ordered gel domains from mainly high-freezing lipid components, cholesterol, and proteins (Heimburg, 2007). The overall composition of a cell membrane affects its freezing temperature and organisms can even change their lipid composition to adjust to different growth temperatures (Hazel, 1995). With a high concentration of “kinked” lipids (having C-C double bonds in the tail groups) the membrane becomes more fluid and the freezing temperature is drastically reduced (Heimburg, 2007). Long hydrocarbon chain lengths, however, increase the freezing temperature. Cholesterol is a topic of much research activity due to its unique and varied properties and the fact that typical concentrations are around 20-30 mol% of the membrane (Heimburg, 2007; Róg et al., 2009). It has a seemingly dual thermal nature. In the more fluid lipids, cholesterol increases ordering and rigidity, but it does the opposite in the gel phase (Róg et al., 2009). Cholesterol can be observed to broaden the freezing transition and lower the freezing enthalpy (Erand, 2007). The role of proteins in membrane freezing, due to their variety, is harder to determine. Membrane proteins have different effective transmembrane lengths within the bilayer and so will congregate with other components with similar size to reduce interfacial tensions. Hydrophobic mismatch between the proteins and the surrounding lipids may lead to changes in the lipid structure to compensate.

4.1.2 The Meyer-Overton Rule

The studies done by Ernest Overton in 1901 characterized how the potency of an anesthetic was proportional to its solubility in olive oil, which is similar in its apolarity to the lipid membranes of cells. Hans Meyer worked independently with different experimental methods and came to the same conclusions which became known as the Meyer-Overton rule of anesthesia. The basic idea of the Meyer-Overton rule is that the narcotic effect of substances is proportional to their ability to distribute within fat or fatty substances.

The packing order of membrane components appears to be essential to the phase properties of the membrane. A small molecule dissolved in the membrane should ideally mix with the fluid phase and not with the gel phase (Heimburg, 2007). The disordering of the molecular structure leads to enhancement of the fluidity of phospholipids in the membrane and a decrease in the freezing temperature, similar to what happens when salt dissolves in water. Incorporation of solutes into the bilayer can also disrupt protein function. This may be by directly inserting into gaps or cavities (Lugli et al., 2009) or by indirectly increasing the lateral pressure and thereby transitioning channels into closed conformations (Cantor, 1997).

4.1.3 Boundary Layer Deformation

As would be expected, the heat capacity at a constant pressure, c_P , is large at a phase transition. It can be understood how the increased heat capacity is related to increased enthalpy H fluctuations through the “fluctuation theorem,” $c_P = (\langle H^2 \rangle - \langle H \rangle^2) / k_B T^2$ (Kubo, 1966). Brownian fluctuations in the free-energy $E = H - TS$ are of the order of the ordinary $k_B T$ per molecule, where k_B represents Boltzmann’s constant and T is the absolute temperature. There is thus a corresponding change in the entropy S at the liquid-to-solid transition. The volume and the surface area of the membrane also change by a few percent upon freezing. Monte-Carlo simulations (Seeger et al., 2005) as well as atomic force microscopy (Oliynyk et al., 2008) have affirmed that fluctuations are large in the vicinity of the solid-liquid interface. The large volume and area fluctuations at a solid-liquid interface are associated with an increased compressibility in volume and area (Heimburg, 2007). The formation of spontaneous pores is more likely in areas where the lateral compressibility is high as less work is needed by the thermal motion to change the local curvature. Thus, pore formation is more likely near the domain interfaces or the protein cluster interfaces (Heimburg, 2007).

4.2 Electrical Membrane Deformation

The fluid inside and outside of the cell with the presence of free ions exhibits good conductivity. Pure lipid bilayers, however, are good insulators with area specific resistances in the range $10^6 - 10^9 \Omega\text{cm}^2$, whereas real cellular membranes have area specific resistances several orders of magnitude lower as $10^3 \Omega\text{cm}^2$ due to the many channels and pumps (Bier, 2005). A cell can be described as an insulating shell containing a conducting medium and in suspension of a conducting buffer. This dielectric discontinuity is prone to affect the electric field lines (Teissié et al., 1999). Because the bilayer thickness is so small (~ 5 nm) very little voltage is needed to separate the charges. This gives a membrane capacitance per unit area on the order of $\sim 1\mu\text{F}/\text{cm}^2$.

Electrical forces applied to cells have the greatest impact on the lipid bilayer structure and on the conformations of membrane proteins (Lee, 2005). The polar head groups of lipids in the cell membrane are most commonly negatively charged or polarizable. Likewise, proteins contain charged domains. The electric field causes charged groups to move, producing mechanical stress. This particular aspect is useful in allowing biological cells to detect electrical fields in their environment,

but it also makes them vulnerable to damage by an electric field. Water molecules can be pulled into transient defects in the lipid packing order within a bilayer and thus lead to pore formation (Lee, 2005). This phenomenon is called electroporation (Chang et al., 1992).

Electroporation techniques have been utilized for insertion of DNA, genes, proteins and other molecules into the interior of cells. An electric field can also be used to induce fusion and stimulate growth and proliferation (Titushkin and Cho, 2009). Both constant and alternating fields have been studied and thresholds for pore formation and pore stability depend on the magnitudes and frequencies applied. Pores may be transient and reversible, i.e. a “gentle” structural rearrangement of the lipid bilayer leads to a rapid electrical discharge followed by resealing (Lee, 2005). Otherwise the pores may be stable and irreversible and lead to eventual death of the cell. If pores are not closed rapidly, permeabilization leads to metabolic energy exhaustion as ion pumps work harder to compensate for the increased leak.

CHAPTER 5:

FRACTAL BEHAVIOR IN LIPID PORE KINETICS

Already in 1973 it was reported that the sodium permeability of an artificial lipid bilayer membrane peaked sharply at the phase transition temperature (Papahadjopoulos et al., 1973). Given the large fluctuations at the solid-liquid interface this result is no surprise. What was truly surprising was the discovery by Antonov et al. (1980) that this increased permeability comes in the form of quantized currents. For a relatively small transmembrane voltage (100 mV) “channels” of a fixed conductance in the picosiemens to nanosiemens regime appear to open and close. The behavior is strongly reminiscent of ion channel currents (Hille, 1992). It is peculiar that just the lipid domains by themselves can actually exhibit the same behavior as is exhibited by specialized ion channel proteins. The results of Antonov et al. (1980) have been reproduced many times and for many different kinds of membranes (Lev et al., 1993; Antonov et al., 1995; Wunderlich et al., 2009). These quantized currents that appear to turn on and off have, so far, defied explanation.

Ion channel opening and closing is a stochastic process. Recordings of single channels can be analyzed to give information on channel conductance, the probability of finding the channel open, and the distribution of open and closed dwelling times (Alvarez et al., 2002). Different types of noise reflect the kinetics of the system and can be characterized by their power spectral density. White noise has a flat power spectral density meaning that within the frequency bandwidth of interest there is equal power in every small interval Δf . When the noise band extends far beyond any characteristic frequency of the system, the noise is effectively random and uncorrelated in time. Brown noise has a power spectral density that follows $1/f^2$ and is related to a random walk type of behavior found with Brownian fluctuations. There is more energy in the lower frequencies for this kind of process. An intermediate type of noise with high frequencies like white noise but with long trends like brown noise is pink noise (also called flicker noise in electronics). Pink noise refers to any noise with a spectral density proportional to $1/f^\alpha$ where $0.5 \lesssim \alpha \lesssim 1.5$.

Pink noise was first found in electronics in the low frequency range but “ $1/f$ -like” noises have been encountered in music, earthquake sizes and frequencies, sandpile avalanches, and star luminosity. The associated scale invariance that occurs with $1/f$ noise is also often found spatially in biological structures like in the branching of blood vessels, lungs, and bones (Bassingthwaite

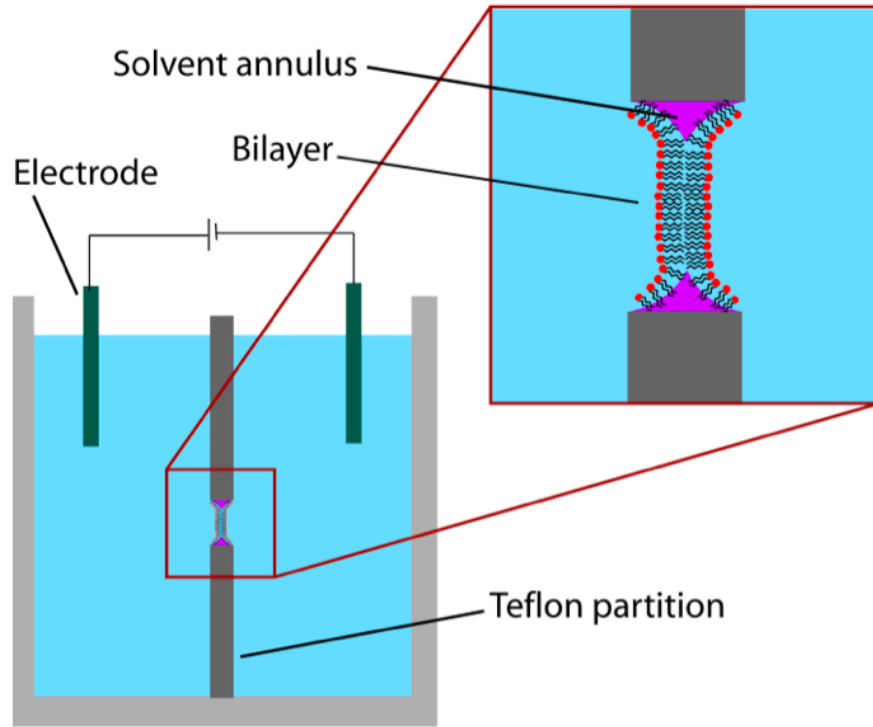
et al., 1994). With a signal that varies in time, there is a repeating structure at different timescales.

Nonlinear and nonequilibrium processes often reveal fractal behavior as well as systems near a critical point such as at a phase transition. In this chapter, a pure lipid bilayer near its phase transition will be studied. With the application of an electric field, the membrane forms pores that can be measured through transmembrane currents. The noise is analyzed and $1/f$ behavior is found. A theoretical model and physical explanation will be presented.

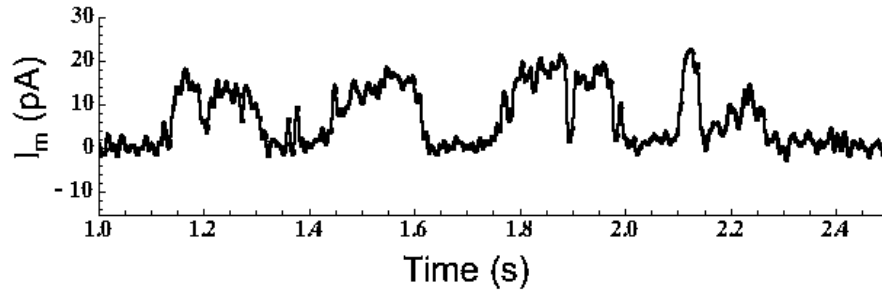
5.1 *Methods and Results*

Experiments were conducted using pure lipid bilayers composed of a DOPC:DPPC=2:1 (mol/mol) mixture (Wodzińska et al., 2009). The ratio and composition of lipids used was chosen because the freezing transition temperature is at room temperature (19°C). This obviously differs from a real biological membrane, but for these purposes, the substitution with pure lipids eliminates the possibility of ionic current through anything but the bulk lipid structure. Black lipid membranes (BLM) are formed by smearing pure lipids onto a hole about 80 μm in radius in an electrically insulating teflon film that is around 25 μm in thickness. A drawing of the setup is shown in Fig. 5.1(a). This membrane, with a KCl solution on both sides, reduces in size until it only contains two layers of lipids arranged tail-to-tail in a bilayer with around 5 nm thickness. Membranes are often compared to soap films, but a soap film has a thickness of the same order of magnitude as the wavelength of light so that variance in thickness gives rise to a colorful interference pattern. The thickness of the BLM is almost two orders of magnitude smaller than the shortest wavelength of visible light, and destructive interference always occurs between the reflected and transmitted waves. This interference gives the dark structure its name. A constant voltage of 210 mV was applied across the BLM. When a pore is formed, ions are able to pass through and a current can be recorded. Typical results are shown in Fig. 5.1(b). Further experimental details are included in Blicher et al. (2009) and Wodzińska et al. (2009).

Several data sets were available for analysis with differing concentrations of the anesthetic octanol. As was said in the previous chapter anesthetics affect the freezing transition temperature of the membrane. Figure 5.2(a) shows current densities for different concentrations of octanol (0 mol%, 7.9 mol%, and 15.9 mol%). The line that is lightest in color is the histogram for currents through the bilayer in a solution that contains no octanol. The histogram traces get darker in color for larger concentrations of octanol (7.9 mol% octanol and 15.9 mol% octanol, respectively).



(a)



(b)

Figure 5.1: Black lipid membrane experimental setup and data. (a) A black lipid membrane is formed by smearing a mixture of pure lipids onto a hole in a teflon partition. A potential difference can be applied via electrodes across the bilayer. This leads to permeabilization of the lipid membrane and the resulting current can be measured. Figure from Wikipedia (2008). (b) Sample of a current obtained when applying 210 mV across a pure lipid bilayer. There appear to be two main levels of current amplitude. The two levels correspond to a pore being open (high) or closed (low or zero). This sample has been reproduced from previously published data found in the reference by Blicher et al. (2009) and also appears in the reference by Gallaher et al. (Preprint B).

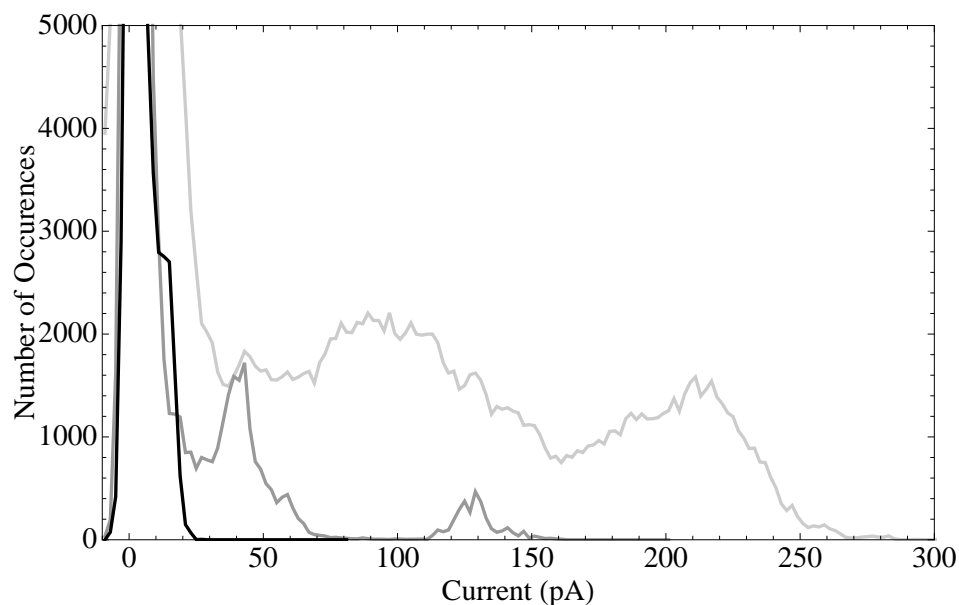
The measurements were recorded at room temperature, i.e 19 °C, which is around the range of the freezing transition of the pure lipid bilayer. As the concentration of octanol is increased, the freezing temperature is reduced. The corresponding increase in distance between the room temperature and the freezing temperature accounts for the reduced permeability.

The multiple peaks in the histogram shown in Fig. 5.2(a) at lower concentrations of octanol present a complication. The first pronounced peaks at nonzero values of current (around 100 pA for 0 mol% octanol and around 40 pA for 7.9 mol% octanol) are likely to correspond to one open pore. The next peak the right corresponds to about twice those currents and likely correspond to two open pores. With two open pores there is ambiguity in determining which pore may close at a given time making the duration of open times impossible to determine. To ease the analysis, the choice was made to work with the higher concentration of octanol which takes the freezing transition temperature further from room temperature and where the possibility of multiple pores is small. From the current density data of 15.9 mol% octanol, there is an apparent local minimum in between the two peaks (cf. Figure 5.2(b)). The cutoff value between open and closed was chosen at 10 pA. Slight changes in this value (9-11 pA) appear to not make much difference in the final outcome.

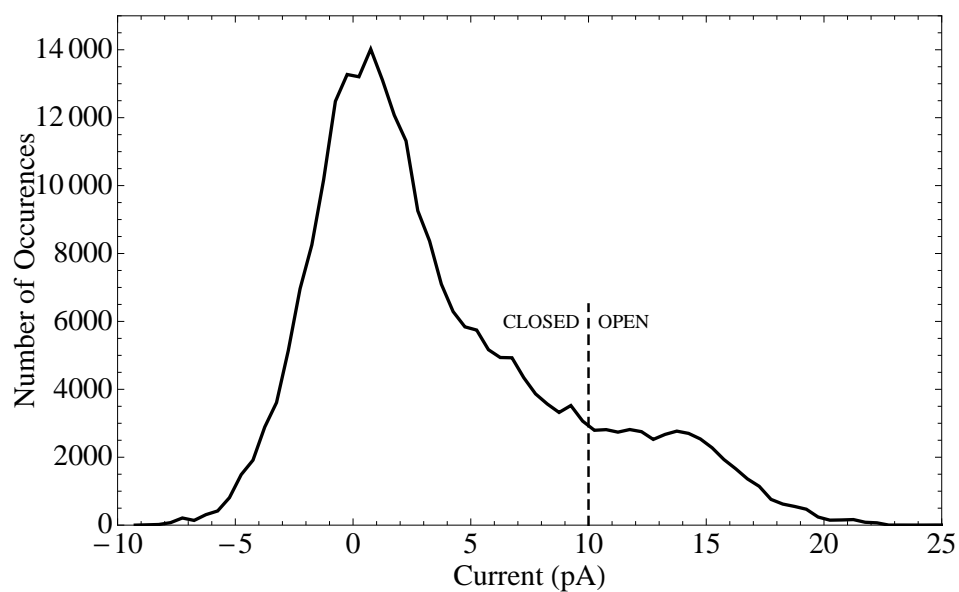
The open and closed lifetimes are calculated simply by determining, at each data point, whether the value is above or below the cutoff point and how long before the cutoff value is crossed again. The current was recorded every 0.1 ms for 30 seconds, but usually the last 5 seconds of the data are wildly fluctuating with large currents suggesting the irreversible breakdown of the seal that the BLM makes with the teflon. For this reason, only the first 25 seconds are used. Of course, because it is not known how long the conductance state remained before the recording started or after it stopped the times at the beginning and end of the data are discarded.

5.1.1 Building the Probability Density Histogram

When putting together an open time histogram with a wide range of timescales, the bin size choice generally constitutes a compromise. For a small bin size the number of events in each bin may become very small and, especially for large open times, the statistical variations from bin to bin will overwhelm any general trend. For a larger bin size one can lose a lot of information in the region of the shorter open times. Bassingthwaighe et al. (1994) described a method to join data for different bin sizes into one histogram. Liebovitch et al. (2001) provided an actual computer



(a)



(b)

Figure 5.2: Effect of anesthetics on membrane permeability. These graphs have been reproduced from previously published data found in the reference by Blicher et al. (2009). (a) Effect of octanol concentration on currents through the BLM. The line that is lightest in color is the histogram for currents through the bilayer in a solution that contains no octanol. The histogram traces get darker in color for larger concentrations of octanol (7.9 mol% octanol and 15.9 mol% octanol, respectively). This shows a reduction in current as more anesthetics are added to the membrane and the freezing temperature is lowered. (b) A closer view of the current density for 15.9 mol% octanol is shown here to see the open-closed cutoff value at 10 pA.

program to construct such a multiscale histogram. This was used as a template to be configured to work with the current signal data (for code see Appendix C).

The program goes from small to large timescales creating a probability density histogram at each effective bin width, t_i . The t_i begins with twice the smallest open time and increases at each iteration following $t_{i+1} = 1.1 \times t_i$. In the reference by Liebovitch et al. (2001) the value 2 was used in place of 1.1, which doubles the bin size each cycle. A smaller number was used here to generate more data points over a smaller range of time. First, memory space is allocated for an array of 20 bins each with the same bin size, t_i . The program goes through each one of the recorded times and counts how many times fall into each bin. In other words, for each open time (t) that satisfies $(j-1)t_i < t \leq jt_i$ for $1 \leq j \leq 20$, the number of counts in the bin ($N(j)$) increases by one. Histogram points in Fig. 5.3(a) are created with x and y -values of:

$$x(j) = t_i(j - 1/2) , \quad y(j) = \frac{N(j)}{t_i N_{\text{total}}} . \quad (5.1)$$

The x -value determines the time at center of each bin, and the y -value is the number of counts in each bin normalized by dividing by the size of each bin times the total number of recorded values, N_{total} .

Thus, one segment of the histogram is created at each scale. The size of the bin is then increased and the program cycles through the process creating points using larger and larger bin sizes. The first bin ($j = 1$) is always excluded because this will contain all of the times unresolved at t_i (Liebovitch et al., 2001). Also when a bin is encountered that contains no points before reaching $j = 20$, the loop breaks to the next t_i . Eventually the bin size becomes large enough that the counts in the bins become too sparse or all of the counts are in the first bin. The results are shown in Fig. 5.3(a). Over about two decades, the open time histogram is seen to be well fitted with a power law.

5.1.2 Calculating the Kinetic Rate Constants

The reference by Liebovitch et al. (2001) also shows how to calculate the time-dependent transition rate $k(t)$ from the open time histogram data. For each time scale the program first checks the counts in the 2nd, 3rd and 4th bins. Empty bins generally occur at the beginning and the end of the data where the times become scattered due to normal statistical variations at the limits of

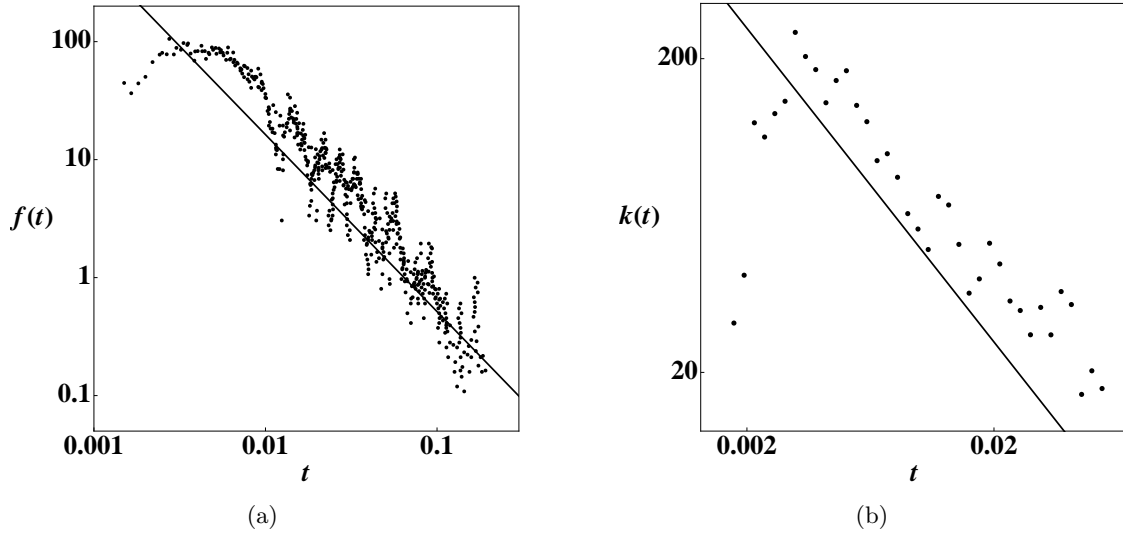


Figure 5.3: The probability density function and kinetic rate constants compared to the theoretical description. Figures from Gallaher et al. (Preprint B). (a) Probability density function, $f(t)$, of open times. The dots represent the points found from the data and the line is derived from the theory. The function for the line is given by $f(t) = t^{-3/2}/(2\sqrt{\pi\lambda})$, where $\lambda = 300$ Hz. (b) Closing rates determined from the experimental data. The function for the line is given by $k(t) = 1/2t$.

the experimental setup such as sampling rate and the duration of the experiment. If all three bins are occupied, a single exponential is fit to these bins by least squares. A rate k_i is calculated for each effective timescale t_i as:

$$k_i(t_i) = - \frac{3 \sum_{j=2}^4 x(j) \ln(N(j)) - \sum_{j=2}^4 x(j) \sum_{j=2}^4 \ln(N(j))}{3 \sum_{j=2}^4 (x(j))^2 - \left(\sum_{j=2}^4 x(j) \right)^2} . \quad (5.2)$$

The transition rate at each timescale is fit to an exponential from the early time behavior of each PDF histogram with this approach. Thus a distribution of transition rates is found. The results are shown in Fig. 5.3(b).

5.1.3 Finding the Power Spectral Density

The power spectral density captures the frequency spectrum and helps identify periodicities. This is found using the Fourier transform function built-in to *Mathematica*® (Wolfram Research, Inc., 2008). The list of current values was input into the “Fourier” function which performs a discrete Fourier transform and returns a list of complex numbers. The resulting list of numbers

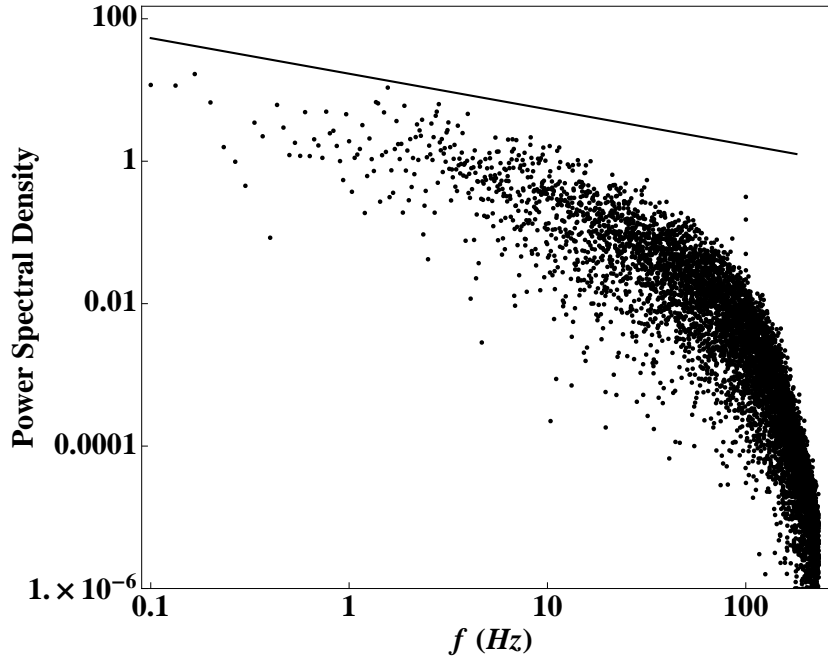


Figure 5.4: Power Spectral density of current signal in Fig. 5.1(b). A line proportional to $1/f^{1/2}$ is added for reference. Power law behavior is apparent in the significant frequency range. Figure from Gallaher et al. (Preprint B).

(the Fourier spectrum) was normalized by the number of data points. The y -values of the power spectral density in Fig. 5.4 were found by taking each value and multiplying by its conjugate and $4\pi^2$. The x -values in Fig. 5.4 are frequencies that are found by dividing the index by the time step (0.1 ms) and the number of data points.

5.2 Theory

Ion channels with a closed state (C) and an open state (O) have commonly been modeled as two-state molecules with Markov transitions connecting the two states:



where k_1 and k_2 are kinetic rate constants, i.e. the probability per second that the state will switch from closed to open and open to closed, respectively. The Markov property states that the transition probabilities for the system depend only on the state of that system and do not depend on the history. The simple $\text{C} \rightleftharpoons \text{O}$ scheme with time-independent transition rates leads to exponentially distributed lifetimes in both the open and closed state.

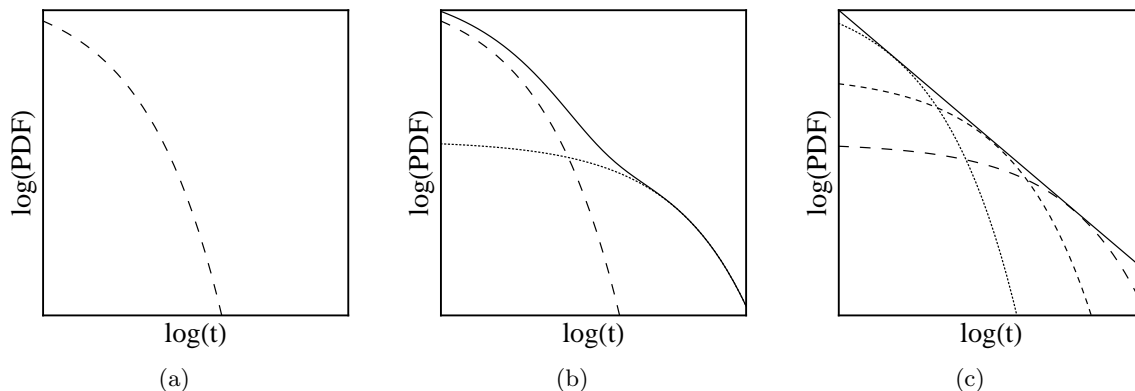


Figure 5.5: Examples of commonly encountered PDF distributions. (a) A distribution that is best described by a single exponential indicates that one transition rate dominates the dynamics. (b) A distribution with distinct bumps can indicate that more than one exponential contributes. The kinetic scheme with this distribution involves three states with two connecting transition rates. (c) A power law distribution finally emerges when the distribution involves more and more states and rates.

When only one or a few Markov transitions dominate, the distribution is a sum of exponentials (cf. Fig.'s 5.5(a) and 5.5(b)). With a large number of states and rates over many timescales (cf. Fig. 5.5(c)), the number of free parameters increases and fitting the data is a matter of coming up with sufficiently many states and rates until one is within the margin of error of the histogram.

Nonexponential distributions like that seen in Fig. 5.3(a) are commonly encountered in ion channel kinetics (Liebovitch and Tóth, 1991; Bezrukov and Winterhalter, 2002; Diba et al., 2004; Harada et al., 2009). Electrophysiologists have generally explained nonexponential distributions of closed and open times with kinetic schemes that contain more than two states (Colquhoun and Hawkes, 1995). With the method presented in the previous sections, the PDF can instead be interpreted in terms of energy barriers. As the PDF goes from a single exponential to a power law, the number of states increases or the open-to-closed transition rate $k(t)$ can be said to change in time, e.g. $k(t) \propto t^{-\mu}$ (Liebovitch et al., 2001). There is ample biomolecular justification for such a decreasing transition rate when we are dealing with the complicated proteins that ion channels are. Ion channels are protein complexes with a behavior that is often not adequately described with discrete states and rates or with a straightforward 1D reaction coordinate. Even a relatively simple protein like myoglobin turns out to be better described in terms of diffusive motion in a many dimensional conformational space (Frauenfelder et al., 1991). With a closing rate of $k(t) \propto t^{-\mu}$ for a channel, after the initial opening, the protein's state over time diffuses away from the activation

barrier to the closed state. The transition rate back to the closed state then decreases and the channel thus “stabilizes in its state” as time progresses.

In 1988 Millhauser, Salpeter, and Oswald proposed a kinetic scheme to explain the Fig. 5.3 type statistics that had been found in several ion channels (Millhauser et al., 1988). The original scheme has been modified to fit this particular situation for open times:

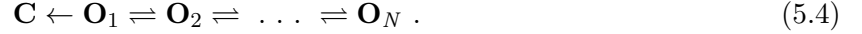


Figure 5.6: Proposed potential energy landscape that fits with kinetic scheme (5.4). The bump in the landscape represents the activation barrier between closed and open states.

The \mathbf{C} represents the closed state, and \mathbf{O}_1 through \mathbf{O}_N represent the many open states, each with the same conductance. The initial opening \mathbf{O}_1 occurs in the high-fluctuation interface area. Upon opening, a channel can close again soon after when it goes to state \mathbf{C} or it can stabilize in its open state by moving to the right. Each state is connected by a constant rate k . The decreasing $k(t)$ comes about as a significant fraction of the probability diffuses away towards \mathbf{O}_N . However, for finite N the eventual return to state \mathbf{C} is inevitable. Though the individual transitions in the above kinetic scheme are Markovian, there is a time-dependent rate $k(t)$ from the \mathbf{O}_1 to \mathbf{O}_N set of states back to the \mathbf{C} state.

More than a decade after the above kinetic scheme 5.4 was first proposed, Goychuk and Hänggi published a series of papers where the discrete diffusion in terms of states and rates was replaced by a continuous time random walk (Goychuk and Hänggi, 2002; Goychuk and Hänggi, 2003). They found the closed time statistics were the same in this case as what Millhauser, Salpeter, and Oswald had derived. Even for an energy landscape that is not flat, as shown in Fig. 5.6, but has some minor undulations, they found the same power laws to hold.

The model that was worked out by Millhauser, Salpeter, and Oswald and by Goychuk and Hänggi (MSOGH) was intended to describe diffusion in a protein’s conformational space. Such a space is an abstraction. But the MSOGH model can explain the mechanism behind the data

depicted in Fig.'s 5.3(a) and 5.3(b) as real lateral 2D diffusional expansion and contraction of a frozen domain around the pore as follows.

A pore is first formed in the solid-liquid interface area where the fluctuations are increased and the probability of pore formation is enhanced. If the pore remains at the chaotic region near this interface, the pore will most likely soon close again. If instead, the lipids making up the pore freeze then the pore will stabilize in its open state. The increased stabilization of the pore relates to Fig. 5.6 by moving to the right ($O_1 \rightarrow O_N$) as more lipids freeze around the pore. Eventually melting of the lipids around the pore makes the pore unstable again and corresponds to Fig. 5.6 by moving to the left ($O_1 \leftarrow O_N$). The diffusion in Fig. 5.6 in the open state actually describes the area change of the frozen raft around the pore.

If all rate constants are identical, the above kinetic scheme can be solved exactly (Millhauser et al., 1988). This is the case as the diffusion is isotropic and has no directional bias. Furthermore, the kinetic rates are made unitless and all set equal to 1. The master equation that is associated with the kinetic scheme then is:

$$\begin{aligned}\dot{p}_1(t) &= -2p_1 + p_2 \\ \dot{p}_n(t) &= p_{n-1} - 2p_n + p_{n+1} \quad \text{for } 1 < n < N \\ \dot{p}_N(t) &= p_{N-1} - p_N .\end{aligned}\tag{5.5}$$

where p_n is the probability of occupying state O_n at time t , and 1 through N refer to the open states of kinetic scheme (5.4). The probability $P(t)$ that a pore stays open for a time t is the sum of the probabilities $p_n(t)$ that the pore stays in the set of open states:

$$P(t) = \sum_{n=1}^N p_n(t) .\tag{5.6}$$

For N approaches infinity, an analytic solution can be obtained for Eq. (5.5) (Millhauser et al., 1988):

$$p_n(t) = \exp[-2t] (I_{n-1}(2t) - I_{n+1}(2t)) ,\tag{5.7}$$

where $I_n(t)$ represents the modified Bessel function of order n . An expansion for $2t \gg n^2$ leads to:

$$p_n \approx \frac{n}{2\sqrt{\pi} t^{3/2}} . \quad (5.8)$$

Figure 5.3(a) shows how, when normalized, the histogram is a probability density function of open times $f(t)$. If we let $P(t)$ denote the probability that the pore stays open until time t , then $f(t) = -\dot{P}(t)$. The distribution $f(t)$ is related to the transition rate $k(t)$ out of the open state in the following way: $k(t) = -f(t)/P(t) = -\frac{d}{dt} \ln P(t)$. From the above kinetic scheme, $f(t) = -dP(t)/dt = p_1(t)$. Starting with a newly opened pore at $t=0$ gives $p_1(0) = 1$ and $p_n(0) = 0$ for $n \geq 2$. This implies $P(0) = 1$. For the open-closed transitions, all that matters is $p_1(t)$. So for $t > 1$ a good approximation is:

$$P(t) \approx \frac{1}{\sqrt{\pi t}} , \quad f(t) \approx \frac{1}{2\sqrt{\pi} t^{3/2}} , \quad k(t) \approx \frac{1}{2t} . \quad (5.9)$$

All of these results are also shown in Millhauser et al. (1988).

The normalized transition rates must be unscaled in the kinetic scheme before the data in Fig. 5.3 can be related to the theory. The raw data was low-pass filtered with a cutoff frequency of $\lambda = 300$ Hz. The current signal, therefore, cannot be resolved at any frequency greater than λ and this accounts for the breakdown of the power law in Fig. 5.3(a) at around $1/\lambda \approx 3$ ms. The transition rates that connect the states of kinetic scheme (5.4) with the previously applied $t \geq 1$ condition that goes with kinetic scheme (5.9) then translates to $t \gtrsim 3$ ms. Unscaling Eq. (5.9) leads to $f(t) \approx t^{-3/2}/(2\sqrt{\pi\lambda})$. As $k(t) \times t$ is dimensionless the $k(t) \approx 1/(2t)$ remains unaffected by the unscaling. Figure 5.3 shows how the theory provides an almost perfect fit to the data.

The current traces in Fig. 5.1(b) make clear that the conductance of a single pore has a preferred level. Histograms presented in the references by Blicher et al. (2009) and Wodzińska et al. (2009) make this assertion more rigorous. If the pore is assumed to be cylindrical and electrolyte filled, then the conductance of 70 pS at 15.9 mol% octanol corresponds to a pore of 0.35 nm radius. Such a radius is indeed similar to that of many protein channels. A single head-group covers a surface area of about 0.6 nm² in the fluid state and of about 0.5 nm² in the gel state. Assuming pores again to be roughly cylindrical and the pore length to be 5 nm, this means that a pore of a 0.35

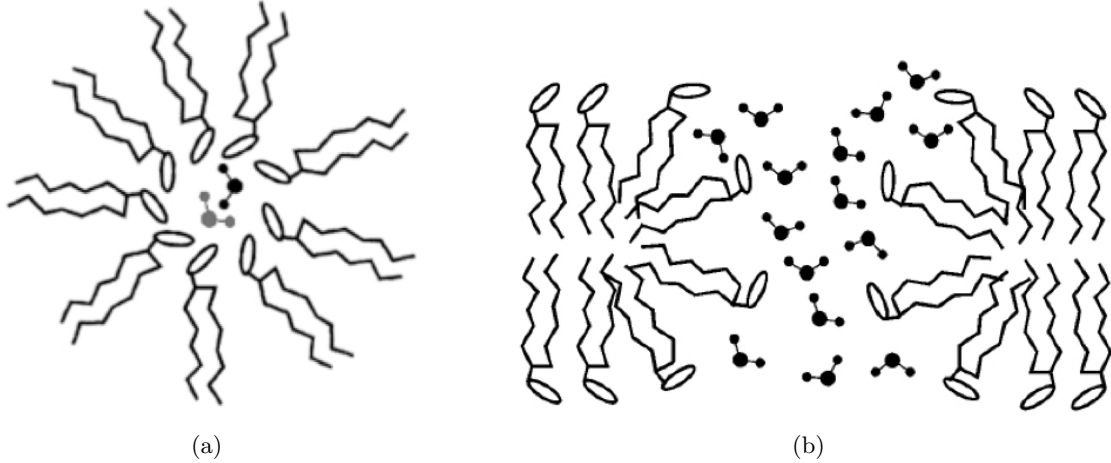


Figure 5.7: Lipid pore configurations. Forming a pore in the lipid bilayer involves a rearrangement of the lipid molecules. Exposing the polar head groups to the interior of the pore makes the pore permeable to water and small ions. (a) Lipid pore viewed from perpendicular to the membrane surface. (b) Lipid pore viewed as a cross-section of the membrane. Modified from Biophysical Journal, 95, Böckmann et al., Kinetics, Statistics, and Energetics of Lipid Membrane Electroporation Studied by Molecular Dynamics Simulations, 1837-1850, Copyright 2008, with permission from Elsevier (Böckmann et al., 2008). A modified version of this figure also appears in Gallaher et al. (Preprint B).

nm radius involves about 20 phospholipids in the lining of the pore (cf. Fig. 5.7).

5.3 Conclusions

Considerations involving standard electropore theory make clear why conductance quantization can occur. Forming a pore involves a rearrangement of phospholipids and an activation barrier has to be crossed to bring about such rearrangement (Bier, 2005). A minimum pore radius r_0 of a few tenths of nanometers is required for a pore to be permeable to water and ions. For phosphate head groups to keep facing the water even in the pore's interior, the phospholipids have to form a very curved edge. The energy required to create the edge of a pore of radius r is $2\pi\gamma r$, where γ is the so-called line tension (Litster, 1975). For small pores the total energy can be approximated with just the linear terms in the radius r , i.e., $E(r) = (2\pi\gamma - \varepsilon_0\varepsilon_w V^2)r$. Here V is the transmembrane voltage and ε_w is the relative dielectric permittivity of water. The term $-\varepsilon_0\varepsilon_w V^2$ describes the Maxwell stress due to the inhomogeneity of the electric field that the conducting aqueous pore causes (Winterhalter and Helfrich, 1987). This stress forces further opening of the pore. Electroporation has commonly been studied with voltages greater than 300 mV. Such large voltages are required to permeabilize a lipid bilayer in its liquid state. Near the lipid phase transition, pore formation begins at lower voltages. With smaller voltages the energy E increases very rapidly with r . In

this case, thermal fluctuations will not be sufficiently strong to drive the pore to radii that are significantly larger than r_0 . Once frozen, a pore will, of course, not change its radius.

Histograms were also made for the closed times. If every apparent pore opening in Fig. 5.1(b) were to stem from the formation of a new pore, then there would be a constant pore formation rate. Such a constant closed-to-open rate would lead to an exponential distribution of closed times. However, a power law is also observed for the closed times and $f(t)$ and $k(t)$ appear to follow Eq. (5.9). This phenomenon could be explained with the realization that the lining of a pore consists of about 20 phospholipids and that it is possible for a pore to partially melt. In that case some individual lipids in the lining get unstuck, move more freely, and clog up the pore. Meanwhile the large scale pore architecture remains in place and the pore can open again and refreeze. When several molecules are able to move independently into and out of the pore's interior the mechanism can be described by the kinetic scheme (5.10) and an MSOGH model. The apparent “-3/2”-power law for the closed times may be due to a significant fraction of the observed openings actually being such “re-openings.” The energy landscape shown in Fig. 5.8 shows how both the open and the closed state can stabilize in time through the freezing and melting of lipids around and within the pore. Molecules or clusters of molecules from the lining of the pore that are moving in and out of the pore's interior have also been offered as an explanation for the $1/f^\alpha$ noise that has been observed in biological and artificial channels in membranes (Läuger, 1988; Bezrukov and Winterhalter, 2002).

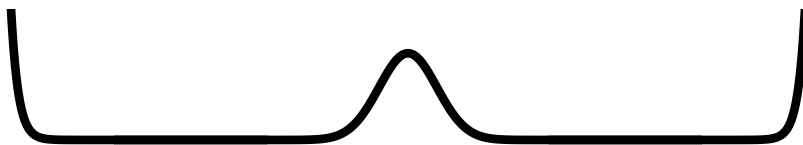
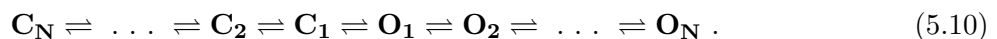


Figure 5.8: Proposed energy landscape for both closed and open states. Just after opening or closing the pore can over time diffuse away from the activation barrier. This leads to transition rate that decreases with time. This scheme with Fig. 5.10 predicts a $1/f^{1/2}$ power law for the power spectral density of the signal in Fig. 5.1(b).

Figure 5.4 shows how the power spectrum follows a power law for the recording in Fig. 5.1(b) for about two decades between the millisecond and the second regime where the power laws applied in Fig. 5.3. It can be derived for a kinetic scheme as given in Fig. 5.10 that the power spectral density

follows $1/f^D$ when the residence times in both the open and closed state follows $f(t) \propto t^{-(1+D)}$ where $0 < D < 1$ (Lowen and Teich, 1993). The observed power spectrum of Fig. 5.4 in the relevant frequency interval indeed displays the predicted -1/2 slope to a good approximation. Already in 1966 it was found that the membrane voltage at the node of Ranvier displays $1/f$ noise in the 10 to 1000 Hz regime (Derksen and Verveen, 1966). Recently, these data have been more accurately rerecorded and it has been claimed that the apparent power law comes about as a sum of Lorentzian contributions of individual types of ion channels (Diba et al., 2004). However, this observation could be associated with the phenomenon presented here.

A description and an explanation of ion channel like behavior of electropores in a lipid bilayer membrane has been presented. Many ion channels have open times in the millisecond regime. Extrapolation of the power laws in Fig.'s 5.3 and 5.4 would lead to frequent openings at that timescale. The possibility should be considered that some of the behavior that is traditionally attributed to ion channels may actually originate in the lipid membrane.

CHAPTER 6:

EPILOGUE

The study of biological membrane traffic is rich in physics and chemistry. The fact that the ion composition differs so greatly from one side to the other makes it an obvious non-equilibrium system. Nonlinear features like chaos, bursting, bifurcations, etc. are commonly encountered (Keener and Sneyd, 1998). Nonlinear dynamics often reveal fractal behavior, and fractals are also common near phase transitions. At these phase transitions “avalanches” can occur that may restabilize the system in its original state or lead to another state. The breadth of processes of molecular machinery must often be handled as chemical reactions using states and rates. Then, as fluctuations and diffusion processes are abundant, there is a wealth of stochastic phenomena to investigate.

This dissertation has addressed ion traffic through the cell membrane via channels, pumps, exchangers and the lipid bilayer itself. Ion transport is a necessary requirement for the maintenance of homeostasis, volume and the transmembrane potential. The changes in permeability at the lipid phase transition and with larger electric fields question channels, pumps and exchangers as the only source of membrane currents.

It was mentioned in Chapter 3 how it was presumed that there was a period of much activity in evolutionary changes from around 2-3 billion years ago in which many of the characteristics of eukaryotes developed. It appears that, as discussed at the start of this dissertation, the complexity of organisms increased due to the distribution of tasks to many parts which provides the selective advantage of higher organisms. A comparison of an animal cell with a bacterial cell may help make the ideas presented here more clear in this respect.

In many ways, bacterial cells are very similar to animal cells. They both have interiors with high potassium concentrations and low sodium concentrations and mostly live in seawater-like environments with low potassium and high sodium concentrations. Both types of cells maintain a transmembrane potential, but the animal cell may average around -75 mV whereas the bacterial cell keeps a potential of around -150 mV. This large potential difference for bacteria is needed to produce ATP. The metabolism of sugars and fats provides acetyl-coA, which then goes through the citric acid cycle where it is subject to a series of energetically downhill steps that result in the pumping of protons into the space between the membrane and the cell wall. With a proton gradient

that is higher outside and a large negatively charged interior, protons will move back in through the protein ATP-synthase and thus provide the energy to make ATP from ADP. Animal cells, however, contain mitochondria which serve the purpose of making ATP (cf. Fig. 6.1). Mitochondria are assumed to be descended from independent bacteria.

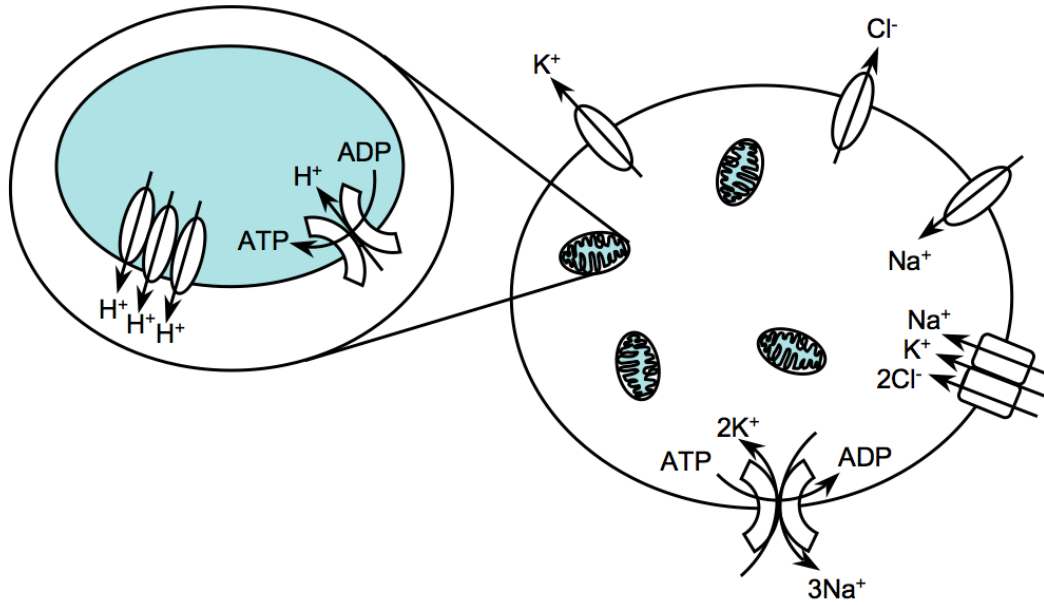


Figure 6.1: Ion traffic and ATP production in the animal cell. The mitochondria are similar to a bacteria cell and are said to be descended from independent bacteria. The presence of an energy-producing organelle in the animal cell changes the requirements for ionic homeostasis.

A bacterial cell also has both a cell membrane and a thicker, more rigid cell wall surrounding the membrane. Because of the cell wall, there is an extra protection against bursting with too much inflow of water, the only caveat is that a turgid pressure must be maintained to keep the membrane extended against the cell wall. The importance of the turgid pressure can be noticed in plant cells (which also have cell walls) and distinguishes a healthy, firm plant versus a wilting one. This pressure difference is accomplished by keeping a high osmotic content inside the cell to ensure sufficient water inflow. The high negatively charged interior will repel anions from entering the cell and the electrochemical gradient of sodium would result in too much influx and disturb the large negative potential needed for ATP production. Thus it seems reasonable that there is selective permeability to potassium ions. The low concentration of potassium in the extracellular environment provides a minimal entrance rate of positive charge, but enough to raise the osmolarity

to maintain pressure and keep the cell extended against the cell wall.

Potassium is the major cation present within all cells, including bacterial cells. The high intracellular concentration of potassium in bacteria is believed to be required for the optimal activity of many cellular enzymes, including those engaged in protein synthesis, for the regulation of intracellular pH, for DNA-protein interactions, and for controlled dissipation of the proton motive force (Asha and Gowrishankar, 1993). In addition, intracellular potassium has been shown to increase with an increase in osmolarity of the extracellular medium and is therefore thought to be an important determinant of cell turgor (Epstein, 1986). There are many transport systems that deal with potassium transport in the bacterial cell. The best characterized among them is Kdp, an extremely efficient scavenging system that turns on when the cell is exposed to potassium starvation conditions and costs energy to pump (Malli and Epstein, 1998). Kdp expression is also seen to increase with a hyperosmotic environment (Ballal et al., 2007).

The large electric potential of a bacterial cell may be necessary to produce ATP, but the animal cell has mitochondria to perform this function. Instead the potential in the animal cell can be thought of as a consequence of maintaining volume homeostasis (Armstrong, 2005). Lacking a cell wall to maintain structural integrity, the animal cell instead keeps an equal osmolarity inside and outside to prevent swelling or shrinking. Anions then can be driven outward in order to make osmotic room for the essential, internally confined, negatively charged substances such as sugars, proteins, and DNA (which generally carry a net negative charge). The Na,K-pump maintains the constant voltage in order to drive anions out. The endpoints for bacteria and animalia are the same: maintain integrity and metabolism. The ways they get there are based on different initial conditions. It is not unreasonable to assume that in the course of gaining the power-producing mitochondria and losing the confining cell wall, the animal cell co-evolved mechanisms for maintaining volume (through chloride transport) and keeping a high internal potassium concentration (IRKs). The Na,K,2Cl-cotransporter can adjust the osmotic content of the interior to keep balancing the exterior, but this presents another load on the pump. With low external potassium conditions *and* a hyperosmotic medium, the Na,K-ATPase would not be able to keep up with this increased demand for energy. So the closing of IRKs provides a means for a lower metabolic resting state in times of stress. The animal cell can thus afford to lose the rigidity and isolation provided by a cell wall by distributing tasks to different components within the cell. The increased ability of the cell

to communicate with its environment could further promote symbiotic relationships necessary for multicellularity. The complexity is further increased, but the robustness has as well.

It is an interesting phenomenon that the freezing point of the membrane is just slightly below the growth temperature of cells. As the growth temperature changes so does the lipid composition to keep the freezing transition consistently just below it. There must be a reason for this. This relationship could be an attribute at fast time scales compared to the time it takes to change membrane composition. One intriguing idea is that this relationship is necessary for the propagation of action potentials (Heimburg, 2007; Andersen et al., 2009). The idea is that during an action potential a pressure wave is induced along the axis of propagation. As the pressure increases, the freezing transition temperature increases and this brings about an increased permeability. By bringing the thermodynamic properties of the membrane into play, the action potential can be seen as a propagation of a compressibility wave that alters the phase properties and therefore allows conduction. The system studied here, with pure bilayers and a large (210 mV) transmembrane potential, is not quite like physiological conditions. However, extrapolation of the results suggest that some significant ion traffic could be occurring through the bilayer even at resting conditions.

Natural selection has optimized cell functioning in the course of evolution. Much can be understood through the genome but these processes occur through physical means. The study of ion traffic through the membrane presents a complex system where the whole is more than the sum of the parts and has to also be studied as such. Nonlinear physics is the tool to study such processes.

REFERENCES

- Adams, C. "Biorhythms.", 2007. <http://www.nurseminerva.co.uk/cellbiology.htm>. Online; accessed 14-April-2010.
- Aickin, C. C. "Chloride Transport Across the Sarcolemma of Vertebrate Smooth and Skeletal Muscle." In *Chloride Channels and Carriers in Nerve, Muscle and Glial Cells*, edited by A. F. Alvarez-Leefmans, and J. M. Russell, Plenum Press, London, 1990, 209–249.
- Aickin, C. C., Betz, W. J., & Harris, G. L. "Intracellular chloride and the mechanism for its accumulation in rat lumbrical muscle." *The Journal of Physiology* 411: (1989) 437–455.
- Alfonzo, A. V., Isles, C., Geddes, C., & Deighan, C. "Potassium disorders - clinical spectrum and emergency management." *Resuscitation* 70: (2006) 10–25.
- Alvarez, O., Gonzalez, C., & Latorre, R. "Counting Channels: A tutorial guide on ion channel fluctuation analysis." *Advances in Physiology Education* 26: (2002) 327–341.
- Andersen, S. S. L., Jackson, A. D., & Heimburg, T. "Towards a thermodynamic theory of nerve pulse propagation." *Progress in Neurobiology* 88: (2009) 104–113.
- Antonov, V. F., Anosov, A. A., Norik, V. P., & Smirnova, E. Y. "Soft perforation of planar bilayer lipid membranes of dipalmitoylphosphatidylcholine at the temperature of the phase transition from the liquid crystalline to the gel state." *European Biophysics Journal* 34: (1995) 155–162.
- Antonov, V. F., Petrov, V. V., Molnar, A. A., Predvoditelev, D. A., & Ivanov, A. S. "The appearance of single-ion channels in unmodified lipid bilayer membranes at the phase transition temperature." *Nature* 283: (1980) 585–586.
- Arispe, N., DeMazancourt, P., Pollard, H. B., & Rojas, E. "Modulation of a large-conductance K⁺ channel granule by adrenergic agonists and G proteins." *Ion Channel Pharmacology* 16: (1998) 343–379.
- Armstrong, C. "Channels and pumps early in evolution." In *Pumps, Transporters, and Ion Channels: Studies on Their Structure, Function, and Cell Biology*, edited by F. V. Sepúlveda, and F. Bezanilla, Kluwer Academic/Plenum Publishers, New York, 2005.
- Asha, H., & Gowrishankar, J. *Journal of Bacteriology* 175: (1993) 4528–4537.
- Ballal, A., Basu, B., & Apte, S. K. "The Kdp-ATPase system and its regulation." *Journal of Biosciences* 32.
- Bassingthwaighte, J. B., Liebovitch, L. S., & West, B. J. *Fractal Physiology*. Oxford University Press, New York, 1994.
- Bezrukov, S. M., & Winterhalter, M. "Examining noise sources at the single molecule level: 1/f noise of an open maltoporin channel." *Physical Review Letters* 85: (2002) 202–205.
- Bichet, D., Lin, Y. F., Ibarra, C. A., Huang, C. S., Yi, B. A., Jan, Y., & Jan, L. Y. "Evolving potassium channels by means of yeast selection reveals structural elements important for selectivity." *Proceedings of the National Academy of Sciences* 101: (2004) 4441–4446.
- Bier, M. "Gauging the strength of power frequency fields against membrane electrical noise." *Bioelectromagnetics* 26, 7: (2005) 595–609.
- Blicher, A., Wodzińska, K., Fidorra, M., Winterhalter, M., & Heimburg, T. "The temperature dependence of lipid membrane permeability, its quantized nature, and the influence of anesthetics." *Biophysical Journal* 96: (2009) 4581–4591.

- Böckmann, R. A., de Groot, B. L., Kakorin, S., Neumann, E., & Grubmüller, H. “Kinetics, statistics, and energetics of lipid membrane electroporation studied by molecular dynamics simulations.” *Biophysical Journal* 95: (2008) 1837–1850.
- Bordag, N., & Keller, S. “ α -helical transmembrane peptides: A “divide and conquer” approach to membrane proteins.” *Chemistry and Physics of Lipids* 163: (2010) 1–26.
- Boutillier, R. G. “Mechanisms of cell survival in hypoxia and hypothermia.” *Journal of Experimental Biology* 204: (2001) 3171–3181.
- Bretag, A. “Muscle chloride channels.” *Physiological Reviews* 67: (1987) 618–724.
- Brismar, T., & Collins, V. P. “Effect of external cation concentration and metabolic inhibitors on membrane potential of human glial cells.” *Journal of Physiology* 460: (1993) 365–383.
- Bubien, J. K., Kirk, K. L., Rado, T. A., & Frizzell, R. A. “Cell cycle dependence of chloride permeability in normal and cystic fibrosis lymphocytes.” *Science* 248: (1990) 1416–1419.
- Cantor, R. S. “The lateral pressure profile in membranes: a physical mechanism of general anesthesia.” *Biochemistry* 36.
- Chang, D. C., Saunders, J. A., Chassy, B. M., & Sowers, A. E., editors. *Guide to Electroporation and Electrofusion*. Academic Press, Inc., San Diego, 1992.
- Chiantia, S., Kahya, N., Ries, J., & Schwille, P. “Effects of ceramide on liquid-ordered domains investigated by simultaneous AFM and FCS.” *Biophysical Journal* 90: (2006) 4500–4508.
- Chung, S.-H., & Kuyucak, S. “Recent advances in ion channel research.” *Biochemica et Biophysica Acta* 1565: (2002) 267–286.
- Colquhoun, D., & Hawkes, A. G. “A Q-matrix cookbook.” In *Single-Channel Recording*, edited by B. Sakmann, and E. Neher, Plenum Press, New York, 1995, 589–633.
- Corry, B., Kuyucak, S., & Chung, S.-H. “Tests of continuum theories as models of ion channels. II. Poisson-Nernst-Planck theory versus brownian dynamics.”, 2000.
- Costa, P. F., Emilio, M. G., Fernandes, P. L., Ferreira, H. G., & Ferreira, K. G. “Determination of ionic permeability coefficients of the plasma membrane of xenopus laevis oocytes under voltage clamp.” *The Journal of Physiology* 413: (1989) 199–211.
- Danielli, J. F., & Davson, H. “A contribution to the theory of permeability of thin films.” *Journal Cellular and Comparative Physiology* 5, 4: (1935) 495–508.
- Dekker, C. “Bottom-up Nanotechnology.”, 2006. <http://med.tn.tudelft.nl/~hadley/nanoscience/week4/4.html>. Online; accessed 14-April-2010.
- Derksen, H. E., & Verveen, A. A. “Fluctuations of resting neural membrane potential.” *Science* 151: (1966) 1388–1389.
- DeWeer, P. “A century of thinking about cell membranes.” *Annual Review of Physiology* 62: (2000) 919–926.
- Dhaka, A., Viswanath, V., & Patapoutian, A. “TRP ion channels and temperature sensation.” *Annual Review of Neuroscience* 135–161.

- Diba, K., Lester, H. A., & Koch, C. "Intrinsic noise in cultured hippocampal neurons: experiment and modeling." *The Journal of Neuroscience* 24: (2004) 9723–9733.
- Donaldson, P. J., & Leader, J. P. "Intracellular ionic activities in the EDL muscle of the mouse." *Pflügers Archiv* 400, 2: (1984) 166–170.
- Durrell, S. R., & Guy, H. R. "A family of putative Kir potassium channels in prokaryotes." *BMC Evolutionary Biology* 1: (2001) 1–14.
- Edelstein-Keshet, L. *Mathematical Models in Biology*. Birkhäuser Mathematics Series. McGraw-Hill Inc., New York, 1988.
- Ellison, D. H. "Diuretic therapy and resistance in congestive heart failure." *Cardiology* 96: (2001) 132–143.
- Epand, R. M. "Detecting the presence of membrane domains using DSC." *Biophysical Chemistry* 126: (2007) 197–200.
- Epstein, W. "Osmoregulation by potassium transport in *Escherichia coli*." *FEMS Microbiology Reviews* 39: (1986) 73–78.
- Ferreira, H. G., & Marshall, M. W. *The Biophysical Basis of Excitability*. Cambridge University Press, Cambridge, UK, 1985.
- Ferrell, J. E., & Machleder, E. M. "The biochemical basis of an all-or-none cell fate switch in xenopus oocytes." *Science* 280: (1998) 895–898.
- Fraser, J. A., & Huang, C. L. "A quantitative analysis of cell volume and resting potential determination and regulation in excitable cells." *Journal of Physiology* 559: (2004) 459–478.
- Frauenfelder, H., Sligar, S. G., & Wolynes, P. G. "The energy landscapes and motions of proteins." *Science* 254: (1991) 1598–1603.
- Frye, L. D., & Edidin, M. "The rapid intermixing of cell surface antigens after formation of mouse-human heterokaryons." *Journal of Cell Science* 7: (1970) 319–335.
- Gadsby, D. C., & Cranefield, P. F. "Two Levels of Resting Potential in Cardiac Purkinje Fibers." *The Journal of General Physiology* 70: (1977) 725–746.
- Gallaher, J., Bier, M., & Siegenbeek van Heukelom, J. "The role of chloride transport in the control of the membrane potential in skeletal muscle - Theory and experiment." *Biophysical Chemistry* 143: (2009) 18–25.
- Gallaher, J., Bier, M., & Siegenbeek van Heukelom, J. "First order phase transition and hysteresis in a cell's maintenance of the membrane potential - an essential role for the inward potassium rectifiers.", Preprint A.
- Gallaher, J., Wodzińska, K., Heimburg, T., & Bier, M. "Ion-channel-like behavior in lipid bilayer membranes at the melting transition.", Preprint B.
- Geukes Foppen, R. J. "In skeletal muscle the relaxation of the resting membrane potential induced by K^+ permeability changes depends on Cl^- transport." *Pflügers Archiv European Journal of Physiology* 447: (2004) 416–425.

- Geukes Foppen, R. J., & Siegenbeek van Heukelom, J. "Isoprenaline-stimulated differential adrenergic response of K^+ channels in skeletal muscle under hypokalemic conditions." *Pflügers Archiv European Journal of Physiology* 446: (2003) 239–247.
- Geukes Foppen, R. J., van Mil, H. G. J., & Siegenbeek van Heukelom, J. "Effects of chloride transport on bistable behaviour of the membrane potential in mouse skeletal muscle." *The Journal of Physiology* 542: (2002) 181–191.
- Gisiger, T. "Scale invariance in biology: coincidence or footprint of a universal mechanism?" *Biological Reviews* 76: (2001) 161–209.
- Goodman, M. B., & Art, J. J. "Positive Feedback by a Potassium-Selective Inward Rectifier Enhances Tuning in Vertebrate Hair Cells." *Biophysical Journal* 71: (1996) 430–442.
- Gorter, E., & Grendel, F. "On bimolecular layers of lipoids on chromatocytes of blood." *Journal of Experimental Medicine* 41: (1925) 439–443.
- Goychuk, I., & Hänggi, P. "Ion channel gating: A first-passage time analysis of the Kramers type." *Proceedings of the National Academy of Sciences U.S.A.* 99: (2002) 3552–3556.
- Goychuk, I., & Hänggi, P. "The role of conformational diffusion in ion channel gating." *Physica A* 325: (2003) 9–18.
- Guo, D., & Lu, Z. "Interaction mechanisms between polyamines and IRK1 inward rectifier K^+ channels." *Journal of General Physiology* 122, 5: (2003) 485–500.
- Haas, M., & Forbush, B. "The Na-K-Cl cotransporter of secretory epithelia." *Annual Review of Physiology* 62: (2000) 515–534.
- Hagiwara, S., & Takahashi, K. "The anomalous rectification and cation selectivity of the membrane of a starfish egg cell." *Journal of Membrane Biology* 18, 1: (1974) 61–80.
- Harada, T., Yokogawa, T., Miyaguchi, T., & Kori, H. "Singular behavior of slow dynamics of single excitable cells." *Biophysical Journal* 96: (2009) 255–267.
- Hayashi, S., Tajkhorshid, E., & Schulten, K. "Photochemical reaction dynamics of the primary event of vision studied by means of a hybrid molecular simulation." *Biophysical Journal* 96: (2009) 403–416.
- Hazel, J. R. "Thermal adaptation in biological membranes: is homeoviscous adaptation the explanation?" *Annual Review of Physiology* 57: (1995) 19–42.
- Heimburg, T. *Thermal Biophysics of Membranes*. Wiley - VCH Verlag, Weinheim, Germany, 2007.
- Heimburg, T. "Fluctuations and Domains: Thermodynamic properties and heterogeneity of membrane assemblies.", 2010. http://membranes.nbi.dk/presentation-english/News_engl.html. Online; accessed 14-April-2010.
- Hille, B. *Ionic Channels of Excitable Membranes*. Sinauer Associates Inc., Sunderland, MA, 1992.
- Israelachvili, J. N. *Intermolecular and Surface Forces: With Applications to Colloidal and Biological Systems*. Academic Press, Inc., Orlando, Florida, 1985.

- Jackson, E. A. *Perspectives of Nonlinear Dynamics*. Cambridge University Press, Cambridge, UK, 1989.
- Jacobson, K. “Lipid rafts: at a crossroad between cell biology and physics.” *Nature Cell Biology* 9, 1: (2007) 7–14.
- Jentsch, T. J., Stein, V., Weinreich, F., & Zdebik, A. A. “Molecular structure and physiological function of chloride channels.” *Physiological Review* 82: (2002) 503–568.
- Jiang, Z., Si, J. Q., Lasarev, M. R., & Nuttal, A. L. “Two resting potential levels regulated by the inward-rectifier potassium channel in the guinea-pig spiral modiolar artery.” *Journal of Physiology* 537: (2001) 829–842.
- Jurkat-Rott, K., & Lehmann-Horn, F. “Paroxysmal muscle weakness - the familial periodic paralyses.” *Journal of Neurology* 253: (2006) 1391–1398.
- Katz, B. “Les constantes électriques de la membrane du muscle.” *Archives des Sciences Physiologiques* 3: (1949) 285–299.
- Kavraki, L. E. “Dimensionality Reduction Methods for Molecular Motion.”, 2007. <http://cnx.org/content/m11461/latest/>. Online; accessed 14-April-2010.
- Keener, J. P., & Sneyd, J. *Mathematical Physiology*. Springer-Verlag, Berlin, 1998.
- Kristensen, M., Hansen, T., & Juel, C. “Membrane proteins involved in potassium shifts during muscle activity and fatigue.” *American Journal of Physiology - Regulatory, Integrative and Comparative Physiology* 290: (2006) R766–R772.
- Kubo, R. “The fluctuation-dissipation theorem.” *Reports on Progress in Physics* 29: (1966) 255–284.
- Kume, H., Takai, A., Tokuno, H., & Tomita, T. “Regulation of Ca^{2+} -dependent K^{+} -channel activity in tracheal myocytes by phosphorylation.” *Nature* 341: (1989) 152–154.
- Kung, C., Saimi, Y., & Martinac, B. “Mechano-Sensitive Ion Channels in Microbes and Early Evolutionary Origin of Solvent Sensing.” In *Protein-Membrane Interactions*, edited by Toni Claudio, Academic Press, San Diego, 1990, 145–154.
- Landau, D. “Potassium-related inherited tubulopathies.” *Cell and Molecular Life Sciences* 62: (2006) 1962–1968.
- Läuger, P. “Internal motions in proteins and gating kinetics of ionic channels.” *Biophysical Journal* 53: (1988) 877–884.
- Läuger, P. *Electrogenic Ion Pumps*. Sinauer Associates Inc., Sunderland MA, 1991.
- Lee, A. G. “Lipid-protein interactions in biological membranes: a structural perspective.” *Biochimica et Biophysica Acta* 1612: (2003) 1–40.
- Lee, R. C. “Cell Injury By Electric Forces.” *Annals - New York Academy of Sciences* 1066: (2005) 85–91.
- Lev, A. A., Korchev, Y. E., Rostovtseva, T. K., Bashford, C. L., Edmonds, D. T., & Pasternak, C. A. “Rapid switching of ion current in narrow pores: implications for biological ion channels.” *Proceedings: Biological Sciences* 252: (1993) 187–192.

- Lewis, K. "Persister cells, dormancy and infectious disease." *Nature Reviews Microbiology* 5: (2007) 48–56.
- Liebovitch, L. S., & Tóth, T. I. "Distributions of activation energy barriers that produce stretched exponential probability distributions for the time spent in each state of the two state reaction $A \rightleftharpoons B$." *Journal of Mathematical Biology* 53: (1991) 443–455.
- Liebovitch, L., Scheurle, D., Rusek, M., & Zochowski, M. "Fractal methods to analyze ion channel kinetics." *Methods* 24: (2001) 359–375.
- Litster, J. D. "Stability of lipid bilayers and red blood cell membranes." *Physics Letters* 53A, 3: (1975) 193–194.
- Lowen, S. B., & Teich, M. C. "Fractal renewal processes generate $1/f$ noise." *Physical Review E* 47, 2: (1993) 993–1001.
- Lu, Z. "Mechanism of rectification in inward-rectifier K^+ channels." *Annual Review of Physiology* 66: (2004) 103–129.
- Lugli, A. K., Yost, C. S., & Kindler, C. H. "Anaesthetic mechanisms: update on the challenge of unravelling the mystery of anaesthesia." *European Society of Anaesthesiology* 26, 10: (2009) 807–820.
- Mallery, C. "Ion Channels.", 2007. http://www.bio.miami.edu/~cmallery/150/memb/ion_channel_1g1.jpg. Online; accessed 14-April-2010.
- Malli, R., & Epstein, W. "Expression of the Kdp ATPase is consistent with regulation by turgor pressure." *Journal of Bacteriology* 180, 19: (1998) 5102–5108.
- McCaig, D., & Leader, J. "Intracellular chloride activity in the extensor digitorum longus (EDL) muscle of the rat." *Journal of Membrane Biology* 81, 1: (1984) 9–17.
- McCullough, J. R., Chua, W. T., Rasmussen, H. H., Eick, R. E. T., & Singer, D. H. "Two stable levels of diastolic potential at physiological K^+ concentrations in human ventricular myocardial cells." *Circulation Research* 66: (1990) 191–201.
- Melkikh, A. V., & Sutormina, M. I. "Model of active transport of ions in cardiac cell." *Journal of Theoretical Biology* 252: (2008) 247–254.
- Miller, C. "An overview of the potassium channel family." *Genome Biology* 1: (2000) 1–5.
- Millhauser, G., Salpeter, E., & Oswald, R. "Diffusion models of ion-channel gating and the origin of power-law distributions from single-channel recording." *Proceedings of the National Academy of Sciences U.S.A.* 85: (1988) 1503–1507.
- Moore, W. J. *Physical Chemistry*. Prentice Hall Inc., Englewood Cliffs, NJ, 1972.
- Mouritsen, O. G., & Bloom, M. "Mattress model of lipid-protein interactions in membranes." *Biophysical Journal* 46, 2: (1984) 141–153.
- Muller, M. "Lectures 2 & 3: Chemistry and the Building Blocks of Life.", 2009. <http://www.uic.edu/classes/bios/bios100/lecturesf04am/lect02.htm>. Online; accessed 14-April-2010.
- Murray, J. D. *Mathematical Biology*. Springer-Verlag, Berlin, 1993.

- Myers, P. Z. “Buffeted by the winds of chance: why a cell is like a casino.”, 2008. http://scienceblogs.com/pharyngula/2008/02/buffeted_by_the_winds_of_chanc.php. Online; accessed 14-April-2010.
- Nichols, J. G., Martin, A. R., & Wallace, B. G. *From Neuron to Brain*. Sinauer Associates Inc., Sunderland MA, 1992.
- O’Leary, T. “Lateral diffusion of lipids in complex biological membranes.” *Proceedings of the National Academy of Sciences* 84: (1987) 429–433.
- Oliynyk, V., and Thomas Heimburg, M. J., Buckin, V., & Kaatz, U. “Lipid membrane domain formation and alamethicin aggregation studied by calorimetry, sound velocity measurements, and atomic force microscopy.” *Biophysical Chemistry* 134: (2008) 168–177.
- Osorio, D., & Nilsson, D. E. “Visual pigments: Trading noise for fast recovery.” *Current Biology* 14: (2004) R1051–R1053.
- Papahadjopoulos, D., Jacobson, K., Nir, S., & Isac, T. “Phase transitions in phospholipid vesicles. fluorescence polarization and permeability measurements concerning the effect of temperature and cholesterol.” *Biophysica Acta* 311: (1973) 330–348.
- Plischke, M., & Bergersen, B. *Equilibrium Statistical Physics*. World Scientific Publishing, Singapore, 1994.
- Qian, H., & Reluga, T. C. “Nonequilibrium thermodynamics and nonlinear kinetics in a cellular signaling switch.” *Physical Review Letters* 94: (2005) 028,101.
- Reichl, L. E. *A Modern Course in Statistical Physics*. University of Texas Press, Austin, 1980.
- Robertson, J. D. “The cell membrane concept.” *Journal of Physiology* 140: (1957) 58–59.
- Róg, T., Pasenkiewicz-Gierula, M., & Vattulainen, I. “Ordering effects of cholesterol and its analogs.” *Biochimica et Biophysica Acta* 1788: (2009) 97–121.
- Russell, J. M. “Sodium-potassium-chloride cotransport.” *Physiological Reviews* 80, 1: (2000) 211–276.
- Sankaran, J., Manna, M., Guo, L., Kraut, R., & Wohland, T. “Diffusion, transport, and cell membrane organization investigated by imaging fluorescence cross-correlation spectroscopy.” *Biophysical Journal* 97: (2009) 2630–2639.
- Seeger, H., Fidorra, M., & Heimburg, T. “Domain size and fluctuations at domain interfaces in lipid mixtures.” *Macromolecular Symposia* 219: (2005) 85–96.
- Sejersted, O. M. “Maintenance of Na, K-homeostasis by Na, K-pumps in striated muscle.” *Progress in Clinical and Biological Research* 268B: (1988) 195–206.
- Sejersted, O. M., & Sjøgaard, G. “Dynamics and consequences of potassium shifts in skeletal muscle and heart during exercise.” *Physiological Review* 80: (2000) 1411–1481.
- Siegenbeek van Heukelom, J. “Role of the anomalous rectifier in determining membrane potentials of mouse muscle fibres at low extracellular K⁺.” *The Journal of Physiology* 434, 1: (1991) 549–560.

- Siegenbeek van Heukelom, J. “The role of the potassium inward rectifier in defining cell membrane potentials in low potassium media, analyzed by computer simulation.” *Biophysical Chemistry* 50: (1994) 345–360.
- Siegenbeek van Heukelom, J., van Mil, H. G. J., & Geukes Foppen, R. J. “The (Na-K-2Cl)-cotransporter controls the depolarizing response of the skeletal muscle membrane to hypertonic media.” In *BioThermoKinetics of the Living Cell*, edited by H. V. Westerhoff, J. L. Snoep, J. Wijker, F. E. Sluese, and B. N. Kholodenko, BioThermoKinetics Press, Amsterdam, 1996.
- Singer, S., & Nicolson, G. “The fluid mosaic model of the structure of cell membranes.” *Science* 175: (1972) 720–731.
- Solé, R., & Goodwin, B. *Signs of Life: How Complexity Pervades Biology*. Basic Books, New York, 2000.
- Sonenshein, A. L. “Control of sporulation initiation in *Bacillus subtilis*.” *Current Opinion in Microbiology* 3, 6: (2000) 561–566.
- Spassova, M., & Lu, Z. “Coupled ion movement underlies rectification in an inward-rectifier K^+ channel.” *Journal of General Physiology* 112: (1998) 211–221.
- Staehelin, L. A. “The thylakoid membranes from the chloroplast of a plant cell.” In *Molecular Biology of the Cell*, edited by B. Alberts, A. Johnson, J. Lewis, M. Raff, K. Roberts, and P. Walter, Garland Science, Oxford, UK, 2002, Fig. 9–33.
- Standen, N. B., & Stanfield, P. R. “Inward rectification in skeletal muscle: a blocking particle model.” *Pflügers Archiv* 378: (1978) 173–178.
- Storr, W. “Magnetic Hysteresis.”, 2010. <http://www.electronics-tutorials.ws/electromagnetism/magnetic-hysteresis.html>. Online; accessed 14-April-2010.
- Strange, K. “Cellular volume homeostasis.” *Advanced Physiology Education* 28: (2004) 155–159.
- Struyk, A. F., & Cannon, S. C. “Paradoxical depolarization of Ba^{2+} - treated muscle exposed to low extracellular K^+ : insights into resting potential abnormalities in hypokalemic paralysis.” *Muscle and Nerve* 37: (2008) 326–337.
- Teissié, J., Eynard, N., Gabriel, B., & Rols, M. P. “Electropermeabilization of cell membranes.” *Advanced Drug Delivery Reviews* 35: (1999) 3–19.
- Titushkin, I., & Cho, M. “Regulation of cell cytoskeleton and membrane mechanics by electric field: role of linker proteins.” *Biophysical Journal* 96: (2009) 717–728.
- Tosteson, D. C. *Membrane Transport: People and Ideas*. American Physiological Society, Bethesda, Maryland, 1989.
- van Mil, H. G. J., Geukes Foppen, R. J., & Siegenbeek van Heukelom, J. “The influence of bumetanide on the membrane potential of mouse skeletal muscle cells in isotonic and hypertonic media.” *British Journal of Pharmacology* 120, 1: (1997) 39–44.
- van Mil, H. G. J., Siegenbeek van Heukelom, J., & Bier, M. “A bistable membrane potential at low extracellular potassium concentration.” *Biophysical Chemistry* 106, 1: (2003) 15–21.

- Wessel, R., Kristan, W. B., & Kleinfeld, D. “Supralinear summation of synaptic inputs by an invertebrate neuron: dendritic gain is mediated by an “inward rectifier” K^+ current.” *Journal of Neuroscience* 19, 14: (1999) 5875–5888.
- Wharton, D. A. *Life at the Limits: Organisms in Extreme Environments*. Cambridge University Press, Cambridge, UK, 2002.
- Wikimedia Commons. “Single Channel — Wikimedia Commons.”, 2006. http://commons.wikimedia.org/wiki/File:Single_channel.png. Online; accessed 14-April-2010.
- Wikipedia. “Lipid Bilayer — Wikipedia, The Free Encyclopedia.”, 2008. http://en.wikipedia.org/wiki/Lipid_bilayer. Online; accessed 14-April-2010.
- Winterhalter, M., & Helfrich, W. “Effect of voltage on pores in membranes.” *Physical Review A* 36, 12: (1987) 5874–5876.
- Wodzińska, K., Blicher, A., & Heimburg, T. “The thermodynamics of lipid ion channel formation in the absence and presence of anesthetics. BLM experiments and simulations.” *Soft Matter* 5: (2009) 3319–3330.
- Wolfram Research, Inc. “Mathematica Edition: Version 7.0.”, 2008.
- Wunderlich, B., Leirer, C., Idzko, A.-L., Keyser, U. F., Wixforth, A., Myles, V. M., Heimburg, T., & Schneider, M. F. “Phase-state dependent current fluctuations in pure lipid membranes.” *Biophysical Journal* 96: (2009) 4592–4597.
- Yamamoto, S., Ishihara, K., Ehara, T., & Shioya, T. “Cell-volume regulation by swelling-activated chloride current in guinea-pig ventricular myocytes.” *The Japanese Journal of Physiology* 54: (2004) 31–38.
- Yan, D. H., & Ishihara, K. “Different polyamine concentrations underlie the regional difference in the strong inward rectifier K^+ current in the heart.” *Physiological News* 60: (2005) 26–27.
- Yan, D. H., Nishimura, K., Yoshida, K., Nakahira, K., Ehara, T., Igarashi, K., & Ishihara, K. “Different intracellular polyamine concentrations underlie the difference in the inward rectifier K^+ currents in atria and ventricles of the guinea-pig heart.” *The Journal of Physiology* 563, 3: (2005) 713–724.
- Yeagle, P. *The Membranes of Cells*. Academic Press, Inc., Orlando, Florida, 1987.

APPENDIX A: CODE FOR CHLORIDE TRANSPORT MODEL

Below is the *Mathematica*® (Wolfram Research, Inc., 2008) code that produces the descending and ascending theoretical curves for control situation before the addition of bumetanide as described in Section 3.1 and as seen in Fig. 3.2(a) with thin symbols and curves. The codes for the other curves in Fig. 3.2 are similar with only small changes in the parameter values to fit the curves. The various parameter values for each situation are all given in Table 3.1. All length values in this program are reported in decimeters (dm) to be compatible with the units of Molar, M (M = mole/L = mole/dm³).

```
Clear["Global`*"];

(* First we create a graph with points indicating experimental data; *)
Kowaarden=1000 {0.00076,0.00139,0.0016,0.00181,0.00201,0.00223,0.00234,0.00264,
0.00285,0.0057};
expControlDesc =1000 {{.00076,-.0531},{.00201,-.0564},{.00243,-.0819},{0.00264,
-.0847},{.00285,-.0853},{.0057,-.0761}};
triangles1[{x_,y_}]:=Graphics[{Thickness[.003],Line[{x-.05,y-1},{x+.05,y-1},
{x,y+1},{x-.05,y-1}]}]
gECD=triangles1/@expControlDesc;
expControlAsc=1000{{.00076,-.0531},{.00181,-.0554},{.00201,-.0562},{.00223,
-.0566},{.00243,-.0571},{.00264,-.0577},{0.00285,-.0577},{.00314,-.0614},
{0.00342,-.0736},{.00399,-.0729},{.0057,-.0710}};
h=Length[expControlAsc];
gECA=Graphics[{Thickness[.003],Table[Circle[expControlAsc[[i]],{.05,1}],{i,1,
Length[expControlAsc]}]}];
expBumetDesc=1000{{.00076,-.0549},{0.0016,-.0586},{0.00181,-.0862},{.00222,
-.0909},{.00264,-.0882},{.00285,-.0875},{0.00399,-.083},{.0057,-.0768}};
gEBD=ListPlot[expBumetDesc,PlotStyle->{PointSize[0.003],Hue[1.0,0,1.0]},
DisplayFunction->Identity,PlotRange->All];
expBumetAsc=1000{{.00076,-.0549},{0.0016,-.0564},{0.00181,-.0571},{0.00201,
-.0576},{0.00222,-.0574},{.00264,-.0887},{0.00285,-.0908},{.0057,-.0779}};
gEBA=ListPlot[expBumetAsc,PlotStyle->{PointSize[0.002],Hue[1,0,1]},
DisplayFunction->Identity,PlotRange->All];

(*Useful parameters*)
```



```

RTF=0.026552;U=(Vm/RTF)//N;ToR=10;Fact=.10;MaxPrec=20;q=12183;
EK=(RTF)Log[Ko/Ki]//N;ENa=(RTF)Log[Nao/Nai]//N;ECli=-(RTF)Log[Clo/Cli]//N;

(*Extracellular ion concentrations*)
Nao=0.148-Ko;Clo=0.130;

(*channels characteristics*)
PNa=0.08 Po;(*ratio determines +/- the Vm when IRK is closed (Ko < 1 mM)*)
Pcl=Fact 1.9 10^-5; (*This value must result in Pcl/PK ~ 3 in the control*)

(*IRK characteristics*)
Po=6.06 10^-8;PKmax=0.65 Po;
Vs=0.0089;(*Vs determines +/- broadness H.loop*)
Vh=(EK+0.0118)//N;(*with the add. term one can shift the H.loop*)
PK=Po+(PKmax/Ko^(1/2))(1+Exp[(Vm-Vh)/Vs])^-1//N;

(*the individual passive ion-currents*)
JNa=-PNa U (Nai Exp[U]-Nao)/(Exp[U]-1);
JK=-PK U (Ki Exp[U]-Ko)/(Exp[U]-1);
JCl=-Pcl U (Clo Exp[U]-Cli)/(Exp[U]-1);

(*pump characteristics*)
KK=0.0013;(*determines Ko value where Vm starts to depolarize at low Ko*)
KNa=0.007;JpMax=0.55 10^-8;

(*the pump current*)
Jpump=-JpMax(1+KK/Ko)^(-2)(1+KNa/Nai)^(-3);

(*cotransporter characteristics*)
Adjust:=1;CotCor:=Adjust 2.4 10^-7;CotDrive:=EK+ENa-2ECli;
OsmStandaard:=0.296;OsmNul=0.266;CotOsm=OsmStandaard-OsmNul+Hyper;
Jcot:=-CotCor CotOsm (EK+ENa-2ECli);OsmolPIonsi=(Nai+Ki+Cli);
OsmolImp=OsmStandaard-OsmolPIonsi;

```

```

(*net currents*)
netJNa=JNa+3Jpump-Jcot;
netJK=JK-2Jpump-Jcot;
netJCl=JCl+2Jcot;

Vm=-0.07355;
Ko=0.0057;Hyper=0;
Do[sols=FindRoot[{netJNa==0,netJK==0,netJCl==0},{Nai,0.001},{Ki,0.107},
{Cli,0.009},AccuracyGoal->35,MaxIterations->10000];
    If[Im[Nai]!=0||Im[Ki]!=0,Print["Imaginary concentrations (IRK)"]; Break[]];
    Nai=sols[[1,2]];Ki=sols[[2,2]];Cli=sols[[3,2]];ENa=(RTF)Log[Nao/Nai];
    ECli=-(RTF)Log[Clo/Cli];Vo=-q(Nai+Ki-Cli)+Vm;
    Cleq=CloExp[Vm/(RTF)]; ECleq=-(RTF)Log[Clo/Cleq]/N

OPIi=OsmolPIonsi;
x0=Nai;
y0=Ki;
Clear[Nai,Ki,Cli];
Komin=0.0007;m=0;Clear[Ko];

Do[m=m+1;Clear[Nai,Ki,Cli,Vm];Vm=q*(2*Nai+2*Ki-OPIi)+Vo;
    Cli=OPIi-Nai-Ki;
    eqn1=D[x[t],t]==netJNa/.{Nai->x[t],Ki->y[t]};
    eqn2=D[y[t],t]==netJK/.{Nai->x[t],Ki->y[t]};
    sol=NDSolve[{eqn1,eqn2,x[0]==x0,y[0]==y0},{x,y},{t,0,10000000000}];
    Nai=x[10000000000]/.sol[[1,1]]; Ki=y[10000000000]/.sol[[1,2]];
    x0=Nai;y0=Ki;
    Clear[Vm];
    Vm=q*(2*Nai+2*Ki-OPIi)+Vo;
    If[Abs[Vm]>0.035,t1[m]=t1[m - 1],Break[]];
    t1[m]={Ko, Vm},{Ko, 0.0057, Komin, -0.0001}];

```

```

pp1=1000*Table[t1[i],{i,1,33}];
pp2=1000*Table[t1[i],{i,34,m-1}];
curv1=ListPlot[pp1,PlotJoined->True,PlotStyle->{Thickness[0.004],GrayLevel[0]},
  DisplayFunction->Identity,PlotRange->All,Axes->False];
curv2=ListPlot[pp2,PlotJoined->True,PlotStyle->{Thickness[0.004],GrayLevel[0]},
  DisplayFunction->Identity,PlotRange->All,Axes->False];
dash=Graphics[{Thickness[.004],Dashing[{0.002,0.01}],Arrow[{1000*t1[33],
  1000*t1[34]},10],Line[{1000*t1[33],1000*t1[34]}]}];

g1=Show[curv1,curv2,dash,gECD,DisplayFunction->$DisplayFunction,PlotRange->
  {{0.,6},{-110,-30}}]

OPIi=0smolPIonsi;
x0=0.0059589;
y0=0.0878939;
Clear[Nai,Ki,Cli];
Komin=0.0007;
m=0;
Clear[Ko];
Do[m=m+1;Clear[Nai,Ki,Cli,Vm];Vm=q*(2*Nai+2*Ki-OPIi)+Vo;
  Cli=OPIi-Nai-Ki;
  eqn1=D[x[t],t]==netJNa/.{Nai->x[t],Ki->y[t]};
  eqn2=D[y[t],t]==netJK/.{Nai->x[t],Ki->y[t]};
  sol=NDSolve[{eqn1,eqn2,x[0]==x0,y[0]==y0},{x,y},{t,0,10000000000}];
  Nai=x[10000000000]/.sol[[1,1]];
  Ki=y[10000000000]/.sol[[1,2]];
  x0=Nai;y0=Ki;Clear[Vm];
  Vm=q*(2*Nai+2*Ki-OPIi)+Vo;
  If[m<155,t2[m]=t2[m-1],Break[]];
  t2[m]={Ko,Vm},{Ko,Komin,0.0057,0.0001}];

pp1=1000*Table[t2[i],{i,1,25}];
pp2=1000*Table[t2[i],{i,26,m-1}];

```

```

curv1=ListPlot[pp1,PlotJoined->True,PlotStyle->{Thickness[0.004],GrayLevel[0]},
  DisplayFunction->Identity,PlotRange->All,Axes->False];
curv2=ListPlot[pp2,PlotJoined->True,PlotStyle->{Thickness[0.004],GrayLevel[0]},
  DisplayFunction->Identity,PlotRange->All,Axes->False];
dash=Graphics[{Thickness[.004],Dashing[{0.002,0.01}],Arrow[{1000*t2[25],
  1000*t2[26]},10],Line[{1000*t2[25],1000*t2[26]}]}];

g2=Show[curv1,curv2,dash,gECA,DisplayFunction->$DisplayFunction,
  PlotRange->{{0.,6},{-110,-30}}]

bc=Show[g1,g2]

```

APPENDIX B: DERIVATION OF CHLORIDE PERMEABILITY AND COTRANSPORTER FLUX

It will be shown in this Appendix how the values of P_{Cl} and J_{cot} can be derived from the comparison of the relaxation time without (the control) and with bumetanide (that blocks the cotransporter) in the medium. Experimental data presented in the reference by Geukes Foppen (2004) is used for this purpose as the same preparations were used. That reference used the imprecise chloride accumulation estimate (1.4 ± 1.2 mM) of Aickin et al. (1989) to achieve an estimate of J_{cot} . This approach also relies on estimations by others; in particular estimations for the permeability ratios for potassium, sodium and chloride and for the concentrations of these ions in the cell under physiological conditions. However, these values are more precisely known.

In the reference by Geukes Foppen (2004) it is described how barium, Ba^{2+} , was added to the extracellular medium. Ba^{2+} rapidly blocks the inwardly rectifying potassium channel (called here IRK). An exponential relaxation to a new steady state membrane potential occurs a few minutes after such blocking. As P_{Cl} is much larger than P_K and P_{Na} in this case, the relaxation to a new steady state value of V_m is primarily associated with the influx of chloride into the cell. The difference of the relaxation times with and without bumetanide can provide the value of the cotransporter flow J_{cot} .

With bumetanide in the medium, the accumulation of chloride is negligible and $V_m = E_{Cl}$ at steady state. The chloride contribution in the GHK-equation can then be left out as in Eq. (3.9). $V_m = -76$ mV was measured with just bumetanide in the medium. After the Mullins and Noda correction for the rheogenic properties of the Na/K-pump (see Chapter 4 of the reference by (Läuger, 1991)), the GHK equation is well fitted with physiological values $[K^+]_i = 132$ mM, $[Na^+]_i = 10$ mM, and $P_K/P_{Na} = 78$ for such V_m . With bumetanide *and* Ba^{2+} in the medium, $V_m = -51$ mV is measured after full relaxation. With the same values for $[K^+]_i$ and $[Na^+]_i$ this leads to $P_K/P_{Na} = 11$. A more detailed adjustment of the concentrations of sodium and potassium produces only a minor change in P_K/P_{Na} .

The driving force behind the chloride inflow is the difference between the actual membrane potential and the equilibrium potential for chloride, i.e. $V_m - E_{Cl}$, where $E_{Cl} = (RT/F) \ln ([Cl^-]_i/[Cl^-]_o)$. When V_m is increased upon the addition of Ba^{2+} , $V_m > E_{Cl}$ and chloride flows into the cell. The dedimensionalized voltage relaxes exponentially to a new steady state as

$$U(t) = U(0) + \Delta U(1 - \exp(-t/\tau)) .$$

Here ΔU is the dedimensionalized total change in V_m in the course of the entire relaxation and τ is the characteristic relaxation time that results when the relaxation of the membrane potential is fitted with a single exponential. The change in intracellular chloride can be described as follows:

$$[\text{Cl}^-]_{\text{i}}(t) = a [\text{Cl}^-]_{\text{o}} \exp [U(t)] ,$$

where $a = E_{\text{Cl}}(0)/V_m(0)$. The slope of $[\text{Cl}^-]_{\text{i}}(t)$ at $t = 0$ (i.e. directly after the addition of Ba^{2+}) can be approximated by differentiating this expression with respect to time and setting $t = 0$:

$$\frac{d}{dt} [\text{Cl}^-]_{\text{i}}(t=0) \approx a [\text{Cl}^-]_{\text{o}} \frac{\Delta U}{\tau} \exp [U(0)] .$$

All the values on the right hand side of this equation can be measured or well approximated. Following Eq. (3.5), the estimate for the flux through the chloride channels is

$$J_{\text{Cl}}(t=0) = \frac{1}{4}d \left(\frac{d [\text{Cl}^-]_{\text{i}}(t)}{dt} \right)_{t=0} ,$$

where d denotes the diameter of the cylindrical muscle cell. For the cases with and without bumetanide the difference of the J_{Cl} 's is due to the constant cotransporter flux J_{cot} . Without bumetanide the measured values are $\tau = 127 \pm 7$ s, $a = 1.03 \pm 0.01$, and $\Delta U = 0.84 \pm 0.03$ and with bumetanide $\tau = 182 \pm 23$ s, $a = 1.03 \pm 0.01$, and $\Delta U = 0.92 \pm 0.05$ (Geukes Foppen, 2004). This leads to $J_{\text{cot}} = 20 \pm 8$ pmole $\text{cm}^{-2}\text{s}^{-1}$.

In the main text a situation in which the medium is made hyperosmotic is also examined. A hyperosmotic medium increases the flow through the cotransporter. The above analysis is repeated for the hyperosmotic situation with parameters $\tau = 90 \pm 5$ s, $a = 1.02 \pm 0.01$, and $\Delta U = 0.53 \pm 0.05$ leads to $J_{\text{cot}}^{\text{hyp}} = 28 \pm 16$ pmole $\text{cm}^{-2}\text{s}^{-1}$.

In the control situation, without bumetanide, the steady state transmembrane potential before the addition of Ba^{2+} is -73 mV. A small hyperpolarization to -76 mV occurs when just bumetanide is added. Such 3 mV hyperpolarization is associated with intracellular chloride decrease, i.e. an

intracellular chloride concentration that is slightly lower when at the chloride equilibrium (with bumetanide in the medium) than in the control situation. The reference by Bretag (1987) reports a $P_{\text{Cl}}/P_{\text{K}}$ that is in the range of 3 to 10. A larger value of $P_{\text{Cl}}/P_{\text{K}}$ would make the chloride decrease smaller. This is because the passive efflux of chloride, being equal to the influx through the cotransporter, needs a smaller driving force when the value of P_{Cl} is larger. In the control steady state, J_{cot} is equal and opposite to the passive outward flow through the chloride channels. With Eq. (3.3) of the main text $P_{\text{Cl}} = (21 \pm 2) \times 10^{-6} \text{ cm s}^{-1}$ is obtained in the control, $P_{\text{Cl}} = (20 \pm 2) \times 10^{-6} \text{ cm s}^{-1}$ is obtained for the medium with bumetanide, and $P_{\text{Cl}} = (15 \pm 2) \times 10^{-6} \text{ cm s}^{-1}$ is found for the hyperosmotic medium. These values are consistent with the range assumed at the beginning of the derivation.

APPENDIX C: CODE FOR COMPUTING PDF, TIME-DEPENDENT TRANSITION RATES, AND POWER SPECTRAL DENSITY

Below is the *Mathematica*® (Wolfram Research, Inc., 2008) code used to compute the multiscale probability density function (PDF), kinetic rate constants, and power spectral density described in Chapter 5. The initialization section at the beginning specifies the data file to use for the current signal data, which should be formatted as a list of current amplitudes (in picoamps) over time (in seconds)).

```
(*Initialization*)
Clear["Global'"];
SetDirectory["Desktop/desktop folders/channeldata/pdf"];
datfile = "15.9mol.txt";
datmax = 250000;
cutoffoc = 10;
min = 2;
tstepdat = .0001;
f = OpenRead[datfile];
data = ReadList[f, {Number, Number}];
Close[f];

(*power spectral density*)

fft=Fourier[Take[data,All,-1]]//Flatten,FourierParameters -> {-1, 1}];
ps=Table[{(i-1)/(tstepdat Length[fft]), 4\[Pi]^2 fft[[i]] Conjugate[fft[[i]]]},
  {i,Length[fft]}};

psrange=Take[ps,7000];
llp=LogLogPlot[(\[Pi] t)^(-1/2),{t,.09,200},PlotStyle->{Thickness[.003],Black}];
logplot=ListLogLogPlot[psrange,Frame->True,FrameStyle->Bold,PlotStyle->Black,
  PlotRange->{{.09,300},{10^-6,40}},LabelStyle->Directive[20,Bold],
  FrameTicks->{{.1,1,10,100},Automatic,{},{}}];
Show[logplot,llp,AspectRatio->1/1.2,ImageSize->Large]

(*Get Open/Closed Times*)
```



```

Clear[i,to,n,tc,m,topen,tclosed]

n=m=i=1;

While[i<datmax,

  tc=0;to=0;

  If[data[[i,2]]<cutoffoc,
    {While[data[[i,2]]<cutoffoc && i<datmax,
      tc=tc+1;
      i=i+1]},
    {While[data[[i,2]]>cutoffoc && i<datmax,
      to=to+1;
      i=i+1}]];

  If[to>0,
    Do[topen[n]=to .0001;
      n=n+1,{1}],to=0];
  If[tc>0,
    Do[tclosed[m]=tc .0001;
      m=m+1,{1}], tc=0];
]

ttab[1]=Table[tclosed[i],{i,2,m-2}];
ttab[2]=Table[topen[i],{i,1,n-1}];

(* Probability Density Function *)
For[w=1,w<=2,w++,
  ptotal=Length[ttab[w]];
  ntotal=0;
  dt=min Min[ttab[w]];
  For[i1=1,i1<=500,i1++,
    pin=0;

```

```

pout=0;
d=dt*(1.1^(i1-1));
bin=Table[0,{i,1,21}];
lbin=Table[g d+d/2,{g,0,20}];

For[i2=1,i2<=ptotal,i2++,
  k=Floor[ttab[w][[i2]]/d]+1;
  If[k<21,{bin[[k]]=bin[[k]]+1,pin=pin+1},{bin[[21]]=bin[[21]]+1,
    pout=pout+1}];
];

For[i3=2,i3<=20,i3++,
  If[bin[[i3]]>0,{ntotal=ntotal+1;
    x[ntotal]=lbin[[i3]];
    y[ntotal]=bin[[i3]]/(d ptotal);
    If[i3<5,{logy[i3]=Log[bin[[i3]]/(d ptotal)]},Null];
    },Null];
];

btest=bin[[2]] bin[[3]] bin[[4]];
If[btest==0,Break[],{s = 3;
  sx=sy=sxx=sxy=stt=0;
  For[i=2,i<5,i++,
    sx+=lbin[[i]];
    sy+=logy[i];
    sxx+=lbin[[i]]^2;
    sxy+=logy[i] lbin[[i]];
  ]
  For[i=2,i<5,i++,
    stt+=((lbin[[i]]-sx/s)*(lbin[[i]]-sx/s));
  ]}
];

```

```

delta=s*sxx-(sx*sx);
A=((sxx*sy)-(sx*sxy))/delta;
B=-((s*sxy)-(sx*sy))/delta;
siga=(1+(sx*sx/(s*stt)))/s;
sigb=1.0/stt;
cov=-sx/(s*stt);
corr=cov/(Sqrt[siga*sigb]);
rates[i1]={d,B};
];

tab=Table[{x[i],y[i]},{i,1,ntotal}];
rattab={};
For[i=1,i<i1,i++,
  If[rates[i][[2]]>0,AppendTo[rattab,rates[i]];
  ];];

If[w==1,
  {ctab=tab;ratesc=rattab;},{otab=tab;rateso=rattab;});
]

Show[{ListLogLogPlot[otab,DisplayFunction->Identity,Frame->True,FrameStyle->Bold,
  PlotStyle->{Black,PointSize[.009]},LabelStyle->Directive[30,Bold],ImageSize->Large},
  FrameTicks->{{.001,.01,.1},{.1,1,10,100},{},{},PlotRange->{{.001,.3},{.05,200}},
  LogLogPlot[1/(2 Sqrt[\[Pi] 300]) t^-1.5,{t,.0001,1},DisplayFunction->Identity,
  PlotStyle->{Thickness[.004],Black}],DisplayFunction->$DisplayFunction,
  AspectRatio->1]

Show[{ListLogLogPlot[rateso,DisplayFunction->Identity,Frame->True,FrameStyle->Bold,
  LabelStyle->Directive[30,Bold],PlotRange->{{.0013,.07},{13, 300}},ImageSize->Large},
  FrameTicks->{{.002,.02},{20,200},{},{},PlotStyle->{PointSize[.012],Black},
  LogLogPlot[.5 t^-1,{t,.0001,1},DisplayFunction->Identity,AspectRatio->1,

```

```
PlotStyle->{Thickness[.004],Black}},DisplayFunction->$DisplayFunction]
```

